Architecture for a scalable ion-trap quantum computer

Dissertation

zur Erlangung des Doktorgrades an der

Fakultät für Mathematik, Informatik und Physik
der Leopold-Franzens-Universität Innsbruck
vorgelegt von

Dipl. Phys. Maximilian Josef Harlander

durchgeführt am Institut für Experimentalphysik

unter der Leitung von
Univ.-Prof. Dr. Rainer Blatt

März 2012

Kurzfassung

Skalierbare Architekturen für Quanteninformatik mit Ionenfallen basieren auf der Möglichkeit eine größere Anzahl von Ionen innerhalb eines Prozessors (einer Ionenfalle) zu speichern und zu manipulieren. Für eine zuverlässige Kontrolle der Informationsträger (Ionen) bedarf es stabil arbeitender Fallen, die gut charakterisiert sind. Auerdem benötigt man eine zuverlässige Methode, die Information zwischen den Ionen zu teilen und zu übertragen.

In dieser Arbeit werden der Aufbau und die Resultate zweier Experimente mit segmentierten Ionenfallen präsentiert. Zum Einen wurden Ionen als Sensoren für elektrische Felder verwendet, was eine neuartige Diagnostik ermöglicht. Mit dieser Methode konnten lichtinduzierte Ladungen auf Oberflächen der Ionenfalle mit einer Genauigkeit von 40 Elementarladungen pro $\sqrt{\text{Hz}}$ nachgewiesen werden. Desweiteren konnte durch eine direkte Kopplung zweier Fallenbereiche eine mögliche Umsetzung fr die Verteilung von Quanteninformation in multiplexen Fallen erforscht werden. Dabei wurde ein kohärenter Austausch von Bewegungszuständen zweier Ionen, die 54 μm voneinander entfernt waren, beobachtet. Die Kopplungsstärke zwischen den Fallenbereichen wurde durch zusätzliche Ionen als Nahfeldantennen verstärkt.

Abstract

A scalable architecture for quantum information processing with trapped ions depends, among other things, on the ability to store and manipulate large numbers of ions within a single processing unit, i.e. the ion trap. To reliably control the ions these traps must be stable and well characterised. Furthermore, reliable ways of sharing the information between the ions have to be developed.

This work presents the development of and the results from two segmented-trap experiments. First, the ions are used as electrical-field probes which serves as the basis for a novel diagnostic tool. With these probes light-induced charging of trap structures was observed with a sensitivity of 40 elementary charges per $\sqrt{\text{Hz}}$. Second, a way to share quantum information in a multiplexed trap structure by direct coupling between two trapping sites is presented. A coherent exchange of the motional states between two ions, separated by 54 μm, was observed. The coupling strength between these two trap sites was increased using additional ions as near-field antennae.

Contents

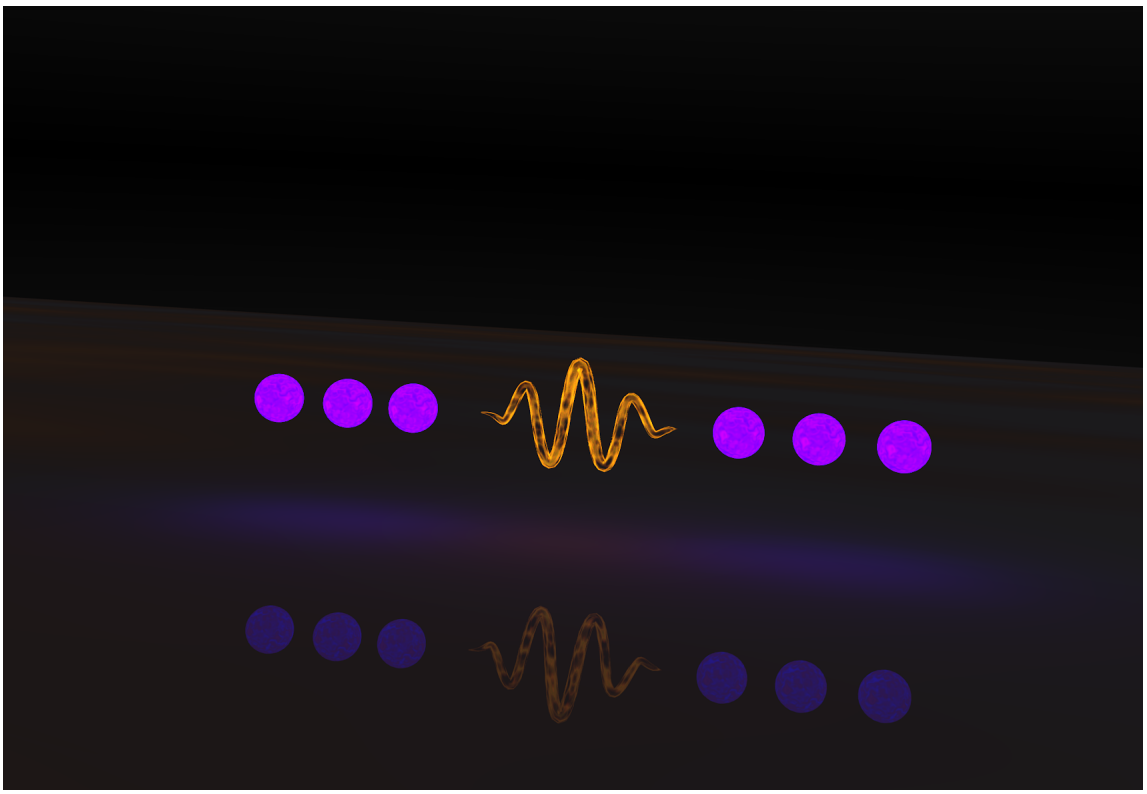

Figure 1: *"Trapped-ion antennae" by Morgan Frey*

Chapter 1

Introduction

More than one hundred years ago, in 1890, Heinrich Hertz first succeeded in transmitting signals over a few metres using an electromagnetic oscillator and thus proving the theory of electromagnetism developed by James C. Maxwell [1]. Since then, technology has advanced so far that electromagnetic signals are used in daily life. Radio stations transmit the latest news and music to local receivers, and even visual signals are sent around the world with improved versions of Hertz's invention. Communication is possible with cell phones sending and receiving the signals at almost any point in the world.

A few years after Hertz's experiments, the theory of quantum mechanics began being developed, and research of quantum systems became increasingly interesting, in theory and experiment. During these decades, understanding of quantum mechanical systems grew and the behaviour of small systems such as single atoms could be well described by this theory. With the increased understanding of quantum mechanics and the progress of experimental techniques, there arose the need for simulations of classically unpredictable quantum systems of growing size. Today, faster computers allow numerical simulations of such systems with a rising number of parameters. However, to date these simulations are still limited to a relatively small number of quantum particles.

In the early 1980s, Paul Benioff and Richard Feynman postulated the idea of using a quantum mechanical system as a quantum computer to calculate such systems [2, 3]. Research began for a viable candidate system of quantum bits (qubits), and to date there exists a variety of possible physical realisations. A comprehensive review about the goals and implementations of quantum information processing and its advantages over classical computing is given in the European roadmap on QIPC [4]. While a classical computer divides information into fundamental pieces of information, called bits, that can take the value of 0 and 1, a quantum computer [5] uses a quantum mechanical two-level system, a qubit, that can take any superposition of the two levels $|0\rangle$ and $|1\rangle$. A qubit could be represented by a spin-$\frac{1}{2}$ particle or a two-level atom, and the information stored in one qubit exceeds the one stored in a classical bit, since not only the amplitudes of the two states are stored but also the phase information. The higher density of information stored in the qubits as well as the possibility of entanglement between qubits enable quantum computers to compute algorithms that classical computers are not capable of computing,

e.g. Shor's factorising algorithm [6]. In 2000 David DiVincenzo postulated seven criteria that are needed for realising a quantum computer [7]:

1. A scalable physical system with well characterized qubits
2. The ability to initialize the state of the qubits to a simple fiducial state, such as $|000...\rangle$
3. Long relevant decoherence times, much longer than the gate operation time
4. A universal set of quantum gates
5. A qubit-specific measurement capability
6. The ability to interconvert stationary and flying qubits
7. The ability to faithfully to transmit flying qubits between specified locations

To date, trapped ions are at the forefront of quantum computation, as they fulfill most of the DiVincenzo criteria. However, one in particular stands out as providing many open challenges: scalability. During the endeavour of scaling up ion-trap quantum computers it became clear that one single quantum register with lots of ions would be physically unworkable. However, it may be possible to use many smaller quantum registers and have the information shared among them. This requires the transport of quantum information between the registers.

In this work, Hertz's idea is taken into the quantum world, where ions are used as near-field antennae to increase the speed and hence the quality of this information transport. The experiments show direct coupling between the motional dipoles of separately trapped ions over a distance of 54 μm, using the dipole-dipole interaction as a quantum-mechanical transmission line [8]. This interaction is small between single trapped ions, but the coupling is amplified by using additional trapped ions as near-field antennae. With three ions in each well the interaction is increased by a factor of seven compared to the single-ion case. This enhancement facilitates bridging of larger distances and relaxes the constraints on the miniaturisation of trap electrodes. This represents a new building block for quantum computation and also offers new opportunities to couple quantum systems of different natures.

This thesis is structured as follows: in chapter 2 an overview on ion traps is given. First the principles of traditional radio-frequency traps for ions and their limitations are introduced. This is followed by descriptions of the two modern segmented trap designs that were used in this thesis. Chapter 3 gives a review of the basic principles of quantum computation with trapped ions. After a general introduction into atom-light interactions and its usage for qubit manipulations, a summary of the achievements of trapped-ion quantum computers is listed. The chapter ends with an introduction of possible ways to render this technology scalable. The experiments in this work were carried out in two separate traps: one planar trap, "Bastille", and one two-layer sandwich trap, "Micreon". These traps and the related experimental infrastructure are described in chapter 4. Chapter 5

describes two experiments in the planar trap, where trapped ions are used as electric-field probes. In the first experiment, a long string of ions is used to map the axial potential of the confining trap. In the second experiment, the ions are used as probes for laser-light induced charging effects on dielectric surfaces. These experiments provide a valuable tool for diagnostics of new ion traps on the one hand, and on the other hand demonstrate further possible applications of trapped ions in different fields of research. Chapter 6 presents the quantum information experiments done in a segmented two-layer trap. At first, a fast cooling method is presented with which the ions can be cooled below the Doppler limit. Then the characteristics of the newly set-up apparatus, including heating rates and coherence times, are shown. Finally, the coherent coupling between two trapping sites and its amplification with ions as near-field antennae is demonstrated, followed by an outlook about possible future gate in these coupled systems. The final chapter 7 gives a summary of this thesis.

Chapter 2

Scalable ion traps

This chapter is focused on the technology of scalable ion traps. Based on the mass spectrometer invented by Wolfgang Paul [9], *Paul traps* use radio-frequency (RF) fields to trap charged particles; in the case considered here, atomic ions. The first section of this chapter will give a review of traditional linear Paul traps, which are currently used successfully as the basis for quantum computation. In the second section the idea of miniaturised segmented ion traps is presented with some considerations about the challenges of physical realisations. The last part of this chapter is dedicated to the consideration of two different trap geometries (two-layer and planar traps) including their respective advantages and disadvantages, depending on the application for which they are used.

2.1 Radio-frequency traps for ions

In an idealised linear Paul trap ions are trapped radially by applying an RF voltage $V_{1,2} = \pm\frac{1}{2}V_0\cos(\Omega t)$ to the diagonally opposing pairs of four electrodes (see figure 2.1) [10, 11]. Axial confinement is created by a DC voltage apllied to the endcap electrodes. Considering only the RF voltage, this creates a time-dependent, two-dimensional quadrupole field that traps a charged particle at its saddle point. For hyperbolically shaped electrodes this potential in the x-y-plane takes the form

$$\Phi(\vec{r},t) = V_0\cos(\Omega t)\frac{x^2-y^2}{r_0^2} \tag{2.1}$$

where r_0 is the minimum distance from the trap center to the electrodes. For improved optical access the electrodes in real traps are usually not hyperbollically shaped. However, for small excursions from the trapping minimum the potential of equation 2.1 is still valid except for a dimensionless geometrical efficiency factor, ε: $\Phi_{\text{eff}}(\vec{r},t) = \varepsilon\Phi(\vec{r},t)$. The equations of motion for charged particles with mass m and charge e in this potential have

a special form of the *Mathieu equations*.

$$\begin{aligned} \frac{d^2x}{dt^2} - 2qt\frac{\Omega^2}{4}\cos(\Omega t)x = 0 \\ \frac{d^2y}{dt^2} + 2qt\frac{\Omega^2}{4}\cos(\Omega t)y = 0 \end{aligned} \tag{2.2}$$

where $q = \frac{2e\varepsilon V_0}{mr_0^2\Omega^2}$ is called the stability parameter. Stable trapping is possible for values of $0 < q < 0.908$ [12]. The solutions of equation 2.2 can be separated into two motions. One is a fast oscillation at the trap drive frequency, Ω, and is called *micromotion*. The other is a slow *secular* motion around the trap center with a frequency $\omega_r = \omega_x = \omega_y = \frac{\Omega q}{2\sqrt{2}}$. These slow harmonic oscillations are those of a particle in a pseudo-potential of the form

$$\Psi_{\text{pseudo}} = \frac{e^2}{4m^2\Omega^2}|\nabla\Phi_{\text{eff}}(\vec{r})|^2 \tag{2.3}$$

where $\nabla\Phi_{\text{eff}}(\vec{r})$ is the instantaneous electrical field when $V_{1,2} = \pm\frac{1}{2}V_0$, i.e. $\cos(\Omega t) = 1$.

The radial potential given in equation 2.1 provides confinement in two directions (x and y) but no axial confinement (z direction) of the ions. The axial confinement is achieved by applying a static voltage on the endcap electrodes. The motional frequency of this harmonic confinement must be much smaller than the radial frequencies, $\omega_z \ll \omega_{x,y}$, to achieve a linear string of ions [13]. Besides providing axial confinement, the endcap voltage has a defocusing effect on the radial confinement, which can be included into the *Mathieu equations*, and has the effect of reducing the range of stable q-values. This is described in detail elsewhere [14, 15]. Due to the symmetric geometry of the traps shown here, it is necessarily true the the saddle points of the DC field and the RF field coincide. In real traps, where this symmetry is broken by imperfections or by design, it must be ensured that the saddle points of the two fields still overlap. Otherwise, the amplitude of the micromotion can be excessive. The process of overlapping the fields is thus called "micromotion compensation" and may require additional DC electrodes.

In a real experiment the voltage $V_{rf} = V_0\cos(\Omega t)$ is applied only to one electrode pair while the other pair is held at ground. If the endcap electrodes are neglected this results in the same equations of motion as only a space independent oscillating potential is added which has no influence on the ions. Taking the endcap electrodes into account lifts the degeneracy of the secular motions as the radial symmetry is broken by the endcap electrodes (they are still at a constant potential, the space independent potential is not added to them). Depending, therefore, on the trap drive frequency Ω, the amplitude of the RF voltage V_{rf} and the applied endcap voltage V_{endcaps}, an ion will have three generally different motional frequencies ω_x, ω_y and ω_z. Assuming that any RF confinement in the axial direction is negligible these are related by $\omega_x^2 + \omega_y^2 + \omega_z^2 = \Omega^2 q_0^2/4$, where q_0 is the stability parameter for the unmodified RF pseudo potential.

In a linear harmonic trap the number of ions that can be stored and operated on is limited. The reason for this is as follows. For quantum information processes, high axial frequencies are required as they define the timescales of gate operations that include the motional bus (see chapter 3.1.4). Due to the Coulomb repulsion of the positively charged

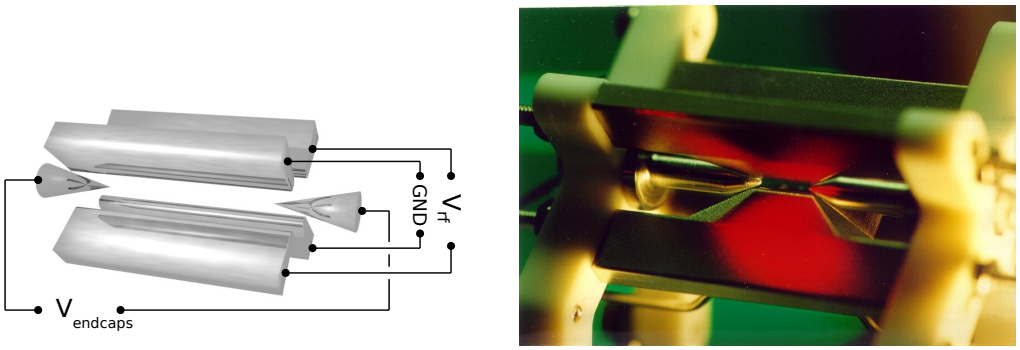

(a) **(b)**

Figure 2.1: *A schematic (a) and a photograph (b) of a linear Paul trap as used in Innsbruck. A radio-frequency voltage $V \sim$ is applied to one opposing pair of blade electrodes while the other pair is held at ground. The resulting time varying, two-dimensional quadrupole field radially confines charged ions to the longitudinal axis. The confinement along the trap axis is generated by voltages at around $V_{\text{endcaps}} = 1000\ V$ on the two endcap electrodes.*

ions, their inter-ion distances at equilibrium decrease with the number, N, of ions. The distance between two ions in a string of ions trapped in a harmonic trap is smallest in the centre of the string. A numerical analysis of the minimum distance, Δz_{min}, between two ions for a string of n ions gives [16]:

$$\Delta z_{\text{min}} \approx 2.0 \cdot \left(\frac{e^2}{4\pi\epsilon_0 m\omega_z^2}\right)^{\frac{1}{3}} \cdot n^{-0.57}. \tag{2.4}$$

Therefore, the increasing the number of ions within one harmonic trap at a constant, high trapping frequency runs counter to required techniques of quantum information processing, such as single-ion addressing with laser beams. Furthermore, the minimum radial confinement ω_r for a linear configuration of the ion crystal also increases with the number of ions. This radial confinement, however, is limited due to the stability parameter by the maximum practical values of Ω and V_{rf}. Segmented ion traps offer a solution to these issues. These traps allow the shaping of the axial potential into non-harmonic traps, e.g. by allowing the creation of anharmonic traps in which a long string of equally spaced ions can be confined [17] or periodic potentials or even more complex structures [18]. These potentials can even be changed in time to allow the splitting of one well into two, the merging of several wells into one, or the moving ("shuttling") of wells to different positions along the trap axis. Moreover, scaling up the number of ions could be even further improved with structures that allow trapping of two-dimensional arrays [19]. Various realisations of segmented traps are presented in the following.

2.2 Segmented traps as a scalable architecture

The general idea for scalable ion traps is to slice the grounded blades of a linear trap into small individually controllable electrodes. This allows tailoring of axial potentials and thereby, for example, creation of many separate trapping sites within one trap [18]. Recent trap designs have evolved into two general structures: Multi-layer designs have a similar geometry to the linear Paul trap electrodes built in a three-dimensional structure. Alternatively planar or surface traps have all electrodes placed in one plane.

In this section these two different trap geometries, both of which have been used for the experiments of this thesis, are discussed. Figure 2.2 shows the schematics for these two trap types. The first is a two-layer trap design which is similar to the geometry of a linear blade trap with a three-dimensional radial cross-section. The second is a surface or planar trap design where the electrodes are all within one plane. The RF pseudo potential minimum is then formed above the surface in free space. In the following, the properties of these two trap geometries are discussed.

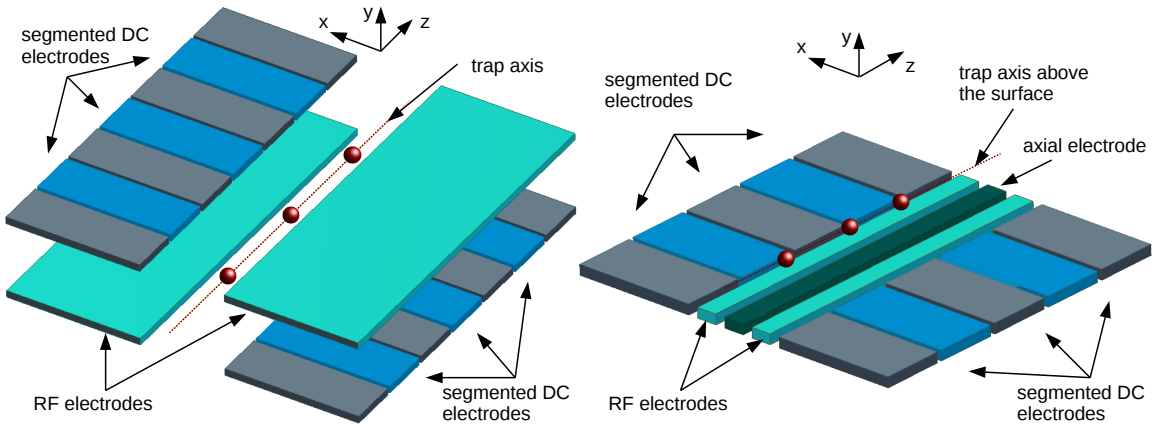

Figure 2.2: *Schematics of two scalable segmented trap geometries: (a) two-layer trap and (b) surface geometry.*

2.2.1 Two-layer traps

To achieve a geometry similar to that of a Paul trap, the electrodes are arranged in two parallel planes, each plane comprising an RF electrode and a series of segmented DC electrodes as illustrated in figure 2.2a. This structure is often achieved by metal coating two separate substrates, which are separated by a spacer layer. To date, there have been various attempts to create such a structure [20–22] including monolithic procedures and sandwich type arrangements of two individually produced chips [23]. Following the DiVincenzo criteria, the quantum system that is used as a qubit must be isolated from the environment to prohibit any information leaking into that environment and leading to

decoherence. A two-layer trap design, where the trapping axis lies between the electrode layers, shields the ions from possibly disturbing fields from outside. Additionally, as the electrodes sit close to the optimal quadrupole positions, the resulting RF pseudo potential yields high trap depths and frequencies. Furthermore, the symmetry of the electrodes simplifies the control of the electrode voltages. Therefore, such a geometry is well suited as a quantum computation processor. However, despite the possibility to create junctions and crossings with multi-layer trap designs [24, 25], scalability is limited as networks of junctions are complicated to manufacture and operate. Despite the limitation of scalability, these trap structures provide a suitable route for initial experiments involving new methods of scalable quantum computation in one dimension. Experiments in such a trap are described in chapter 6 of this thesis.

2.2.2 Surface traps

All electrodes of this kind of trap are arranged in one plane as illustrated in figure 2.2b. For a linear trap there are usually five rows of electrodes: two connected to the RF source, one DC electrode between the two RF electrodes, here referred to as the *axial electrode* and then two series of segmented DC electrode on the outer sides. Fabrication of planar traps can be done directly with standard microfabrication techniques by coating a substrate with metal while a mask defines the structure of the electrodes. This process can be much less complicated than the processes needed for multi-layer traps. The traps can thus be manufactured on a short timescale allowing rapid optimisation of the geometry, electrode materials, surface quality and treatments. Additionally, scalability with two-dimensional trapping arrays can be more easily achieved as the manufacturing process of the required structures is straight forward. Such two-dimensional traps have been already realised [19, 26, 27]. Due to the open access from above, the ions are more susceptible to electrical fields from the environment. This higher susceptibility of the ions to small electrical field changes can be used as a probe of these fields [28].

However, the open structure of these kinds of traps generates some issues that may need special attention when using them for quantum information processing. The fact that the trap minimum sits above the plane of the electrodes (see figure 2.2b) leads to an increased anharmonicity of the trapping potential in the direction perpendicular to the surface and a lower trapping depth compared to a two-layer trap with similar size and voltages applied. One possibility to enhance the confinement is given by placing an optically transparent, electrically conducting mesh above the ion trap. This solution not only increases the confinement but also shields the ions from disturbing electrical fields from the environment. Another issue of planar traps is that for a geometry symmetric about the y-z plane, as shown in figure 2.2b, the principle axes of the two radial modes are perpendicular and parallel to the trap surface. As the cooling laser beam is required to have an overlap with the direction of the oscillation mode and the laser must run parallel to the trap surface, the perpendicular radial mode cannot be cooled efficiently. There are two ways to circumvent this issue. One is using an asymmetric width of the RF electrodes, which leads to a shift of the RF null to one side. The micromotion compensated DC potential, which creates the axial confinement, thus tilts the principal RF axes. The other

possibility is to split the axial electrode (figure 2.2b) along the trap axis into two separate electrodes. Applying two different voltages to these two electrodes also results in a DC confinement with tilted radial axes. A trap of this design is presented in chapter 5. There, advantage was taken of the open structure of this trap to measure electrical fields with the ions as probes.

2.3 Technical considerations about ion traps

Ion trapping for quantum information processing is technically challenging. The quality of an ion trap can be characterised by, among other things, the degree to which two disturbing effects are suppressed: the ion heating and the ammount of micromotion (see section 2.1). These two effects are described in the first part of this section. In light of this, the second part describes some of the technological demands that should be considered to achieve a scalable, stable and controllable ion-trap design. Special focus is on the challenges that arise due to the segmentation and miniaturisation of the ion traps.

2.3.1 Unwanted pertubative effects

Ion heating. Following the DiVincenzo criteria for a quantum computer, the qubit is required to be well-enough isolated from the environment that decoherence occurs on timescales much longer than the time needed for the algorithms. Otherwise, any incoherent interaction with the environment would lead to decoherence of the information stored or processed in the system. During entangling gates, the information is shared between the ions via the common motional state. The stringency of the requirements on the excitation of this motional state varies, depending on the gate employed. For example the Mølmer-Sørensen (MS) gate operation requires a low motional state occupation $\bar{n} \lesssim 20$, while the Cirac-Zoller (CZ) type gate operation even requires the ground state, $\bar{n} = 0$. Furthermore, any externally driven change of the motional state during the gate operations will decrease the coherence of the system. An important value therefore is the heating rate of an ion in a trap. This is given by the mean number of phonons that the ions gain per unit time, $\dot{\bar{n}}$. In the ideal case the timescale of the creation of one phonon due to heating should be much longer than the time needed to perform the quantum operations. The heating is generally caused by electrical noise, that drives the motion of the charged ions within the trap. Possible noise sources are believed to be technical noise (e.g. Johnson noise) and so called *anomalous* heating due to patch potentials on the electrode surfaces [29]. While the heating rate due to technical noise would scale with the inverse square of the characteristic scale of the trap, anomalous heating rates are expected to show a d^{-4} dependence [30].

Micromotion. Another issue with the stable trapping of ions is micromotion; the fast oscillation at the trap drive frequency. As this is a coherent oscillation with the RF drive of the trap, it does not, of itself, introduce heating. However, if the ions are laser cooled, these motional changes are out of phase with the micromotion and can result in a lower cooling efficiency and a higher final temperature. Additionally, the coupling to the carrier

transitions is reduced by the presence of micromotion as it also generates sidebands. The amplitude of the micromotion depends on the amplitude of the RF electric field that the ions experience. The minimal amount of micromotion occurs when the ions are situated on the saddle of the RF potential. This can be achieved by ensuring that the saddles of the RF potential and the DC potential coincide. Usually compensation voltages are applied to additional electrodes for this purpose. Any scalable trap architecture must therefore not only incorporate sufficient electrodes to trap ions, but also have sufficient degrees of freedom to compensate for micromotion.

2.3.2 Demands on controllable and scalable ion traps

Miniaturisation of trap geometry. The size of a trap, i.e. the distance of the ions to the closest electrode, is an important feature, on which many technological demands depend on. Smaller trap sizes are favourable for several reasons. One is the lower RF amplitude and electrode voltages needed in order to realise higher secular frequencies. Secondly, deterministic splitting and merging of ion strings requires high local curvatures of the axial potentials. This in turn necessitates small electrode sizes for creating these potentials. However, if the scale of the electrodes is small compared to the ion-electrode distance, the axial potential created by the electrode at the ion's position is similar to the one of a point charge, and any further reduction of the electrode size would not increase the local curvature any further. This results in a optimal electrode size dependent on the trap dimension. As a rule of thumb this size is on the order of the ion-electrode distance [31]. Any further increase of the local curvatures of the axial potential requires either a smaller trap geometry or very high voltages. In the experiments presented in chapter 6, a double-well potential with a distance of $\sim 50\,\mu$m could be created with electrodes with a width of $250\,\mu$m using the latter method.

Despite the advantages of small trap geometries, it is not feasible to make traps arbitrarily small. The rate at which the ions are heated increases with decreasing trap size [29, 30]. The laser light required to interact with the ions cannot be focused to arbitrary small spot sizes, and practical methods of fabrication on different length scales must be taken into account. Each of these issues is now addressed in term.

Optical access. In an ion-trap quantum computer, as it is described in this thesis, cooling, state manipulation and state detection are done by interaction of the ions with laser-light. Therefore optical access to each trapping zone is desired. This includes especially access for the laser beams needed to drive qubit transitions. And additionally single-ion addressing on each ion is also needed for individual qubit rotations and can be realised with a single strongly focused beam either by shifting the ion string or the laser beam. Focusing of the laser beam down to a beam waist of a few microns requires the use of optics with a high numerical aperture close to the ions. Otherwise, optical errors can result in addressing errors, that can be compensated for in a similar way to spin refocusing as performed in NMR experiments [32]. However, this in turn increases the overhead of needed operations. The optical elements in close vicinity of the ions are usually dielectrics, e.g. fused silica lenses coated with dielectric anti-reflective coatings. Any charges, that

may accumulate on the dielectric surfaces, thus remain there and frustrate the efforts to minimise micromotion or stabilise the ions' positions. The second experiment in chapter 5 focuses on these charging effects and shows a method using trapped ions to measure it.

Manufacturing. The manufacturing process of an ion trap is another possible challenging issue, especially for multi-layer trap geometries. Depending on the desired trap size, there are different machining procedures available. Precision macroscopic machining technologies can reach down to sizes of a several hundred micrometres. Monolithic technologies are optimised for structures at sizes of between a few nanometres up to a few hundred nanometres. For trap geometries with sizes in the range a few tens of micrometres laser cutting techniques are a possibility. The trap presented in chapter 6 was built by laser cutting. For surface traps, large structures ($> 100\,\mu$m) can be fabricated using standard printed circuit board (PCB) techniques. Smaller structures ($> 20\,\mu$m) require more advanced PCB prototyping. Photo lithographic techniques while being more involved can provide resolution of electrodes down to $\sim 1\,\mu$m, and offer the possibility of more complex structures [33].

Depositions on the trap's electrodes. During the loading procedure, a thermal beam of atomic calcium is sent through the trap. As the trap size is reduced, it is possible that calcium gets deposited on the trap structure. The calcium could short narrow insulating gaps between two adjacent electrodes. Furthermore, the galvanic potential between calcium and the electrode material could lead to stray fields which, for example, would prevent stable micromotion compensation. Other loading mechanisms, e.g. pulsed lasers ablation of a calcium target [34] or backside-loading of surface traps, could prevent these issues if necessary. However, at the present time the systems used in this thesis are not limited by such effects. Therefore these technically more demanding procedures are not necessary, but are mentioned for the sake of completeness.

2.4 Summary

In this chapter the principles of ion traps based on Paul's mass spectrometer were described. After introducing the standard linear Paul trap, the idea of scalable segmented traps and two possible realisations of which are presented. These two trap geometries were used for the experiments presented in this thesis in chapter 5 and 6. In the end, an overview of possible issues that should be taken into account when designing a new scalable ion trap is given.

Chapter 3

Scalable quantum information processing with trapped-ion systems

As this work is about scaling up trapped-ion based quantum computation, the following chapter reviews possible ways to achieve this scalability. The first section gives a review of quantum computation, its requirements and a general introduction to the realisation with trapped ions. After the basics, the second part of this chapter focuses on possibilities, how ion-trap quantum computation might be rendered scalable.

3.1 Review of trapped-ion quantum information processing

In this work, the qubits of the quantum computer are realised using the electronic states $|S\rangle$ and $|D\rangle$ and the motional phonon states of singly charged $^{40}Ca^{+}$ ions. The quantum state is manipulated with coherent laser-light illumination to drive optical dipole and quadrupole transitions. This section provides an overview of the necessary background for how quantum computation is carried out using trapped $^{40}Ca^{+}$ ions. Section 3.1.1 starts with introducing the $^{40}Ca^{+}$ ion and its level structure. By considering only two of these levels, the ion can be considered as a two-level atom. The interaction of such a two-level atom, trapped in a harmonic potential, with laser light is given in section 3.1.2. Dissipative interactions can be used to prepare the ion in or near the motional ground state, i.e. cool the ion. Furthermore they can be used for state detection (section 3.1.3). The electronic and the motional state of the ion can also be manipulated in a coherent way. This can serve technical purposes, such as using coherent operations to measure the motional state and heating rate of an ion. The electronic and motional states also serve as qubits storing the quantum information. The coherent manipulation of these states thus allows quantum information processing (section 3.1.4). Multiple-qubit operations are realised by using the motional state as a bus to mediate interactions between electronic qubits. Finally, section 3.1.5 surveys the current state of the art in trapped-ion quantum

computation. More detailed information can be found in the theses by Christian Roos [14], Mark Riebe [35] and Jan Benhelm [36].

3.1.1 $^{40}Ca^{+}$, the ion species used in Innsbruck

A singly ionised earth-alkali atom has a similar energy level scheme to a neutral alkali atom and is comparable to the structure of atomic hydrogen as one valance electron orbits a nucleus with effectively one positive elementary charge. A diagram of the five lowest energy levels with the corresponding transition wavelengths and lifetimes is shown in figure 3.1. The lowest energy level is the $4^2S_{1/2}$ state, the next higher levels are the

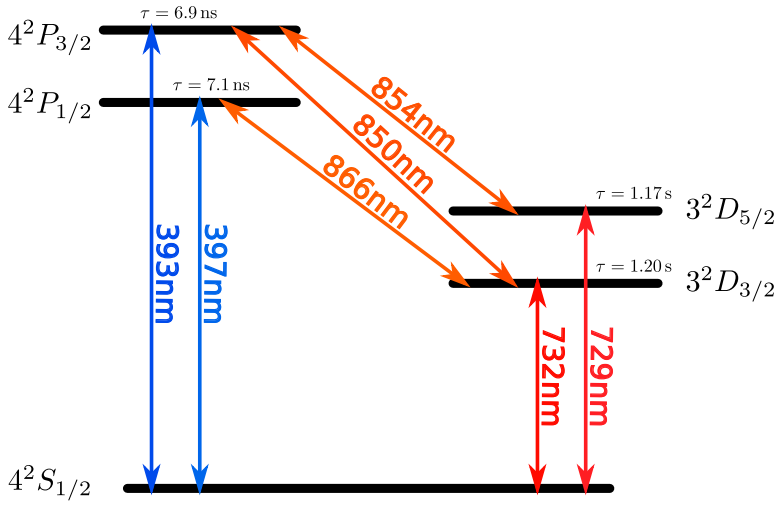

Figure 3.1: *Level scheme of* $^{40}Ca^{+}$ *including the wavelengths of the transitions and the life times of the excited states. The* $S_{1/2} - P_{1/2}$ *dipole transition at* 397 nm *is generally used for Doppler cooling and detection. Laser light at* 866 nm *is used to repump populations that decayed from the excited* $P_{1/2}$ *state into the* $D_{3/2}$ *state during Doppler cooling and detection. The qubit states are usually* $S_{1/2}$ *as* $|1\rangle$*-state and* $D_{5/2}$ *as* $|0\rangle$*-state. They are manipulated with laser light at* 729 nm *on a quadrupole transition. For fast re-initialisation of the qubit's state, repumping light at* 854 nm *pumps the populations of the* $D_{5/2}$ *state into the* $P_{3/2}$ *where they then decay to the ground state within nano seconds. The other transitions are not of interest in this thesis, but are shown for the sake of completeness.*

$3^2D_{5/2}$ and the $3^2D_{3/2}$ which are energetically split by spin-orbit coupling. There are no lower lying states to which the ion can decay via dipole transition and no dipole transition to the $4S$ state is allowed. Therefore the 3^2D states are metastable and their lifetime is roughly one second. However, strong laser radiation can couple the S and D states by quadrupole excitation at wavelengths of 729 nm and 732 nm. In this work, the qubit states are encoded in the $S_{1/2}$ and $D_{5/2}$ states. The next levels are the $4^2P_{1/2}$ and $4^2P_{3/2}$. The $S_{1/2} - P_{1/2}$ dipole transition is usually used for Doppler cooling and state detection with a laser at 397 nm. Due to the dipole allowed decay from $4^2P_{1/2}$ to the metastable $3^2D_{3/2}$ states with a probability of about 1 per 17 decays [37], repumping with 866 nm

light is required during the cooling and detection periods. Populations of the $3^2D_{5/2}$ can be brought back fast into the ground states by repumping with 854 nm light to the $P_{3/2}$ state from which it then decays via a dipole transition to the ground state within a few nano seconds.

3.1.2 Atom-light interaction in a harmonic trap

The interaction of a trapped atom or ion with laser light can be described by considering only two energy levels (either $|S\rangle$ and $|D\rangle$) of the atom split by $\hbar\omega_0$. This effective two-level system can be driven at (or near) resonance by laser light at frequency $\omega_L = \omega_0 - \delta$, with δ being the detuning. The ion is further held in a harmonic trapping potential. The quantised motion can take energy values $\hbar\omega_{\text{trap}}(n + \frac{1}{2})$, where n is the phonon number. The Hamiltonian for this systems consists of three parts: the one for the internal atomic states, H_{atom}, the one for an ion trapped in a harmonic trap, H_{trap}, and the one for the interaction between the ion and the light, H_{L}:

$$\begin{aligned} H_{\text{atom}} &= \frac{1}{2}\hbar\omega_0\sigma_z \\ H_{\text{trap}} &= \frac{\hat{p}^2}{2m} + \frac{1}{2}m\omega_{\text{trap}}^2\hat{x}^2 \\ H_{\text{L}} &= \frac{1}{2}\hbar\Omega(\sigma^+ + \sigma^-)\left(e^{i(k\hat{x}-\omega_L t+\varphi)} + e^{-i(k\hat{x}-\omega_L t+\varphi)}\right). \end{aligned} \tag{3.1}$$

Here, $\hat{x}$ and $\hat{p}$ denote the space and momentum operators of the particle of mass m in the harmonic trap, $\sigma^{\pm}$ and σ_i are the Pauli spin matrices and k is the wave vector of the light. The laser's intensity and its coupling strength to the ion are included in the Rabi frequency Ω. The system's time dependence can be derived by introducing the Lamb-Dicke parameter $\eta = k\sqrt{\frac{\hbar}{2m\omega_{\text{trap}}}}$ and changing into the interaction picture and applying the rotating wave approximation [38]. The Hamiltonian for the interaction takes the form

$$H_I = \frac{1}{2}\hbar\Omega\left(e^{i\eta(\hat{a}+\hat{a}^\dagger)}\sigma^+ e^{i\delta t} + e^{-i\eta(\hat{a}+\hat{a}^\dagger)}\sigma^- e^{-i\delta t}\right) \tag{3.2}$$

with $\hat{a}^{(\dagger)} = e^{i\omega_0 t}a^{(\dagger)}$ with $a^\dagger$ and a being the creation and annihilation operators replacing $\hat{x}$ and $\hat{p}$.

The ion's electronic and motional state is usually denoted as $|S, n\rangle$ or $|D, n\rangle$. Depending on the detuning δ it is possible to couple the ion's electronic and motional states via the laser light. This can be done because, in the ion's rest frame, the laser light is frequency modulated with the trap frequency. Calculation of the time evolution of a state $\Psi = \sum_n (c_n |S, n\rangle + d_n |D, n\rangle)$ results in the Rabi frequency for a transition from the motional state with n phonons to the one with n' phonons

$$\Omega_{n,n'} = \Omega || \left\langle n' \right| e^{i\eta(a+a^\dagger)} |n\rangle ||. \tag{3.3}$$

The Lamb-Dicke regime is defined by $\eta^2(2n + 1) \ll 1$. It represents the situation where the size of the motional wavefunction of the atom is much smaller than the wavelength

of the interrogating light field. In this regime, transitions changing the motional state by more than one phonon are suppressed and can be neglected. The Rabi frequency for the remaining red- and blue-sideband transition can then be simplified (figure 3.2):

$$\begin{aligned} \Omega_{\text{red}} &= \Omega_{n,n-1} = \Omega\eta\sqrt{n} \\ \Omega_{\text{blue}} &= \Omega_{n,n+1} = \Omega\eta\sqrt{n+1}. \end{aligned} \tag{3.4}$$

It should be noted that these transition strengths vary as a function of the motional state of the ion. If the motional state does not change, the so-called carrier transition, the Rabi frequency only weakly depends on the motional state of the atom:

$$\Omega_{\text{carr}} = \Omega_{n,n} = \Omega(1 - \eta^2 n). \tag{3.5}$$

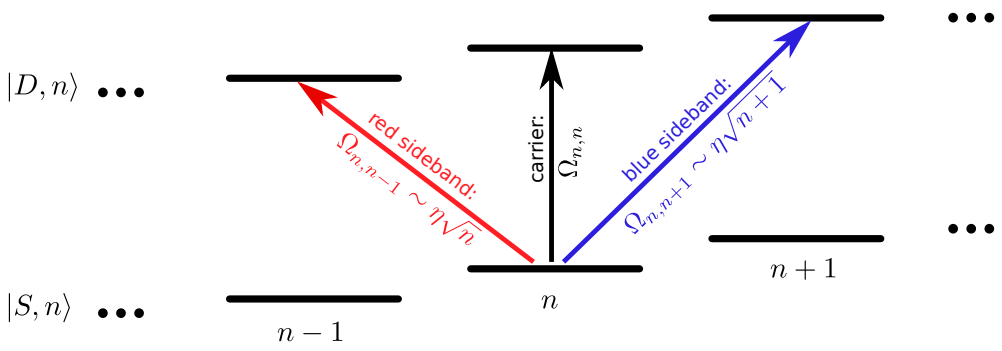

Figure 3.2: *Carrier and first-order sideband transitions of a two-level atom in a harmonic trap. The carrier transition does not change the phonon number. The transition reducing the phonon number is called red sideband, and the one increasing the phonon number is called blue sideband.*

3.1.3 Dissipative interactions: cooling and detection

Cooling of ions to, or close to, the motional ground state is one requirement for achieving high fidelity quantum-state manipulations as the Rabi frequency depends on the motional state (see equation 3.5). High thermal populations in the motional state would thus act as *spectator modes*, which would cause a loss of contrast [39]. Laser cooling is a widely-used cooling method. Doppler cooling allows the reduction of the motional energy of the atoms down into the Lamb-Dicke regime and sideband cooling allows further cooling to, or close to, the motional ground state [40, 41]. In this section an overview of Doppler and sideband cooling is given. While the principles of these two cooling methods are similar, they are

applied in two different regimes: Doppler cooling is applied in the *weak-binding regime* or unresolved-sideband regime, where the trap frequency is much smaller than the natural linewidth of the cooling transition $\omega_{\text{trap}} \ll \Gamma$. Sideband cooling is applied in the *strong-binding regime* or resolved-sideband regime, where the trap frequency is higher than the linewidth, $\omega_{\text{trap}} \gg \Gamma$. Detailed descriptions can be found in the thesis of Christian Roos [14] and in further literature [42].

Doppler cooling of an ion with transition linewidth Γ can reach a final energy of

$$k_B T = \frac{\hbar\Gamma}{2}. \tag{3.6}$$

This can also be expressed in the minimum mean phonon number of a thermal state:

$$\bar{n}_{\text{min}} = \frac{\Gamma}{2\omega_{trap}}. \tag{3.7}$$

This Doppler limit can be derived either semi classically [10] or in a quantum mechanical picture [42]. The basic principle is that the confined ion, during its oscillation in the trap, sees in its rest-frame a time dependent Doppler-shifted laser light. By absorbing and re-emitting photons, the ion's momentum can be changed - decrease of momentum can be achieved by either absorbing a carrier photon followed by emission on the blue sideband transition (figure 3.3 a) or by absorption of a photon on the red sideband and emission of a carrier photon (figure 3.3 b). The opposite processes (figure 3.3 c and d) lead to an increase of the momentum. By detuning the laser it is possible to create an imbalance between the cooling and the heating processes such that the ion can either be cooled or heated, i.e. red detuned laser light ($\omega_L < \omega_0$) cools the ion. In our system, close to the Doppler limit the ion reaches the Lamb-Dicke regime, which causes the processes which include higher order changes of the motional to be suppressed as they scale with η^2. The Doppler limit is reached when the net rate of all the heating and cooling processes is zero and it is minimal if the laser light is red detuned by half the natural linewidth of the transition $\delta = \omega_0 - \omega_L = \frac{\Gamma}{2}$.

Sideband cooling requires the system to be in both the Lamb-Dicke regime and the resolved-sideband regime. An illustration of the scheme is depicted in Figure 3.4. It allows the ion to be cooled to the motional ground state with high population probability [43–45]. The cooling laser is tuned to the red sideband of the transition. In the case of $^{40}Ca^{+}$ experiments this is the $S_{1/2} - D_{5/2}$ transition excited by the laser at 729 nm. Each excitation to the upper energy level reduces the vibrational quantum number. Due to being in the Lamb-Dicke regime, a spontaneous emission of a photon and the consequent recoil does not change the motional state. The state $|S, 0\rangle$ is a dark state such that the population will eventually settle in this state. The lifetime of the metastable D-state is about one second, which would result in a very low cooling rate. To overcome this, the $D_{5/2}$ state can be coupled to the short living $P_{3/2}$ state by the repumping laser at 854 nm.

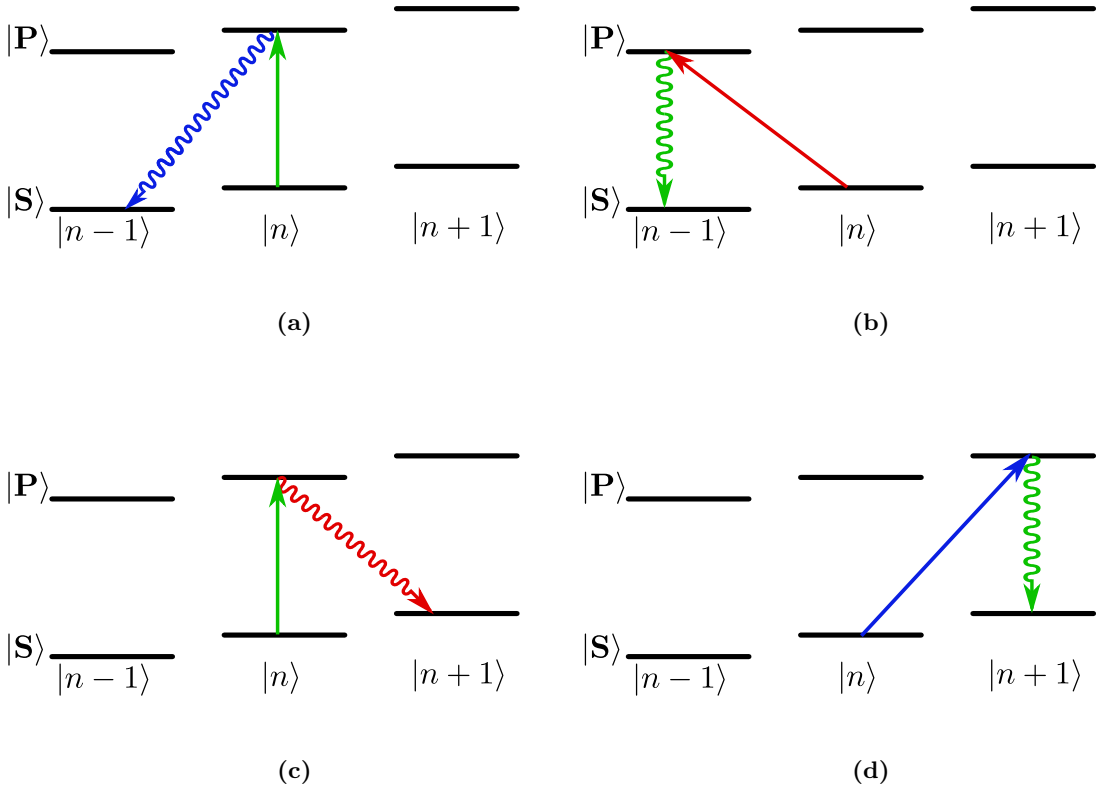

Figure 3.3: *The four main processes that occur during Doppler cooling, if the ion is in the Lamb-Dicke regime. The cooling processes (***a** *and* **b***) reduce the motional quantum number by one while the heating processes (***c** *and* **d***) increase it. The detuning δ of the laser light with respect to the atomic transition defines at which rate these processes take place. Red detuned laser light favours the cooling process (b) and thus cools the ion. The Doppler limit is reached when the overall rates of heating and cooling processes cancel.*

State detection of the electronic qubit is, following the DiVincenzo criteria, required for read-out of the qubit. In this case it is performed by the electron-shelving technique to measure the probability of the ion to be in one of the qubit states, here the $|1\rangle = |\mathrm{S}\rangle$ state. This state scatters photons under illumination with 397 nm light whereas the state $|0\rangle = |\mathrm{D}\rangle$ remains dark. The laser light thus projects any superposition state of the qubit into either the $|\mathrm{S}\rangle$ or $|\mathrm{D}\rangle$ state, with a probability depending on the respective amplitudes in the initial superposition. An ensemble of repeated measurements on many identically prepared systems then reveals the occupation probabilities of the two states. A more detailed treatment of the discrimination process is given in the appendix of [14]. Further literature about complete state measurements, including the phases of superpositions, ("state tomography") is given in the theses of Mark Riebe [35] and Thomas Monz [46].

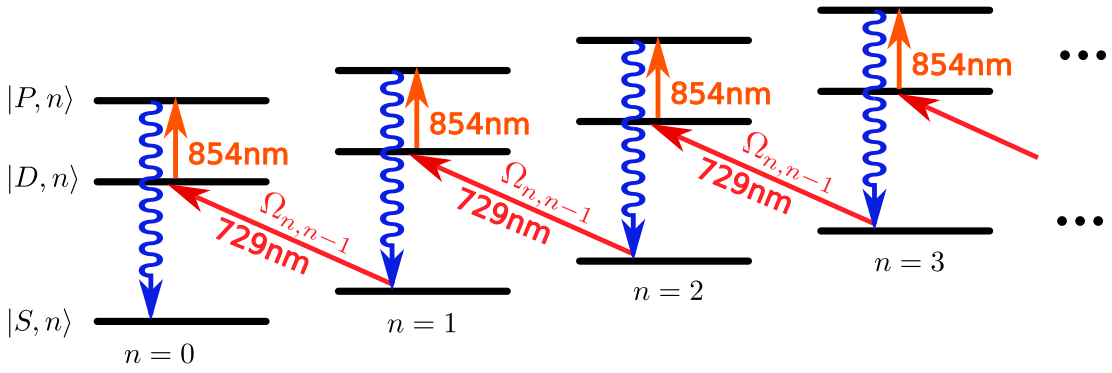

Figure 3.4: *Schematic of the sideband cooling procedure. The excitation with* 729 nm *light on a red sideband* ($\Omega_{n,n-1}$) *from* $|\mathrm{S}\rangle$ *to* $|\mathrm{D}\rangle$ *is accompanied by a reduction of the phonon number by one. The additional repumping laser at* 854 nm *couples the excited* $|\mathrm{D}\rangle$ *state to the* $|\mathrm{P}_{3/2}\rangle$ *state which has a much shorter lifetime than the metastable* $|\mathrm{D}\rangle$ *state. Within the Lamb-Dicke regime the spontaneous decay back to the ground state leaves the motional state unchanged with high probability. The* $|\mathrm{S},0\rangle$ *state is, except for off-resonant excitations, a dark state, such that the population will settle in the motional ground state if no other heating processes occur.*

3.1.4 Coherent state manipulation and multiple-qubit gates

The state evolution under laser illumination can be derived from equation 3.2. This leads to the optical Bloch equations [38]. As a result, the ion's state population under laser-light illumination, resonant with a carrier transition, oscillates between the $|\mathrm{S}\rangle$ and $|\mathrm{D}\rangle$ state with the Rabi frequency $\Omega_{n,n}$ (see equation 3.5). Figure 3.5 shows such Rabi oscillations. Starting from a well-defined state, any superposition can thus be created by applying a pulse of laser light with the corresponding amplitude, frequency and phase for the needed amount of time [35]. The coherent operations can further be used to measure the motional state of the ion, or to create many-qubit gate operations.

Measuring the motional state of an ion One important technical feature of an ion trap is its heating rate; the rate at which the ions increase their mean phonon number. Especially as the motional state is used as a bus to share the quantum information between the qubits, a randomly created phonon during a gate operation may destroy or at least reduce the coherence of the gate operations. One way to measure the heating rate is to determine the motional phonon number of an ion at different times after the ion has been cooled to a low motional state, e.g. by sideband cooling. There are different ways to measure the mean phonon number, depending on how high it is. Most of them rely on the fact that the coupling strength of the atom-light interaction depends on the motional state of the ion (see equation 3.3). Some of these methods are given in the thesis of Christian

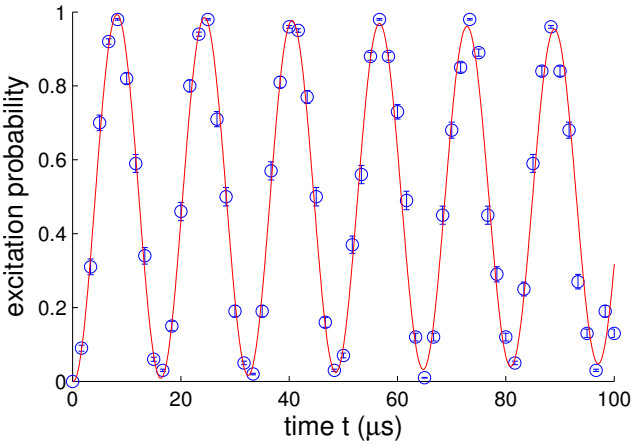

Figure 3.5: *Experimentally measured Rabi oscillations on a carrier transition after sideband cooling on all motional modes (both radial and the axial mode). Shown is the population probability of the* $|\mathrm{D}\rangle$ *state versus the length of the applied laser pulse. Each point represents 100 experiments and the error bars represent the statistical projection noise.*

Roos [14]. One method relies on comparing the height of the red and blue sidebands. The motional state can be found given the different scaling of each sideband with $\bar{n}$ (cf equation 3.4). This method however works only, if the ion is cooled close to the ground state ($\bar{n} < 1$) and the remaining populations are almost only in the two motional states with zero and one phonon. Another motional state measurement can be done with the Rabi oscillations on the carrier transition. For relatively high mean phonon numbers, e.g. after Doppler cooling only, $\bar{n} \approx 5$ or higher, the thermal state occupation leads to an decreasing contrast of the oscillations. This is due to the dependency of the Rabi frequency on the motional state (cf equation 3.5) and can be used to obtain the mean phonon number. This method has been carried out to measure the improved Doppler-cooling method presented in chapter 6.1.1.

In this work, another approach is undertaken, by measuring Rabi oscillations on the red and blue sideband transitions, and simulating them simultaneously to determine the mean phonon number. Considering the ion's motional state to be a thermal distribution, the resulting excitation probability after driving Rabi oscillations for a time, t, would be

$$p_D = \frac{1}{2}\left(1 - \sum_n \rho_n \cos(\Omega\eta_{\mathrm{eff}}\sqrt{n}t/2\pi)\right) \tag{3.8}$$

for the red-sideband transition and

$$p_D = \frac{1}{2}\left(1 - \sum_n \rho_n \cos(\Omega\eta_{\mathrm{eff}}\sqrt{n+1}t/2\pi)\right) \tag{3.9}$$

for the blue-sideband transition. Here, $\eta_{\mathrm{eff}} = \cos(\theta)\eta$, where θ is the angle between the laser beam and the axis of the motional mode and ρ_n is the population of the motional

state with n phonons which is, for thermal states,

$$\rho_n = \frac{\bar{n}^n}{(\bar{n}+1)^{n+1}}. \tag{3.10}$$

With the effective Rabi oscillation frequency on the sidebands, $\Omega_{\text{eff}} = \eta_{\text{eff}}\Omega$, as a free parameter, this technique does not require knowledge of the Lamb-Dicke factor. The Lamb-Dicke factor could be determined by additionally measuring the Rabi oscillation frequency on the carrier transition.

Multiple-qubit operations can be performed by the motional bus since all ions within one trap share the same motional state. This means that the electronic state of one ion can be mapped onto the motional state of all ions within the trap and then be mapped back into the electronic state of another ion. This is the basic principle of the Cirac-Zoller controlled-NOT gate [47, 48]. A different way of entangling gate operations can be performed with bichromatic laser light, for example the Mølmer-Sørensen-type gate [49, 50]. The Mølmer-Sørensen gate operation (see figure 3.6) is performed with a bichromatic light field with frequencies $\nu_\pm = \omega_0 \pm (\omega_{\text{trap}} + \varepsilon)$, i.e. the laser light is detuned by ε from the red and blue sideband of the atomic transition ω_0. This light field couples the $|\text{SS}\rangle$ state of two ions with the $|\text{DD}\rangle$ state, leading to oscillations between the two states, similar to resonant Rabi oscillations. However, a $\pi/2$ pulse with the bichromatic light does not lead to the product state, $(|\text{S}\rangle + |\text{D}\rangle) \cdot (|\text{S}\rangle + |\text{D}\rangle)$, which is a superposition of all four two-ion populations including the $|\text{SD}\rangle$ or $|\text{DS}\rangle$ states. In the bichromatic case the terms of the unwanted $|\text{SD}\rangle$ and $|\text{DS}\rangle$ states interfere destructively resulting in the maximally entangled superposition $|\text{SS}\rangle + |\text{DD}\rangle$.

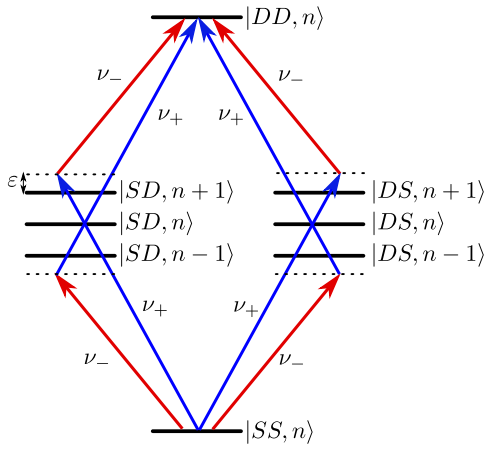

Figure 3.6: *Schematic of a Mølmer-Sørensen interaction with two ions. A bichromatic light field with frequencies close to the motional sidebands, ν_+ and ν_-, couples the $|\text{SS}\rangle$ and $|\text{DD}\rangle$ states. The interaction is only weakly dependent on the motional state.*

3.1.5 Achievements of trapped-ion based quantum computers so far

With such a system of trapped-ions qubits it has been possible to demonstrate numerous quantum logic gates and algorithms. These include a phase gate [51], the Cirac-Zoller controlled-Not gate [48] and the Mølmer-Sørensen gate [52]. Using these gates as building blocks has enabled a variety of different algorithms such as the teleportation of a quantum state [53, 54], entanglement swapping [55], the entanglement of up to 14 ions [56] and repetitive implementation of a quantum error correction scheme [57]. Moreover, with trapped-ion systems, a variety of quantum simulations have been realised: the simulation of the Dirac equation including the 'Zitterbewegung' [58], a quantum random walk [59] and the simulation of open quantum systems [60]. In these simulations, the time evolution of a Hamiltonian under investigation is reproduced by a controllable quantum system, formed by the trapped ions [61, 62]. The level of control demonstrated in such schemes puts trapped ions at the forefront of realisations of quantum computers.

3.2 Scalability of ion-trap based quantum processors

Despite the recent success of trapped-ion quantum simulators and computers, one of the DiVincenzo criteria is not yet fulfilled: scalability. Most of the above-mentioned experiments were carried out with 5 qubits or fewer. An entangled state could be generated with up to 14 ions [56], but the decreasing coherence time with the number of qubits allowed only the generation and measurement of these entangled states. One possible future application of a quantum computer is to factorise large numbers with Shor's algorithm [6], where the time needed scales more favourably with the size of the number to be factorised than any classical algorithm. For example, a k-bit number can be factored in a time proportional to $\mathcal{O}(k^3)$ using a quantum computer with $5k + 1$ qubits [63]. In other words, factoring a 200 digit number would require about 3500 qubits with no error correction implemented. With error correction this rises to 100000 qubits [8]. There is clearly considerable work to be done before such an algorithm is realised on an ion-trap quantum computer. Despite the fact that quantum computers might not surpass classical computers' abilities of factorisation in the near future, they might exceed classical computers in the simulation of quantum systems. To simulate a spin $\frac{1}{2}$ system with n particles, a classical computer would require a memory to store 2^n numbers and has to solve a $2^n \times 2^n$ matrix to evaluate the time evolution of the system [64]. As an example the Cray XT5-HE supercomputer can store the equivalent information of a quantum system with 43 qubits [65]. A universal quantum simulator, where the interaction of the system under investigation can be simulated, could in principle store the information on n qubits.

One limiting factor of scaling trapped-ion quantum computers is the fundamental limit on the number of ions that can be stored and efficiently operated upon within a standard linear Paul trap. Except for ultrafast gates [66] the time needed for entangling gate operations via the motional bus depends on the trapping frequency of the ions. Adding more and more ions into a string in a linear trap at a constant trapping frequency leads to unwanted effects. First, the inter-ion distance decreases with the number of ions which

renders single-ion addressing or readout more and more difficult. Second, the number of motional modes in frequency space increases with the number of ions which leads to spectral crowding and prohibits the addressing of single motional modes. Third, the radial confinement has to be increased to keep the ions aligned in a linear chain without forming a zig-zag configuration. To overcome these limitations, various solutions have been proposed and partially realised. One of the most prominent examples is the "QCCD", the quantum charge-coupled device [18]. This proposal led to the development of a new generation of *segmented* ion traps, where the axial confining potential can be tailored to more complex configurations than just the harmonic potential of a standard linear Paul trap.

The basic principles of these solutions are either the increase of the number of qubits within one trap [17] or building networks where small processors (traps) are interconnected and the quantum information is transported from one to another. In this section some of the proposals are introduced.

3.2.1 Many-qubit systems and new types of quantum gates

As noted before, segmented ion traps allow a much more flexible tailoring of the axial potential shape. This enables the storage of ions in long chains where the inter-ion distance is constant (see figure 3.7). In such a configuration the coupling between the ions can be accomplished by using the radial motional modes [17, 67]. Additionally, these long ion

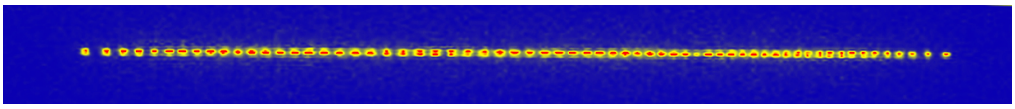

Figure 3.7: *A chain of 64 ions trapped with almost equal spacing. This was achieved using a linear trap with five segments [68].*

strings may be combined with ultra fast gates [69, 70]. There ultra short laserpulses, much shorter than the lifetime of an excited state pertaining to a dipole transition, are used for coherent population transfer. A geometric phase pick-up for entangling-gate operations can be mediated by the momentum kick when a photon is absorbed. Due to the short gate time in comparison to the trap oscillation period the excitation of the motional state occurs only locally [66] in the ion chain as the shared motion of the ions is too slow to spread the information. Decoherence due to unwanted spectator modes is thus suppressed.

Another route to enable quantum computation in large strings of ions may be achieved with gates that do not rely on atom-light interactions. This would abrogate the necessity of ultra-stable laser sources (in frequency and intensity) which are one of the main limiting factors of scalability due to their required well defined laser-ion interactions. It has been shown that ion strings, placed in a strong magnetic gradient, may offer a coupling between the qubit and external degrees of freedom [71]. This coupling would not rely on optical wavelengths and thus enable the coupling of the internal states of distant ions [72].

3.2.2 Transporting quantum information

The experiments and proposals mentioned above focus on increasing the number of possible qubits within one quantum register. An alternative route rendering trapped-ion quantum computation scalable is proposed by developing techniques to interconnect small quantum registers. Therefore, ways to coherently transport the quantum information from one ion trap to another are investigated.

Photons as carriers

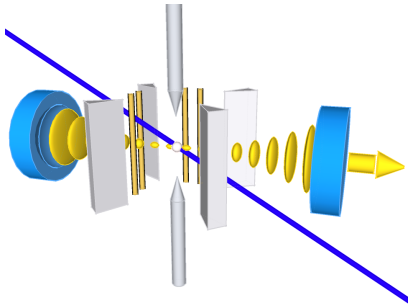

Figure 3.8: *A trapped ion coupled to an optical cavity. This system can be used to realise quantum information transfer between static qubits (ions) and flying qubits (photons). The picture is courtesy of Bernardo Cassabone.*

Photons are one possible realisation of quantum information carriers [73]. This proposed scheme would require a mapping of the quantum information between the atomic state and a single photon. Ideally this could be done deterministically. Cavity QED experiments are a promising realisation to achieve the required coupling between atoms and single photons [74–76]. A technically more simple solution than the deterministic coupling can be achieved by a probabilistic scheme. Here, the demand for a unit-efficiency conversion between qubits is dropped. Interfering two photons emitted by ions in remote locations is then used to herald ion-ion entanglement [77, 78]. Creating a large network with many entangled ions could then be used for further processing within the respective processors without the need for further transport of quantum information as a "one way quantum computer" [79]. The cost of the simplicity is the overall rate at which entanglement occurs and can be measured. This currently stands at typically 40 Hz [80].

Transfer with particle transport

Another way to transport quantum information from one processing unit to another is by directly shuttling an ion or ions from one trapping site to another within a multiplexed segmented trap architecture [18]. This scheme requires a very precise and stable control of the trapping voltages. For shuttling operations, this control must then be varied rapidly (on the order of the trapping frequencies which are up to a few MHz) while maintaining their base stability. To date a variety of experiments with numerous trap designs have

successfully demonstrated splitting [81], shuttling and reordering of ions within a linear trap [82] and through T- [24] or Y- [27] or X-junctions [25]. One aspect that needs to be considered is the time needed for such a shuttling routine, as it has to be performed in addition to the gate operations and within the coherence time of the system. As the coherence time drops with an increasing number of qubits, e.g. for a GHZ state the coherence time scales with $1/N^2$ [56], the shuttling operations should be expected to be as fast as gate operations and certainly shorter than 100 ms. This requires fast voltage drives for the electrodes and prohibits the use of low-pass filters to reduce electrical noise on the electrodes. This may not be desirable, as good filtering of electrical noise can reduce unwanted heating of the ions as demonstrated in chapter 6.1.2.

Direct transfer in coupled systems

A third way to distribute quantum information within a network of small processors is one of the topics in this thesis. Here, ion strings are coupled directly due to the dipole-dipole interaction induced by the oscillating charges (the ions themselves) within each trap. Therefore the ions can be described as resonantly coupled oscillators. This coupling acts as a channel to transfer the quantum information from one trapping site to another without the need of fast shuttling of the ions within the multiplexed trap [83, 84]. As with the information transfer by shuttling, speed of the information exchange between two coupled systems needs to be fast compared to the decrease of coherence. The interaction speed directly depends on the coupling strength of the dipole-dipole interaction. In this thesis, the coupling of the motional state of two ion traps has been implemented on a quantum mechanical level and the coupling strength has been increased using multiple ions for the first time as described in chapter 6.

Chapter 4

Experimental setup

This chapter introduces the experimental setups that have been built and used during this thesis. Section 4.1 describes the general infrastructure that is needed to operate the ion trap experiments, such as laser sources and computer controls. In section 4.2 and section 4.3, the two ion traps used are introduced: The first one is the planar trap "Bastille", courtesy of I.L. Chuang at MIT, Boston. The second trap, "Micreon", is a two-layer gold on alumina sandwich-type trap which was built in a consortium under the European project STREP-Mircotrap.

4.1 General setup

In an ion-trap experiment, the ion is held in a trap which, in turn, is mounted in a vacuum system. The ion is illuminated by various laser lights for the purpose of ion creation (photoionising atoms) and state preparation, manipulation and readout. The ion can then be imaged by collecting scattered light. The trap and laser systems require a high degree of control which is achieved by various computer-controlled electronic systems. The experiments presented in this thesis have been carried out in two different trap systems. However, the general infrastructure remained the same. This section gives an overview of the infrastructure used to operate the two traps.

4.1.1 Laser systems and detection

This section describes the various laser systems, that are required for the trapped-ion experiments of this work. These include the photoionisation of atomic calcium (422 and 375 nm), as well as cooling and detection (397 nm), repumping (854 and 866 nm) and state preparation (729 nm) of the ions. A level scheme of $^{40}Ca^{+}$ is shown in figure 3.1. In the end, the two methods how the scattered light of the ion is detected are described.

Photoionisation of calcium is achieved in a two-step process with lasers at wavelengths of 422 nm (resonant with the atomic $4s^1S_0$ to $4p^1P_1$ transition) and 375 nm (P_1 to the continuum). The two laser diodes (both Toptica DL100) are grating stabilised and the

wavelength of the 422 nm laser is monitored by a WS-7 wave meter (High Finesse). The two laser beams are overlapped on a polarising beam splitter (PBS) and coupled via a single-mode fibre to the experiments.

Cooling and detection of calcium ions is realised on the $S_{1/2} - P_{1/2}$ dipole transition at a wavelength of 397 nm [39]. Additionally 866 nm is needed to pump back possible populations from the metastable $D_{3/2}$ state, into which the ion can decay from the excited $P_{1/2}$ state, as described in section 3.1.1. 397 nm light is generated by frequency doubling of a titanium sapphire (Ti:Sa) laser at 794 nm. The Ti:Sa laser (Coherent 899 ring laser system) is pumped by a diode-pumped solid-state (DPSS) laser system (Coherent Verdi V10, 532 nm) The 794 nm light is stabilized to an external reference cavity using the Pound-Drever-Hall method achieving a linewidth of about 300 kHz [85]. To be able to tune the resonance frequency, one of the mirrors of the reference cavity is held by two piezoelectric transducer (PZT) rings. A resonator with a lithium triborate (LBO) crystal is used to double the frequency of the light at 794 nm. An output power of up to 100 mW at 397 nm is generated. This light is distributed with polarising beam splitters (PBS) and half-wave plates into three paths to be used at three independent calcium experiments. Fine-tuning of the frequency and intensity by each individual experiment is done with the first order of an acusto optical modulator (AOM, Brimrose, QZF-80-20-397) in double-pass configuration. Frequency control (around 80 MHz) and power control (up to 2 W) is provided by in-house electronics including a voltage controlled oscillator (VCO, Minicircuits POS100) and an rf-amplifier (Motorola, MHW9267). The light is then coupled via a polarisation maintaining single-mode fibre to the experimental table. Another AOM in single-pass configuration at 80 MHz switches the light on or off, controlled with a TTL signal. This AOM also allows for further intensity control. The reference cavity stabilising the Ti:Sa laser is detuned from $^{40}Ca^{+}$ resonance by 240 MHz so that the light passing the two AOMs is then in resonance with the calcium ions. A mechanical shutter in the zeroth order beam path of the double-pass AOM allows the far red-detuned light (160 MHz) to be switched on. This light is needed for cooling of hot ions, e.g. while loading the trap.

The laser-light at 866 nm is produced with a diode-laser system (Toptica, DL100), that is also stabilised to an external reference cavity with the Pound-Drever-Hall method. Distribution to different experiments is achieved by dividing the light with polarising beam splitters and half-wave plates. A double-pass AOM setup at around 200 MHz enables independent intensity and frequency control for the experiments. The light is sent to the experiment with a single mode fibre. In order to have just one beam path carrying all wavelengths needed for loading, the 397 nm light is overlapped with the photoionisation beams with a band-pass filter (Semrock FF01-395/11-25) used as a dichroic mirror. This beam is then further overlapped with the 866 nm light with another band-pass filter (Semrock FF01-839/270-25).

The quantum-logic laser is resonant with the $S_{1/2} - D_{5/2}$ quadrupole transition at 729 nm. It is used for coherent manipulations of the quantum state of the ions. The laser light is generated with an optically pumped titanium-sapphire laser (Coherent, 899 ring

laser). The setup was built by Michael Chwalla and a detailed description is given in his thesis [86]. The laser is stabilised to an external high finesse cavity ($\mathcal{F} = 479500(1600)$) with the Pound-Drever-Hall method to achieve a sub Hertz linewidth on a time scale of 1 s. The stability on longer timescales is limited by the thermal drift and the aging of the cavity material (ULE), which has a thermal expansion coefficient of below $10^{-8}\mathrm{K}^{-1}$. Since the maximum output power of up to 500 mW is only sufficient to service one experiment at a time, 10 mW of the light is picked off the Ti:Sa laser light. The light is then amplified using a tapered amplifier diode laser system (Toptica TA-100) to generate up to 400 mW of light. A polarisation maintaining single single mode fibre cleans the transverse mode to a TEM_{00} mode. The light is then passed through an AOM at 80 MHz for intensity stabilisation and is finally coupled into another ten metre long polarisation maintaining fibre sending the light to the experimental apparatus. Amplitude and frequency control of the light is done with an AOM at 270 MHz in double-pass configuration. The radio-frequency pulses for this AOM are generated by the digital synthesizer built in the pulse sequencer box (section 4.1.2) to achieve phase coherent laser pulses. The light is then split into two paths and further AOMs, again at 80 MHz, are used to switch the light between the different optical paths and directions towards the ions.

Repumping light is necessary, as described in section 4.3.4, to pump population in the metastable $D_{5/2}$ states after the detection of the quantum state back to the $P_{3/2}$ state. From here it decays rapidly back to the $S_{1/2}$ ground state, from which the experiment cycle is begun again. The laser-light at 854 nm is produced with a diode-laser system (Toptica, DL100) and is also stabilised to an external reference cavity with the Pound-Drever-Hall method. The optical setup is similar to the one of the 866 nm light including the double-pass AOM setup at around 200 MHz for independent intensity and frequency control. Both wavelengths (866 nm and 854 nm) are overlapped on a PBS and coupled together via a single-mode fibre to the experimental table.

Detection of the ions' fluorescence. Two devices are used to detect the light scattered by the ions: a photo-multiplier tube (PMT)[1] and an electron multiplied charged coupled device (EM-CCD) camera[2]. The PMT offers a fast detection of all ions at the same time, while the camera is slower than the PMT but allows the resolution of the individual ions. In order to minimise stray light on the detectors, both devices have narrow-band filters[3] attached.

4.1.2 Experimental control

Control over the experiment, switching laser light on/off, changing frequencies/powers, is described in detail in [36] and summarised here. The intensity, frequency and phase of the laser light can be controlled with AOMs that transfer these properties from a radio-frequency signal to the light field. The hardware to generate the appropriate RF signals

[1] ET enterprises, electron tube 9111B
[2] Andor, iXon DV885 JCS-VP
[3] Semrock, FF01-395/11-25

consists of a computer that includes digital and analog input/output cards (National Instruments, NI-PCI6733 / PCI6703) connected via TCP/IP with a pulse sequencer box (PBox) developed by Paul Pham and further adapted to the needs of the Innsbruck calcium experiments by Philipp Schindler [87]. The user interface is given by a Labview programme, "QFP 2.0", written by Timo Körber.

The pulse sequencer box

The PBox allows the generation of fast sequences of amplitude-, frequency- and phase-controlled RF pulses. The central unit is a field-programmable gate array (FPGA) processor that controls a direct digital synthesizer (DDS) for RF generation. Amplitude control is achieved with a digital analog converter (DAC) and a variable-gain amplifier implemented into the box. Additionally, the unit is equipped with 8 digital input and 16 digital output boards to receive and send TTL signals (on an update rate of 1 per 10 ns) to other hardware in the experiment such as AOM drivers for switching of laser lights.

Additional hardware

Some signals (analog or digital) are constant over the course of a sequence that is controlled by the pulse sequencer. These are generated with analog and digital input/output cards (National instruments, NI-PCI6733 and PCI6703) or a high voltage-supply (ISEG, EHS-8020x_405). Digital signal generators (Marconi Instruments, 2022E and Rohde & Schwarz, SMB01) are used as RF drives for the ion traps. A fast digital input counter (included in the NI-PCI6733) is used to count the photons detected by the PMT.

Software control

All the hardware mentioned above is controlled by the user using the QFP 2.0 programme, written in Labview. This is the graphical user interface that translates user commands into hardware code. The connection to the pulse sequencer box is achieved by an additional server programme written in Python. The sequences are sent by QFP via TCP/IP protocol to this server that translates the human-readable sequence code into machine code and transmits it to the PBox via a TCP/IP network connection. The analog and digital input/output cards are directly accessed by QFP, where two digital channels are used as hardware triggers to synchronize the software with the pulse sequencer box. Additionally, a GPIB-bus to control the signal generator and CAN-bus support for controlling the ISEG high-voltage supply are also implemented in QFP.

Camera control

The EMCCD camera is connected to a second, independent computer via the proprietary Andor bus. The original software (Andor Solis) is used to configure and readout the camera. For sequenced experiments, the camera can be triggered with a TTL signal from one of the digital outputs of the pulse sequencer box. For future experiments a programme, written in Labview using the proprietary Andor drivers library, will be able to communicate

with the experimental software QFP via a network connection. This programme has not yet been implemented into the experiment, since the following experiments did not require a single-qubit readout.

4.2 Surface ion-trap setup

The following section describes the experimental setup and the surface ion trap in which the two field-probing experiments described in chapter 5 have been carried out.

4.2.1 The "Bastille" trap

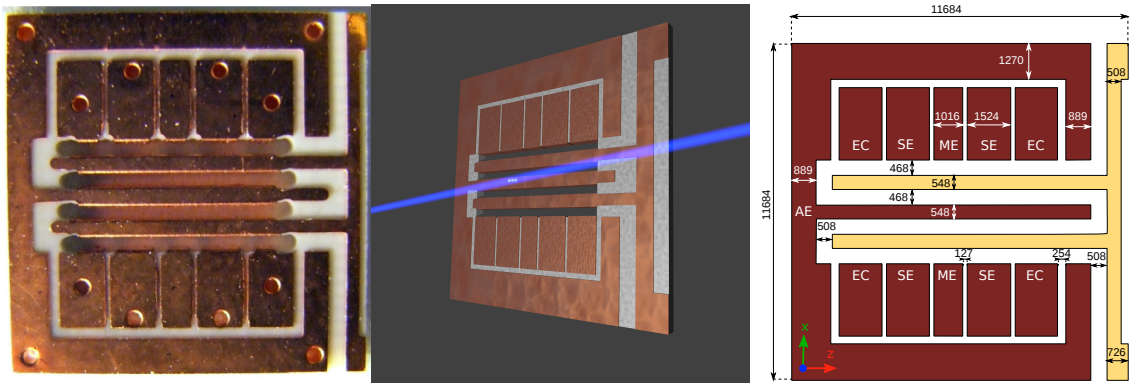

(a) (b) (c)

Figure 4.1: *The surface trap Bastille. (a) A photograph of the unbonded trap. (b) Schematic drawing of the trap. The laser beams pass the trap about* 800 μm *above the surface and parallel to it. The beam is at an angle of about* 5° *to the axial direction to achieve cooling in the radial direction. (c) Schematic drawing of the trap electrodes indicating the electrode group names ('EC' - endcap electrodes, 'SE' - steering electrodes, 'ME' - middle electrodes, 'AE' - axial electrode). All four steering electrodes are individually connected to separate channels, to allow for balancing the voltages and thus set the ions' starting positions. The dimensions of the trap are given in* μm.

The trap used for the experiments in section 5.2 and 5.3 is provided courtesy of I.L. Chuang, MIT Boston. A picture and a schematic view of the macroscopic, five wire surface-trap is shown in figure 4.1a. The electrodes are made of copper on a UHV compatible PCB material (Rogers Corporation, 4350-B). A detailed overview of the trap geometry and operational parameters is given elsewhere [28, 82, 88] and summarised here. The electrode dimensions are in the millimetre range (see figure 4.1a). The ions are trapped $\sim 820\,\mu$m above the axial electrode. The radio-frequency voltage for trapping has a frequency of $\sim 10\,$MHz and an amplitude of $U_{\mathrm{rf}} = 200 - 400\,$V. The necessary input power of 0.5 to 2.5 W is produced with a signal generator (Marconi Instruments, 2022E) and an amplifier (Minicircuits ZHL-1-5W). A helical resonator [15, 89] is used to transform the power to high voltages at low currents. The DC voltages are delivered by a computer-controlled

digital-analog conversion (DAC) card (National Instruments, NIPCI6733). For the endcap and middle electrodes [82] the voltage is amplified by a factor of ~ 14.

4.2.2 Vacuum apparatus

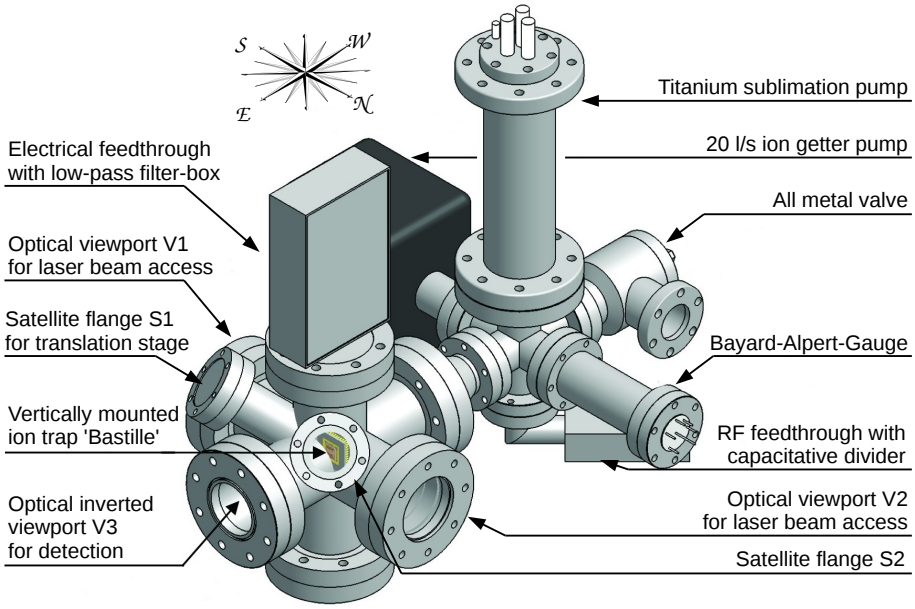

Figure 4.2: *A schematic of the vacuum vessel that holds the ion trap Bastille, where ions are used as electric field probes. The trap is mounted vertically in the center of a 6-way-cross. The cooling and photoionisation lasers are sent through the viewports V1 and V2 along the North-South axis. A lens system for detection inside the inverted viewport (V3) is held approximately* 6 cm *away from the trap surface. A translation stage holding a glass plate (not shown) was attached to the satellite flange S1 during the experiments described in section 5.3*

The trap is mounted in a vacuum vessel made of stainless steel, which is depicted in figure 4.2. The vessel has two sections. One is a pumping section with all UHV-pumps (20 l/s Starcell ion-getter pump and Ti-sublimation filaments), and an all-metal valve. With this valve, additional pumps for evacuation during bake out can be attached. Furthermore, a Bayard-Alpert-Gauge to determine the pressure is attached. The other section contains the trap itself. The trap is mounted vertically, facing east, in the vertex of a CF63 6-way-cross that has additional CF40 flanges in two of the space diagonals (Satellite flanges S1 and S2). The pumping section of the chamber is attached on the western flange of the 6-way-cross. The northern and southern flanges are closed with fused silica glass viewports for optical laser access (fig. 4.2 V1 and V2). The eastern flange holds an inverted viewport that sits close (~ 4.5 cm) to the trap surface. The inverted viewport allows the placement of a custom made lens (focal length: 67 mm, $NA = 0.28$, Silloptics Germany) close,

$\sim$ 6 cm, to the trapped ions for a high photon collection efficiency. With this lens the ions are imaged onto the EMCCD camera achieving a resolution of 2 μm per pixel. An electrical feed-through with Sub-D connector is placed on the top flange to connect the DC electrodes of the trap with the supply-voltage. To minimise radio-frequency pickup, low-pass filters with a cut-off frequency of 1kHz are used, mounted in an aluminum box for shielding. The radio frequency needed for the trapping potential is connected to an electrical feed-through mounted on the bottom flange of the pump section. A capacitive divider with an approximate ratio of 1:100 is used to yield information about the relative amplitude of the RF drive.

The satellite flange S1 holds a magnetically-coupled mechanical feed-through (not shown in figure 4.2). With this it is possible to bring samples, e.g. a glass window or fibre tip, close to the trap to study their effect on the ions. The mechanical feed-through has a travel range of 25 cm. The samples can thus be completely withdrawn from the trap, such that they do not influence the ions. With this modification charging of a dielectric glass plate could be demonstrated, as described in chapter 5.3.3.

4.2.3 Segmented-electrode control

The voltage supplies for the Bastille trap electrodes are supplied by the NI-PCI6733 analog output board, the counter of which is also used as the PMT digital input. Multiplexing the channels, as described in [88], allows the control of all eleven electrodes with one 8-channel board. Two channels are amplified with a high voltage amplifier to enable voltages of up to 119 V. The computer-control software has been expanded to allow ion shuttling within a sequence [82]. To minimise the computation power required, the voltage ramps were not calculated with the QFP software, instead a modular expansion to the Pbox server software using the proprietary drivers in C-code (National Instruments, NIDAQmx ANSI-C) was written, such that the server program controls the analog outputs of the board. A graphical user interface was implemented into the QFP software.

4.3 Two-layer trap system

The following section describes the experimental setup and the two-layer ion trap "Micreon". In this trap the experiments about quantum information transfer described in chapter 6 have been carried out.

4.3.1 The "Micreon" trap

The trap used in the experiments presented in chapter 6 has been built within a European collaboration under the STREP-Microtrap project. The organisation of the manufacturing process was lead by the group of Ferdinand Schmitt-Kaler in Ulm (now in Mainz). Detailed information on the production process is given in the Thesis of Stephan Schulz [90] and an overview is given here. It is a sandwiched two-layer trap (section 2.2.1). The gold electrodes were evaporated and galvanically grown on alumina wafers and the structuring and insulation cutting was done with laser cutting. The two gold coated wafers

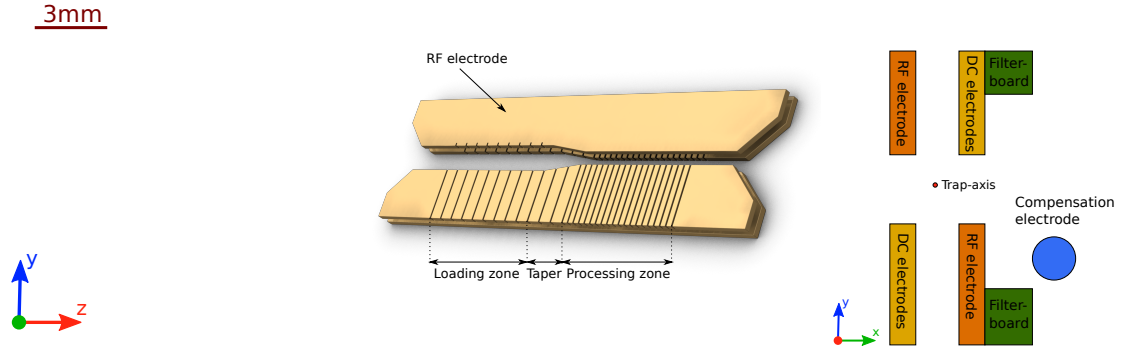

Figure 4.3: *(a) A picture of the two-layer gold on alumina "Micreon" trap. (b) Schematic of the two trapping zones; a wider zone with an aperture of* 500 μm*, called the loading zone for historic reasons, and a zone with smaller aperture of* 125 μm *called the processing zone. (c) A schematic of the cross section of the trap indicating the RF and DC electrodes as well as the filter board holding the trap. An additional compensation electrode parallel to the trap axis was attached to the backside of the filter board to enable micromotion compensation in a second radial direction.*

are separated by a 125 μm thick alumina spacer. A picture and schematic drawings of the trap are shown in figure 4.3. The trap has two zones with different ion-electrode spacings: the so-called "loading zone" (on the left) and "processing zone" (on the right). In the loading zone the aperture is 500 μm wide and the electrode width is 250 μm. The dimensions for the processing zone are 125 μm for the aperture and 100 μm as the electrode width. A taper section that consists of three 250 μm wide electrodes connects the two zones where the aperture decreases linearly from 500 μm to 125 μm. All the experiments of chapter 6 have been carried out in the loading zone as the heating rate is expected to be lower due to the larger ion-electrode distance. A 125 μm thick spacer separates the two substrates with the gold plated electrode structures. The ion-electrode separation is thus 258 μm. The 30 MHz radio-frequency voltage is generated by a digital synthesizer[4]. The signal is amplified with an RF amplifier[5] and the power is transformed to high voltage with a helical resonator (unloaded frequency of 99 MHz). With this setup, voltages of up to $\sim$ 400 V amplitude (0 - peak) can be achieved. Low-pass filters inside and outside of vacuum reduce RF and noise pick-up on the electrodes. A photograph of the in-vacuum filter board with the attached trap is shown in figure 4.4b. The in-vacuum RC-filters with resistance $R = 2.8\,\mathrm{k\Omega}$ and capacitance $C = 55\,\mathrm{pF}$ have a cut-off frequency of $f = 1\,\mathrm{MHz}$ and are made with UHV compatible thick-film at the University of Siegen. The alumina substrate of this filter board is also the carrier holding the trap itself. Using only the trap electrodes themselves there is only the possibility to compensate micromotion in one radial direction by applying a bias voltage on two opposing DC electrodes. There are no

[4] Rhode&Schwartz, SMB-01
[5] Minicircuits, ZHL-1-5W

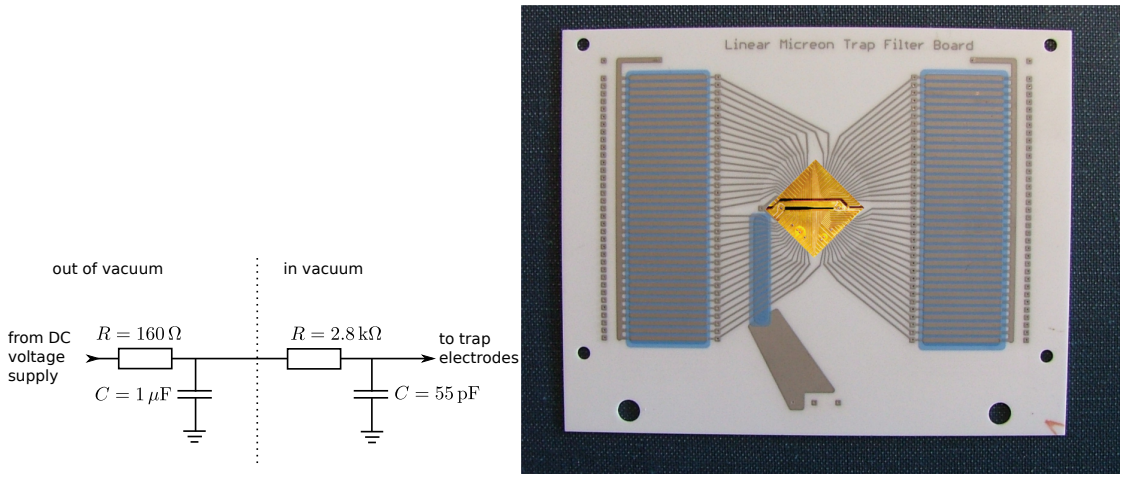

(a) **(b)**

Figure 4.4: *(a) The electric circuit for both filters, the one inside vacuum and the other attached on the outside to the electrical feed-through of the vacuum vessel. (b) A picture of the alumina filter board that holds the Micreon trap. It is made with thick-film technology at the University of Siegen. The capacitors of the RC-filters consist of two conducting plates separated by an insulating (blue) material*[6]*. The resistors are on the backside of the board.*

micromotion compensation electrodes on the RF electrode sides. To allow micromotion compensation in a second direction an additional gold-plated steel rod with a diameter of 2 mm has been attached to the backside of the trap-holding filter board (see figure 4.3c).

4.3.2 Vacuum apparatus

The stainless-steel vacuum chamber containing the ion trap is shown in figure 4.5. The trap is mounted vertically in the center of a CF200 octagon with eight CF63 flanges surrounding it. To one of the flanges the pumping section is attached, including a 20 l/s ion getter pump[7], a titanium sublimation pump[8] and a Bayard-Alpert UHV gauge[9]. A gate valve between the main chamber and the pumping section allows the pumps to always be kept under vacuum, even if the chamber needs to be opened for maintenance or repair. On the opposite side of the main section an all-metal valve is mounted, to attach a pump stand with a turbo molecular pump during bake out. For optical access four viewports and two inverted viewports are attached to the remaining six CF63 flanges. The inverted viewports allow the placement of lens systems with a focal length of $\sim$ 5 cm close to ion trap. The bottom of the vacuum chamber is formed by a CF200 blank flange. The flange on top of the chamber has additional smaller flanges for electrical feed-throughs:

[6] DuPont, 5704
[7] Varian, Starcell
[8] Varian, TSP
[9] Varian, UHV-24p

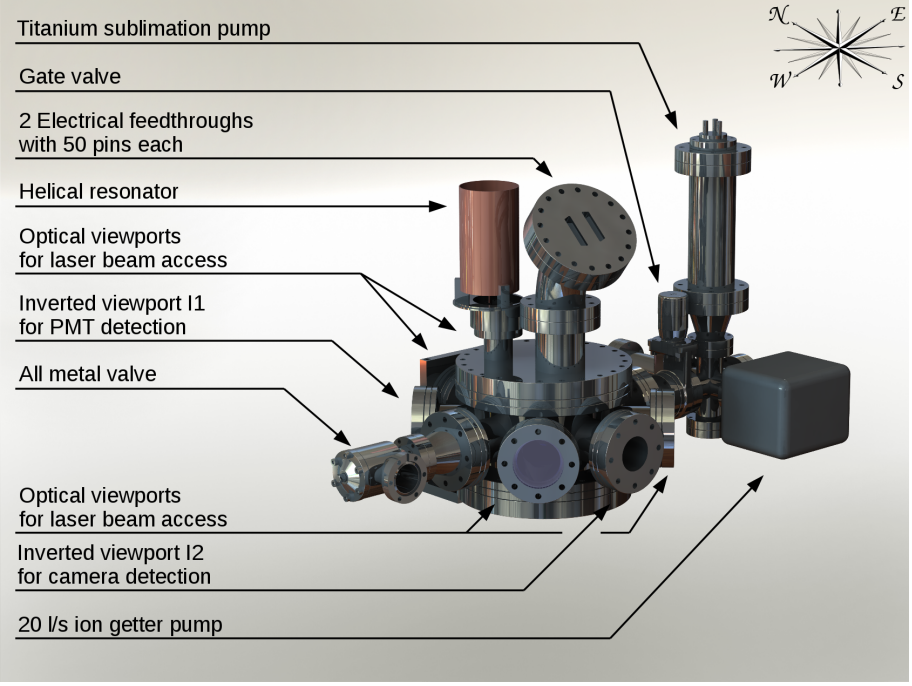

Figure 4.5: *A schematic of the vacuum vessel that holds the ion trap "Micreon" used for the experiments described in chapter 6. The vessel consists of two sections: a pump section (eastern part) and the experimental section (western part). The two sections are connected with a gate valve to keep the pump section under vacuum, even if the chamber has to be opened. The experimental section is a CF200 octagon in which the trap is mounted vertically with the trap axis tilted by* 15° *counter clockwise from the east-west axis. On top flange of this section the helical resonator for the RF supply and the electrical feed-throughs for the electrodes' DC voltages are attached. Six optical viewports (including two inverted viewports) allow three optical paths to be used.*

one high-voltage two-pin connector for the RF drive (CF40), one eight pin connector for the calcium oven current (CF40) and one flange with two D-Sub 50 connectors for the DC segment voltages (CF100). The trap mounted onto the ceramic filter board is also attached to this top flange, as is the atomic calcium oven. It is therefore possible to mount the trap and the electrical contacts on one flange, adjust the beam direction of the atomic oven and then attach the whole trap system onto the vacuum chamber in one piece. After the assembly, the vessel was baked at a temperature of 190°C for 2 weeks under vacuum with a pump stand attached to it via the all-metal valve. As a result a final pressure of $3 \cdot 10^{-11}$ mBar was achieved.

4.3.3 Electrode voltage control

The DC voltages for the segmented electrodes were initially generated with a 10 V precision reference (Analog devices, REF01) powered by 12 V lead batteries. The voltage control is done by voltage dividers built with 10-turn precision potentiometers. In the

later experiments the DC voltages were generated with the programmable eight channel high-voltage supply (ISEG Spezialelektronik, EHS-8020x_405) mentioned above.

4.3.4 Experimental sequence

The quantum-information experiments, described in chapter 6, are performed with a sequence of different laser pulses and consist of three main parts: initialization of the ion qubit(s), quantum operations and then state detection. Figure 4.6 shows a schematic of the experimental procedure with the respective lasers for each step when working with $^{40}Ca^{+}$ qubits. First, Doppler cooling is applied on the dipole $S_{1/2} - P_{1/2}$ transition including a repumping laser from $|D\rangle$ back to the $|P\rangle$ state ($\sim 2.5\,\mathrm{ms}$). Thereafter optical puming and sideband cooling on the quadrupole transition ($S_{1/2} - D_{5/2}$) are alternated to achieve a well defined state $\left|S, m_j = -\frac{1}{2}, n = 0\right\rangle$ ($\sim 10\,\mathrm{ms}$). At this stage the ions are prepared in the initial state. The quantum state manipulation and operations are then done by various pulses on the $S_{1/2} - D_{5/2}$ transition to generate the desired unitary operations on the ions (up to a few $100\,\mu\mathrm{s}$). The state-detection process ($\sim 2\,\mathrm{ms}$) projects the ions either into the $|S\rangle$ (fluorescing) or $|D\rangle$ (dark) state. Finally the repumping light at 854 nm brings the ions' populations back into the ground state ($\sim 500\,\mu\mathrm{s}$). This sequence is repeatedly performed unchanged a certain number of times to measure the statistical state probabilities.

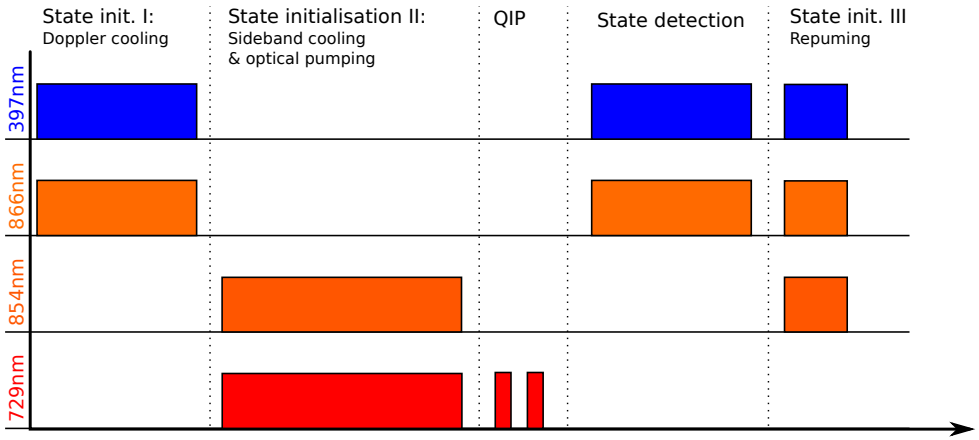

Figure 4.6: *The experimental sequence as the lasers are switched for the individual steps to initialise the qubit(s), perform the quantum operations and finally read out the state of the qubit(s). During the sideband cooling and optical pumping processes, the frequency of the laser is alternated such that it is once resonant with the red sideband transition between the* $\left|\mathrm{S}, m_j = -\frac{1}{2}\right\rangle$ *state and the the excited* $\left|\mathrm{D}, m_j = -\frac{5}{2}\right\rangle$ *state for sideband cooling and then it is resonant with the carrier transition from* $\left|\mathrm{S}, m_j = \frac{1}{2}\right\rangle$ *to* $\left|\mathrm{D}, m_j = -\frac{3}{2}\right\rangle$ *for optical pumping to collect the population in the* $\left|\mathrm{S}, m_j = -\frac{1}{2}\right\rangle$ *state.*

Chapter 5

Trapped ions as field probes

A trapped, charged atom is sensitive to a variety of physical quantities and their effects. Thus there are many possible ways to use trapped ions not only as qubits in a quantum computer, but also as a tool to measure these quantities. The internal electronic states of the atom, accessible with electromagnetic waves at optical or radio-frequencies, can thus be used as clocks or, if magnetic effects are taken into account, as probes for magnetic fields. Moreover, the ion will always stay in the minimum of the electric potential of the trap. Therefore, any additional electric potential which modifies the trapping potential will be measurable with the ion as a shift of either the motional frequency or the ions' position or both.

Recent developments of ion traps focus on the miniaturisation and segmentation of the trap structures, where scalable quantum computation may be achieved (as described in chapter 2). These technological implementations to ion traps cause different challenges for designing, building and operation of such devices. Since fabrication processes underlie different imperfections, the final trapping potential can vary from the originally simulated one. Additionally the true effect of each electrode on the trapping potential is important to know, when shuttling ions around within the trap.

In the following chapter two examples of using the ions' positions as probes for electric potentials are shown. In the first experiment, a long string of a few tens of ions is trapped in a linear trap, and the axial trapping potential is measured with their equilibrium positions. In the second experiment, charges are created by illuminating surfaces in the vicinity of a few trapped ions. These charges create an electric potential in addition to the trap potential and causes the ions to shift their positions. By observing the ions' centre of mass position as it changes over time, a detection sensitivity of 40 elementary charges per $\sqrt{\text{Hz}}$ was achieved. These two sections will follow a short motivation including a theoretical overview on how the potential can be calculated with the ions' positions and a brief introduction to the experimental setup. The major results reportet in this chapter have been published in [68] and [28].

5.1 Probing electric potentials and fields with ions

This section shows the two methods that are used in this chapter to calculate an electric potential. Both methods use a CCD camera picture as measured data, where the pixel size is calibrated to real distances at the focal plane. A picture of a long string of ions is the basis for the first method, where the electric potential is calculated from inter-ion distances. In the second method, series of pictures are taken to measure the change of the ions' positions. Combined with the trap frequency, this movement is used to calculate the time-dependent electric field that causes the ions' movement.

5.1.1 Calculation of the axial trapping potential with long ion chains

The axial trapping potential (see 5.2) of an ion trap can be directly measured using long ion chains as the positions of the ions are such that the total potential energy is minimised. In Paul traps ions are generally confined in three dimensions. In the following, only one (the axial) dimension is considered, which is reasonable if the radial trapping frequencies are much bigger than the axial: $\omega_{r1}, \omega_{r2} \gg \omega_{ax}$. Consider a string of N ions trapped under this condition. At equilibrium, the sum of all forces acting on each ion i is zero.

$$F^{(i)}_{\text{total}} = 0. \tag{5.1}$$

The total force $F^{(i)}_{\text{total}}$ acting on one ion, i, at position z_i consists of the Coulomb repulsion from all other ions, j, and the force due to the external confining potential $F_{\text{ext}}(z_i)$

$$F^{(i)}_{\text{total}} = F^{(i)}_{\text{ion}} + F_{\text{ext}}(z_i) = 0 \tag{5.2}$$

where

$$F^{(i)}_{\text{ion}} = \frac{e^2}{4\pi\epsilon_0} \sum_{j \neq i}^{N} \frac{|z_i - z_j|}{(z_i - z_j)^3}. \tag{5.3}$$

Since the total force $F^{(i)}_{\text{total}}$ is zero at equilibrium, $F_{\text{ext}}(z_i)$ is equal and opposite to $F^{(i)}_{\text{ion}}$, in other words $F_{\text{ext}}(z_i)$ can be calculated for all ion positions z_i. Interpolating between each ion position, a numerical integration gives the confining potential in 1D except for an unknown integration constant. In this way, when the ions' positions are known (taken from a CCD camera image), the confining axial potential can be retrieved.

With this method, not only can the applied confining potential be measured, but it is also possible to isolate the effects on the potential due to single electrodes. This can be done by applying small variations δV to the voltage $V_{\text{electrode}}$ on the electrode of interest, while keeping all other voltages unchanged. The resulting potential $\psi_{\text{modified}}(z)$ consists of the unmodified reference potential $\psi_{\text{ref}}(z)$ and the potential $\psi_{\text{electrode}}(z, \delta V)$ that is generated by the electrode with an applied voltage δV. Therefore, potential of the electrode of interest can be instantly calculated for the region where both potentials overlap:

$$\psi_{\text{electrode}}(z, \delta V) = \psi_{\text{modified}}(z) - \psi_{\text{ref}}(z) \tag{5.4}$$

Numerical errors may be reduced, by averaging over repeated measurements for different values of δV. Under the assumption that the radial trapping frequencies are much greater than the axial one, any movement of the ion string in the $x-$ and $y-$direction can be neglected and the potential change can be measured with the change of the ions' positions. This method could also be extended for higher dimensions, either by measuring the ion positions of two- or even three-dimensional ion crystals, or by measuring the change of the ion spacings due to an additional potential in all the directions of interest.

5.1.2 Probing electric fields or potentials with single ions

The second method of this chapter to map out an electric field over a wide range is to use a single ion or a string of a few ions in a harmonic trap. In a segmented ion trap, the trapping zone with the ions can be moved along the trapping axis while keeping the motional trapping frequencies constant. For small electric fields the effect on the ions can then be approximated by an additional linear potential. This causes the trapping minimum, and thereby the centre of mass of the ion string, to move by a distance Δz_{ion} along the trap axis, assuming that the radial frequencies are much higher than the axial one. Therefore the projection of the applied electric field onto the trapping axis can be calculated.

$$E_{\text{ax}} = \frac{\Delta z_{\text{ion}} e}{4\pi\varepsilon_0 \omega_{\text{ax}}} \tag{5.5}$$

If the applied electric field is changing over time, $E_{\text{ax}} = E_{\text{ax}}(t)$, the movement of the ions measured by a series of pictures can be used to obtain this time dependency.

5.2 Long ion chains to measure the electric potential

Three experiments are presented in this section. In each experiment a long string of tens of ions is used to measure the axial potential. This method is then used to probe the potential of the trap (5.2.1), the change of the axial potential during a shuttling routine (5.2.2) and the potential of a single trap electrode (5.2.3).

5.2.1 Probing a trap potential

An ion string of up to $\sim$ 30 ions is loaded with photoionisation into the trap. Typical motional trapping frequencies are ω_x, $\omega_y = 2\pi\times(250,\ 800)$ kHz for the radial modes. The axially confining potential is provided by voltages (-20 V $< V <$ 60 V) applied to the five pairs of DC segments. Its curvature is much smaller than that of the radial potential resulting in a frequency of $\sim$ 90 kHz. An accumulation of 10 pictures of the ions is taken to increase the signal to noise ratio. Since the individual ions simply have to be resolved on the CCD image, the cooling does not need to reach the Doppler limit. A Labview routine was written to measure the axial positions of each ion in the string: the intensities for each column of the accumulated picture are summed to retrieve an axial intensity profile (figure 5.1). Due to imaging errors (stray-light and aberration of the lenses used) a halo can be seen around the ions. This halo results in a slowly varying background in the

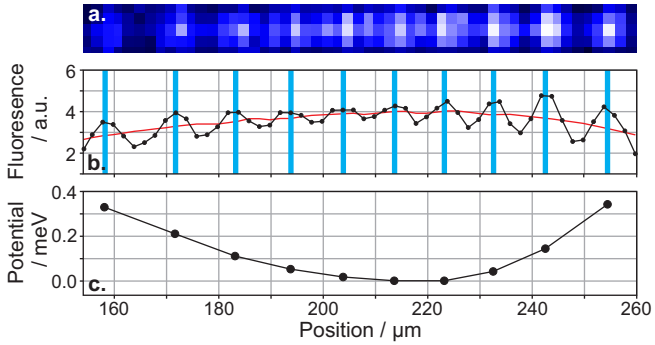

Figure 5.1: *Calculation of a 1D potential along the trapping axis [68]. (a) The ions are imaged with the EMCCD camera, typically with a 100 ms exposure time and a resolution of about 2 µm per pixel. (b) The counts for each column are summed (dots). To compensate for non-uniform illumination and imaging artifacts a slowly varying background (red line) is subtracted. The ion positions (blue lines) are then determined using a weighted fit. There are a number of more involved algorithms for identifying ion positions [91], though the simple method used here was sufficient to give a positional uncertainty of less than ±0.5 µm, or 0.25 pixels. (c) The axial potential is reconstructed by numerical integration of the forces calculated by equation 5.3. The offset of the potential has been arbitrarily chosen such that the minimum of the potential is zero.*

intensity profile which can be subtracted. With these positions the axial potential is then calculated following as described in section 5.1.1. The analysis of a typical set of data with the resulting axial potential is shown in Fig. 5.1.

5.2.2 Analysing a shuttling routine

Having evaluated a single potential it is straight forward to analyse a variation of this potential, e.g. for a shuttling process, provided the shuttling is adiabatic, i.e. slower than the trap frequency. By interrupting the shuttling process after short steps one can capture a series of images of the ion string. Fig. 5.2a shows such a series, each taken at a different step of the shuttling process, which is equivalent with different sets of electrode voltages. These images were used to calculate the potential seen by the ions as they were moved from left to right along the trap. Use of only one or a few ions would provide information about the position of the well minima. However, the presence of a large number of ions allows visualisation of a greater extent of the entire potential in an instant. During this measurement, due to the rather shallow confinement at axial trapping frequencies of up to ~ 100 kHz, ions were lost and had to be reloaded. However, this did not detrimentally affect the measurement. Figure 5.2b shows the reconstructed potential during the shuttling process.

The exact shape of the confining potential (of order mV) is due to small differences between large electrode voltages (of order V). Any imprecision in a computer simulation of the trap can give rise to qualitatively different predicted potentials. For example, for the scenario in Fig. 5.2c the simulation was qualitatively different (no shuttling was observed between the two separate wells). The direct measurement using ions is clearly a more

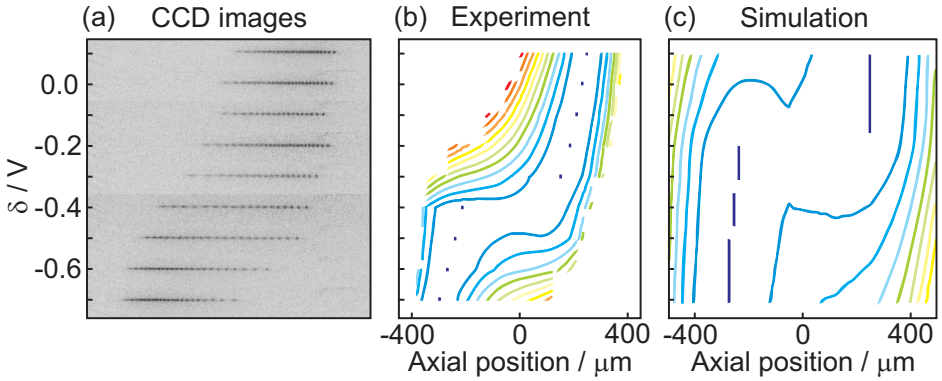

Figure 5.2: *Analysing a shuttling routine. The initial axial potential was created by applying* (V_{EC},V_{SE},V_{ME}) = (40.5, 4.5, 30.8) *V to the DC electrode segment groups. To move the ions along the trapping axis, the steering electrodes were used by increasing the voltage on the left hand pair and decreasing the voltage on the right hand pair of electrodes by equal amounts,* δ*. For each measurement the string consisted of 18 to 25 ions. (a) CCD images of the ion strings for different values of* δ*. (b) A contour plot of the measured potential as a function of* δ*. Equipotential lines are spaced by 0.4 meV. (c) Simulation data for similar voltages to those used in the experiment (within 1 V). This shows that the experimentally observed behaviour can be qualitatively reproduced in simulations.*

sensitive and accurate method.

5.2.3 Analysing the effect of single electrodes

Finally, as described in section 5.1.1 the effect of a single electrode can be ascertained. An example result is shown in Fig. 5.3. While keeping all other electrode voltages constant, measurements of the total trap potential were taken, with different voltages, $V_{ME} + \delta$, applied to the middle DC electrode pair. The effect of the *middle electrode* pair was calculated following section 5.1.1. The ion string was typically only 200 μm long. But, as the ion string was moved to different positions when changing V_{ME}, the potential due to the single electrode pair could be measured over an extended range ($\sim$1 mm). Furthermore, increasing the ion string's length by loading more ions would also increase the range of instantaneos measurement of the electrode's potential.

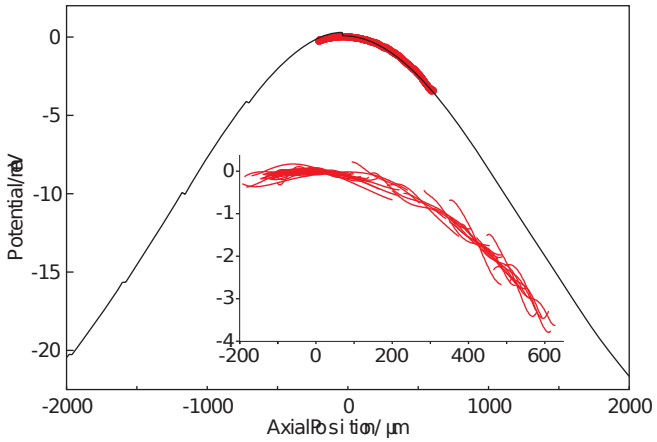

Figure 5.3: *Characterization of the potential due to a given feature. The thin solid line shows the potential along the trap axis due to a voltage $V_3 = 1$ V applied to the middle DC electrode, as calculated by boundary-element-method simulations. The discontinuities are an artifact of the 10 µm grid resolution of the simulation output. The bold line is the result from ion-string measurements. Potentials were measured for many different values of δ. The pairwise differences between these measurements were used to calculate the effect of the central electrode for the region in which the measurements overlapped (see section 5.1.1). Results of each pairwise measurement are shown in the insert. These results were then averaged to give the line in the main figure.*

5.3 Trapped-ion probing of light-induced charging effects on dielectrics

This section shows another way to use ions as electric-field probes. In these experiments the charging of surfaces under laser illumination is investigated by observing a shift in the position of a string of up to five ions (equation 5.5). Here, the extent of the charging-induced electric field along the trap axis is not mapped by moving ions in the trap to different positions, as described in section 5.1.2, instead the origin of the charging, i.e. the point of laser illumination, is moved. After a introduction on how the experiments are performed and analysed, two charging processes are studied. The first is charging on the copper surface of the trap itself, the second is charging on a glass window with an anti-reflective coating, that has been brought close to the ions with a distance of 1.2 mm.

5.3.1 Experimental method

A few additions were made to the generic apparatus described in section 4.2. These are illustrated in figure 5.4. Notably a small broadband mirror is additionally implemented into the detection path to shine the charging laser light onto the *axial electrode's* surface. The point of incidence, and therefore the point of charging, can thus be moved along the electrode, parallel to the trapping axis. The beams are focused to a diameter of below 100 µm and the beam pointing is calibrated by observing the position of the laser beam on the trap with the CCD camera. The experiments were performed with some of the

wavelengths, that are used for calcium ion trapping experiments: 375 nm, 397 nm, 422 nm and 729 nm. Also a mechanical feed-through was attached to the the satellite viewport S1 (figure 4.2) carrying a glass window. This window can be positioned above the trap, such that it is placed in the optical path of the charging laser and ions' fluorescence (figure 5.4).

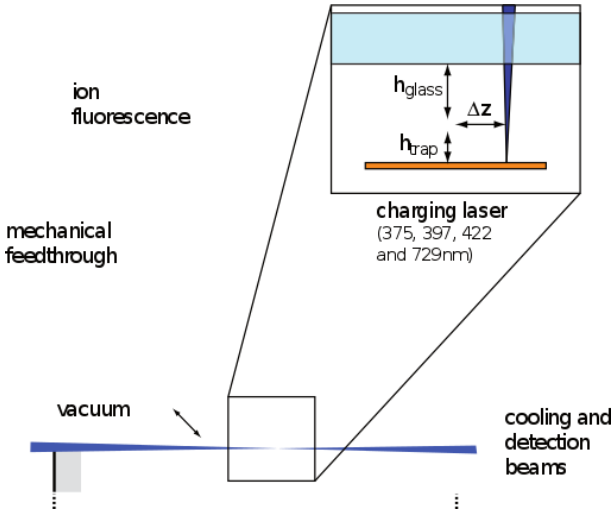

Figure 5.4: *Optical setup. A glass plate attached to a mechanical vacuum feed-through can be held at different distances (1 mm$\lesssim d \lesssim$10 cm) from the ion string (not to scale). Via a small mirror in the path of the fluorescence light, the glass plate and the central trap electrode can be illuminated with laser light of different wavelengths.*

A string of up to five $^{40}Ca^{+}$ ions is trapped at typical motional frequencies of $2\pi\times(790, 230, 90)$ kHz in the two radial and the axial directions. Cooling of the ion string is achieved in the same way as in the experiments described in section 5.2. A series of up to a few hundred CCD images is taken, each comprising 10 accumulations of 100 ms exposure, and 2 μm resolution to measure the positions of the ions. During the few minutes of recording of the images, the charging laser-light is switched on for a certain amount of time. The individual ion positions are fitted to each image using a method similar to that described in section 5.2.1 and thus the centre of mass position of the ions over time is measured. Due to the fitting of the ion positions and averaging over the individual positions the precision of the string's centre of mass position is increased beyond the resolution of the camera picture to 0.12 μm per ion per $\sqrt{\text{Hz}}$. The axial motional frequency of the ions gives information regarding the curvature of the confining potential. With equation 5.5 the change in electric field along the trapping axis can be calculated.

5.3.2 Charging of the trap surface

In the following experiments the above-mentioned glass plate is withdrawn, such that it has no influence on the ions and has no laser light incident on it. Figure 5.5 shows the axial position of the ion string over time as the illuminating laser ($\lambda = 375$ nm) beam is switched on for 40 s (grey-shaded area). The point where the laser hits the trap surface

is $\Delta z = 200\,\mu$m distant laterally from the initial position of the ions. While the laser is on, an attractive force acts on the ions as the substrate is illuminated, making them move at $\sim 1\,\mu$m/s towards the laser beam. This movement saturates on a timescale of ~ 1 min. Switching off the laser beam causes the ion string position to relax to close to its original value on a somewhat longer timescale.

The movement of the ions implies a negative charging of the copper trap surface. While the exact nature of the copper charging is not known, it is assumed that the surface is partially or completely covered by a thin insulating layer, probably an oxide [92]. One might expect that charges directly above the copper surface produce negligible fields, because image charges form directly beneath them and shield their effect. Charging of the copper electrode may be explained by the excitation of electrons onto insulating patches directly above the bulk material.

Together with the induced image charge this creates a small electric dipole. Such an

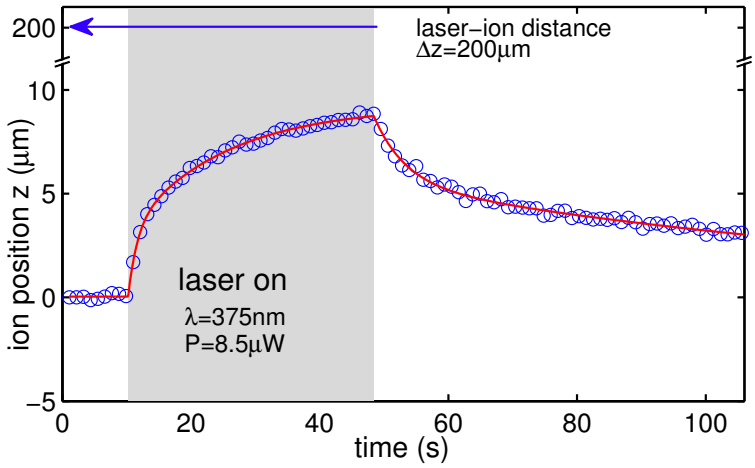

Figure 5.5: *Typical example of the axial positions of the ion string as the illuminating laser is switched on (grey-shaded area). The data was taken with* $8.5\,\mu$W *of* $\lambda = 375$ nm *light, focused on the trap at* $\Delta z = 200\,\mu$m *away from the ion on the axial electrode. The laser light impinging on the trap surface leads to charging. These charges cause ions to move towards the laser beam. After the laser is switched off, the ions relax slowly towards their original position, indicating an neutralisation of the charges produced. The solid lines are the exponential fits to the data.*

excitation represents a metastable state which may easily relax back to a neutral state. Analysing the data more quantitatively leads to the following model for the charging process of the trap surface. Under illumination with laser light local charges are produced with a wavelength-dependent production rate, P. The presence of existing charges creates a barrier inhibiting the creation of new charges. This may, to first order, be accounted for by considering a production rate $P = P_0(1 - \delta \cdot n_q)$, where n_q denotes the number of charges present and δ describes the barrier effect. In addition, produced charges may be neutralised at a rate $\gamma > 0$. The total process is then described by the differential equation

$$\dot{n}_q = P_0(1 - \delta \cdot n_q) - \gamma \cdot n_q \tag{5.6}$$

where the values for P_0, δ, and γ depend on the process and the (local) material properties. The deduced time dependence of the number of charges present during and after laser illumination respectively then becomes

$$n_q(t) = \begin{cases} n_{\mathrm{eq}} \cdot [1 - \exp(\gamma_{\mathrm{on}} t)] \\ n_0 \cdot \exp(-\gamma_{\mathrm{off}} t) \end{cases} \tag{5.7}$$

where the inverse settling times are $\gamma_{\mathrm{on}} = \gamma + P_0\,\delta$ and $\gamma_{\mathrm{off}} = \gamma$; $n_{\mathrm{eq}} = P_0/\gamma_{\mathrm{on}}$ is the steady-state solution under illumination, and a constant, n_0, reflects the amount of charge present at the moment the laser is switched off. These two solutions represent the core for fitting the charging effect on the trap surface and later, in section 5.3.3, for the charging of the glass plate.

However, the time dependence of the ion-string position for electrode charging is not well fitted with equation (5.7) alone. This is attributed to the fact that there is a multitude of metastable states to which the electrons may be excited, given the likely inhomogeneous nature of the electrodes' surface. Each state may have its own excitation probability and decay constant, leading to an inhomogeneous broadening. This is taken into account by expressing the total number of charges as the result of two separate charging processes with independent production rates and relaxation constants. The individual constants do not have a direct physical meaning and may depend on the specific time span investigated. However, as an indication, the derived relaxation constants for the charge production (laser on) are $1/\gamma_{\mathrm{on},1} = 2\,\mathrm{s}$ and $1/\gamma_{\mathrm{on},2} = 16\,\mathrm{s}$ and for the decay (laser off) $1/\gamma_{\mathrm{off},1} = 5\,\mathrm{s}$ and $1/\gamma_{\mathrm{off},2} = 120\,\mathrm{s}$. The limitation to two production processes does not affect the following analysis of the quantum efficiencies, that are dependent on P_0: at the time the laser is switched on, t_{on}, no charges are present, $n_q(t_{\mathrm{on}}) = 0$. In other terms $\dot{n}_q(t_{\mathrm{on}}) = P_0$. It is therefore sufficient to measure the initial ion velocities that are proportional to the initial charge production rate (see equation 5.8).

As explained above, the axial dependence of the field resulting from the charging laser is mapped out by changing the position of laser illumination with respect to the ions' position, Δz. Figure 5.6 shows the initial velocities for different powers of laser illumination for $\lambda = 375\,\mathrm{nm}$. The behaviour for the other wavelengths measured is qualitatively similar and can even be observed for infrared light at 729 nm. The activation energy for this charging process is thus less than the photon energy of 1.7 eV for 729 nm light. The fitted curves correspond to the initial velocities expected from the axial component at the ions' position of an increasing dipole field as described by

$$\dot{z}_{\mathrm{ion}} = \dot{D}_{\mathrm{rel}} \cdot \frac{h_{\mathrm{trap}} \cdot \Delta z}{\left((\Delta z)^2 + h_{\mathrm{trap}}^2\right)^{5/2}}\,. \tag{5.8}$$

Here $\dot{D}_{rel}$ is the fit parameter for the net production rate of surface charges (hence dipoles):

$$\dot{D}_{rel} = \frac{3 q_{\mathrm{Ca}}}{4\pi\epsilon_0 m_{\mathrm{Ca}} \omega^2} \cdot \dot{n}_q q_e r_{\mathrm{dip}} \tag{5.9}$$

with q_{Ca} and m_{Ca} the charge and mass of a calcium ion, ω the axial trap frequency, q_e the electron charge and r_{dip} the distance between charge and image charge, which is twice the

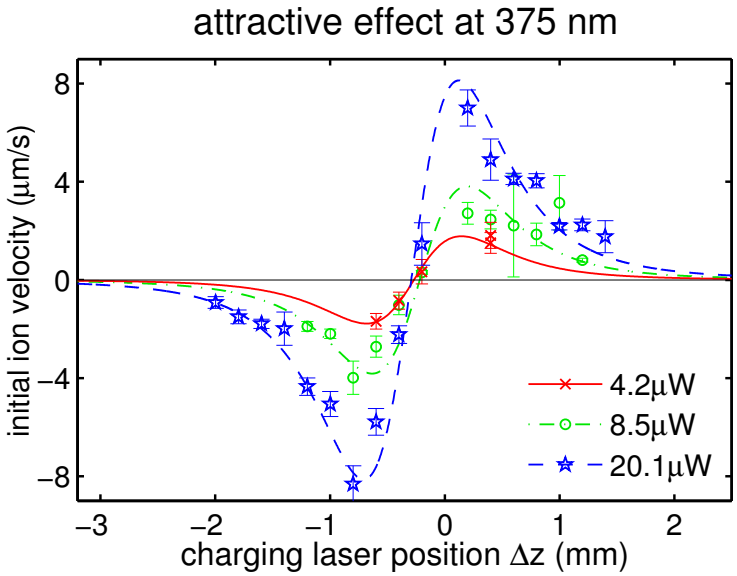

Figure 5.6: *Initial ion velocity as a function of laser beam position ($\lambda = 375\,\mathrm{nm}$) due to charging of the trap surface for different laser powers. For the other investigated charging laser wavelengths the results are similar and exclude any significant contributions from terms other than that of a dipole. The lines are fits according to equation 5.8.*

thickness of the insulating layer. The symbol h_{trap} denotes the height of the ions above the trap and Δz denotes the axial distance between ion and laser beam. The measured data excludes any significant contribution from monopole or quadrupole (and higher order) terms where the width of the curve would be bigger or smaller, respectively. Furthermore, it verifies that the production rate scales linearly with incident laser power.

As the thickness of the insulation patches, and hence the extension of the dipole r_{dip}, is unknown the quantum efficiency of the dipole production process, η_{dip}, can only be expressed in terms of this unknown value. For the wavelengths $\lambda = (375, 422, 729)\,\mathrm{nm}$ the resulting quantum efficiencies are $\eta_{\mathrm{dip}} = (14, 62, 0.2) \cdot 10^{-9}/(r_{\mathrm{dip}}/\mu\mathrm{m})$ respectively. The data does not provide sufficient information to propose a model that describes the wavelength dependence of the dipole-production rates, e.g. the significant reduction of the rate at 375 nm compared to that at 422 nm. Charging of the trap surface due to light at 397 nm could not be measured, because the stray light would render detection of the ions' fluorescence at the same wavelength impossible.

5.3.3 UV light-induced charging of an anti-reflective (AR) coated glass plate

The second effect that has been studied is charging on the surface of an anti-reflective coated glass plate. This plate is placed as close as $\sim 1.2\,\mathrm{mm}$ from the ions, parallel to the trap surface. The effect can be observed for the charging laser wavelengths shorter than 400 nm (375 and 397 nm). Figure 5.7 shows the ions' centre of mass position over

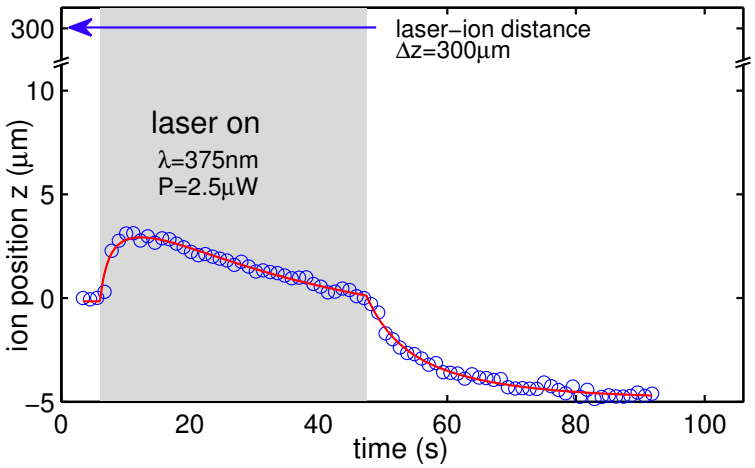

Figure 5.7: *Typical example of the axial positions of the ion string as the illuminating laser is switched on (grey-shaded area). The data was taken with* $2.5\,\mu$W *of* $\lambda = 375\,$nm *light, focussed on the trap at* $\Delta z = 300\,\mu$m *away from the ion on the axial electrode and the glass plate is* $h_{\mathrm{glass}} \sim 1.2\,$mm *away from the ions. In addition to the charging on the trap, the laser penetrating the glass plate leads to a positive charging of the glass. This causes the ion string to move away from the laser beam. After the laser is switched off, the ions relax slowly, indicating the relaxation of the charges at the trap, whereas the charge on the glass remains for days. The solid lines are the exponential fits to the data.*

time as the charging laser at 375 nm is switched on for 32 s shining through the glass plate and hitting the trap $\Delta z = 300\,\mu$m away from the ions. As the laser is switched on the ions first move towards the laser beam as they did for the experiment without the glass plate. This implies an attractive, negative charging. However, after a few seconds the attractive force is overcome by a repulsive one, causing the ions to turn around and move away from the charging laser beam. This movement saturates, dependent on the applied laser intensity, on a timescale of minutes. After the laser is switched off, the relaxation of the charging on the trap makes the ions move further away from the laser beam, whereas the displacement caused by the additional repulsive force subsequently remains unchanged for days. When the dielectric glass plate is brought close to the surface trap it might be expected that electrons are extracted from the trap electrodes by light or by the trap voltage and settle on the glass that would attract the ions and make them move towards the laser beam. While it cannot be excluded that this negative charging effect occurs to a small degree, the only detectable effect is a net positive charging at the position where the laser penetrates the glass. The induced repulsive effect on the ion string can be separated from the trap-surface effects because the trap-surface effects relax on a short time scale while the glass charging remains. This positive charging is attributed to the ejection of electrons from the anti-reflective coating of the substrate. Since these holes are produced in a dielectric surrounding, no electrons can be reabsorbed and therefore the charge creation is irreversible.

In figure 5.7 the ions' movement is fitted with a model which sums both the attractive

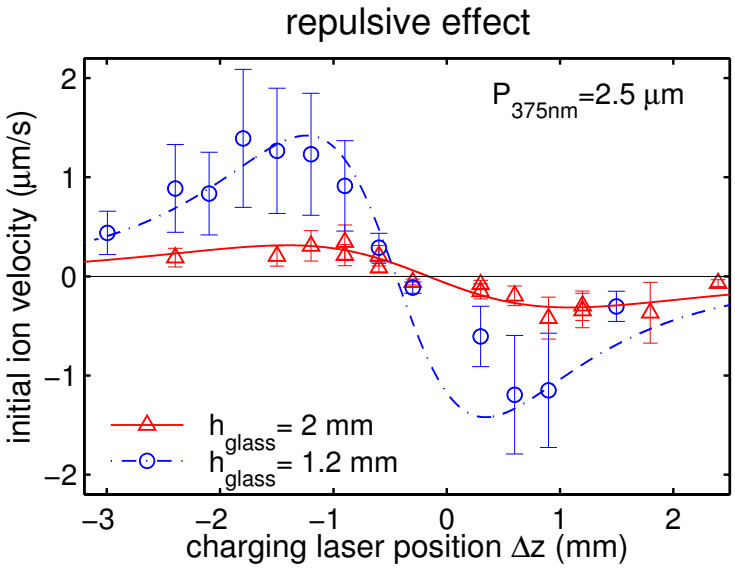

Figure 5.8: *The initial ion velocity as a function of beam position ($\lambda = 375\,\mathrm{nm}$) due to charging of the glass surface for different ion-glass distances h_{glass}. The effect due to the charging of the ion trap surface is subtracted from the data. This leaves the effect of glass-plate charging shown. The lines are fits according to equation 5.10. The error bars are the one sigma confidence intervals extracted from the theoretical calculations of the time dependence of the ions' positions (as shown in figure 5.7).*

and repulsive effects (see equation 5.7) under the condition that the relaxation rate for the repulsive effect is $\gamma = 0$. The ion velocities induced by the glass charging are shown in figure 5.8 for two different ion-glass distances h_{glass} at a laser power of $\sim 2.5\,\mu\mathrm{W}$. The charging saturates on a timescale of $1/\gamma_{\mathrm{on}} = 38\,\mathrm{s}$. The fitted curves indicate the expected axial field for a point charge located at the glass surface nearest to the ion trap. The charging effect at the backside of the glass plate has been neglected as the thickness of the glass (5 mm) is large compared to the ion-glass distance. In addition to this monopole-like contribution

$$\dot{z}_{\mathrm{ion}} = \dot{Q}_{\mathrm{rel}} \cdot \frac{\Delta z}{\left(\Delta z^2 + h_{\mathrm{glass}}^2\right)^{3/2}} \tag{5.10}$$

the small shielding due to an image charge with opposite sign and appropriate distance (at $h_{\mathrm{glass}} + h_{\mathrm{trap}}$ below the trap surface) has been taken into account. No significant contribution to the field from dipoles on the glass surface is observed. In equation (5.10) h_{glass} is the ion-glass distance and n_q the number of positive charges created on the glass plate and $\dot{Q}_{\mathrm{rel}}$ is the relative charge production rate:

$$\dot{Q}_{\mathrm{rel}} = \frac{q_{\mathrm{Ca}}}{4\pi\epsilon_0 m_{\mathrm{Ca}}\omega^2} \cdot \dot{n}_q\, q_{\mathrm{e}}. \tag{5.11}$$

With the known trap frequency $\omega \sim 90\mathrm{kHz}$ the charge-production efficiency is calculated to be $\eta_{375} = 1.2 \cdot 10^{-10}$ electrons per photon at $\lambda = 375\,\mathrm{nm}$. For $\lambda = 422\,\mathrm{nm}$ and

$\lambda = 729\,\text{nm}$ no movement of the ion string, and therefore charging of the glass, could be detected at the given level of sensitivity.

Analysing the charging of the glass plate with 397 nm light

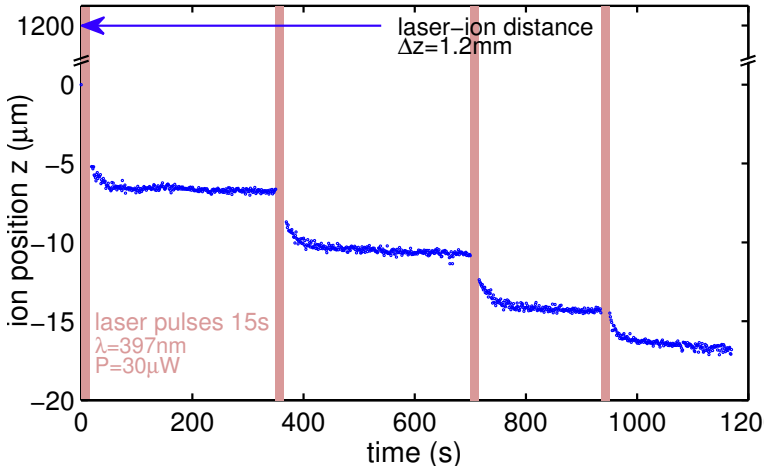

Figure 5.9: *Experiment carried out to measure the charging efficiency of* 397 nm *light. The charging laser at* 397 nm *is switched on for* 15 *s while the camera is off (red shaded areas). During the illumination the glass and the trap surface are charging up similar to the experiments with* 375 nm *light. After the charging laser is switched off, the camera can detect the ions position as the charges on the trap surface relax while the charging on the glass plate remains. That way, the charging rate of the glass plate due to laser light at 397 nm can be measured.*

The EM CCD camera is equipped with a narrow-band optical filter to filter out any light except the ions' fluorescence light at 397 nm. Thus the significant stray light at 375 nm, 422 nm and 729 nm does not interfere with measuring the ions' fluorescence at 397 nm. However, the ions cannot be imaged (using 397 nm light) at the same time as the trap is directly illuminated with 397 nm light. Nonetheless, the charging effects of the glass plate for 397 nm light can be measured in a pulsed way. While the camera is off, the charging laser is switched on for 15 seconds. During the laser illumination, the glass and the trap surface are being charged. After the charging laser is switched off, the ion string position can be measured (camera on) while the charges on the trap relax, whereas the charges on the glass remain unchanged. Thus, the difference in the ions' position before the charging light was switched on and after the relaxation of the charges on the trap is due to the charging of the glass plate. This procedure was repeated four times, to reveal the charge production rate on the glass surface (see figure 5.9). A comparison with the ion velocities with 375 nm light hitting the trap at the same spot reveals the quantum efficiency of $\eta_{397} = 0.4 \cdot 10^{-10}$ at $\lambda = 397\,\text{nm}$.

5.3.4 Estimation of the charge sensitivity

Using ions as electric-field probes, two different quantities are of direct interest: the electric field itself and the related force acting on the ion string. The two quantities are linked by the charge of the probe, hence the number of ions used for the measurement. In systems where the field under study is not, or not strongly, affected by the probe, a higher field sensitivity can be obtained by increasing the number of ions. The force on the ions however scales linearly with the number of ions, and so does the back action on the field source. If this back action must be kept small, a high force sensitivity is desirable, which can be achieved by reducing the number of ions.

With the imaging method described here an upper limit for the position uncertainty of a three-ion crystal is computed from the residuals to be $\delta z = 0.12\,\mu$m for a one second acquisition time. The uncertainty in position scales with the inverse square root of the averaging time and of the number of ions n_{ion}, i.e. with $1/\sqrt{\mathrm{Hz}}$ and with $1/\sqrt{n_{\mathrm{ion}}}$. The time and ion-number dependence can thus be joined with the uncertainty to yield a sensitivity of $0.12\,\mu\mathrm{m} \cdot \sqrt{3/n_{\mathrm{ion}}\mathrm{Hz}} = 0.21\,\mu\mathrm{m}/\sqrt{n_{\mathrm{ion}}\mathrm{Hz}}$. Given the trap frequency of 90 kHz, this corresponds to an electric field sensitivity of $30\,\mathrm{mV}/(\mathrm{m} \cdot \sqrt{n_{\mathrm{ion}}\mathrm{Hz}})$, and a force sensitivity of $4.5\,\mathrm{zN} \cdot \sqrt{n_{\mathrm{ion}}/\mathrm{Hz}}$. Where ($\mathrm{zN} = 10^{-21}\,\mathrm{N}$). With the laser displacement, Δz, at the most sensitive position (peaks of the curves in figure 5.8) and with a glass-ion distance of 1.2 mm, this is equivalent to detecting the presence of 40 elementary charges with three ions within one second. For similar charge sensitivities, near-field probes such as scanning atomic force microscopes are usually required [93]. However, using the ion trap as a measuring device has the advantage that the sensor leaves the surface completely unobstructed and does not interfere with the measured effect.

Provided the precision of the ion-position measurement is limited by the imaging technique (as it is in the experiments described above), rather than the ion's thermal spread, the measurement sensitivity scales with the inverse square of the trap frequency. Beyond this limit, it scales with the inverse of the trap frequency. It would thus be relatively simple to improve the sensitivity of the ion probe method by an order of magnitude by reducing the ions' motional frequency. The sensitivity could be further increased using homodyne detection (e.g. observing micromotion sidebands for transverse excursion) or using quantum detection schemes [94].

5.4 Summary and outlook for ions as field probes

This chapter showed two methods where trapped ions are used as field probes to detect electric potentials that are either needed for trap operation or are perturbing it.

In the first experiment, a one-dimensional method to measure the axial electric potential of an ion trap is shown. In the limit of strong radial confinement it can be assumed that the height of the ion string above the trap does not change significantly. By applying small changes to the voltages of one electrode or group of electrodes the behaviour of these features can be determined differentially. This allows the experimental study of different processes, e.g. shuttling of ions within segmented ion traps. Although simulations can

qualitatively model such a process, there are both technical and fundamental reasons why this may not be sufficient. A direct probing of the trap is thus needed to reveal stable operational parameters. This method might also be expanded to higher dimensions, if the radial confinement is weakened, so that the ions are arranged in a 2D ion crystal [95, 96] or even 3D [97] ion crystals. Extending equation 5.3 to the higher dimensions, it enables sampling of the potential $\psi(x, y, z)$ in all dimensions. For the measurement of three dimensions the addition of suitable optics is required, whereas a two-dimensional measurement is already possible with the setup described here (figure 5.10). Furthermore, this method may find applications in sensitive measurements of surface physics, where the change of the trapping potential due do changes in the surface are revealed.

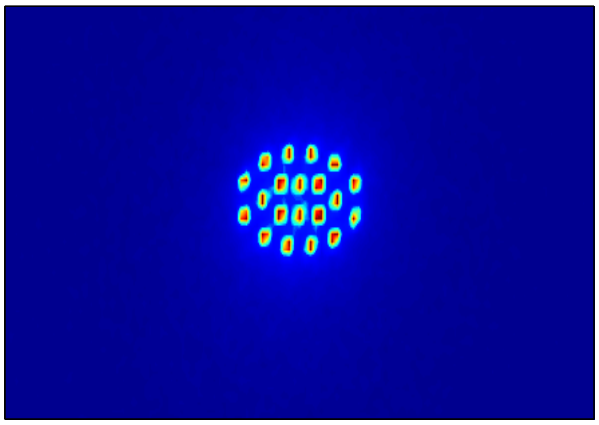

Figure 5.10: *A picture of a two-diemensional ion crystal with 20 ions trapped in Bastille. By extending the interpolation algorithm of section 5.2 one could obtain the two-dimensional trap potential of this configuration.*

The second experimental method uses trapped ions to reveal two distinct mechanisms for charging dielectrics. First, laser light impinging on the copper trap electrodes caused the accumulation of negative charges on the electrode surface, presumed to be located on insulating patches. Second, laser light incident on an optically-coated glass surface was observed to locally create positive charges. The obtained results are listed below.

Wavelength λ	375 nm	397 nm	422 nm	729 nm
Trap surface: $\eta_{\mathrm{dip}}(10^{-9}/(r_{\mathrm{dip}}/\mu\mathrm{m}))$	14	-	62	0.2
AR coated glass: $\eta(10^{-10})$	1.2	0.4	-	-

The low activation energy for the first process of less than 1.7 eV suggests the direct light-induced occupation of these patches (the work function of copper is ~ 4.5 eV [98]). Within the resolution of the measurement, no spatial variation was observed in the patch distribution. With a tightly focused laser beam it may be possible to directly resolve single patches of sizes on the order of a micrometre. Finally, this method provides a general tool to study local charging of any surface that can be brought close to an ion trap. This method has been successfully used in various groups to characterise the susceptibility of newly built ion traps to charging effects [99, 100].

Chapter 6

Quantum information transport using trapped-ion antennae

Transport of quantum information is one key feature to render quantum computers truly scalable [7]. This can be achieved either by transporting a particle that carries the information (e.g. an atom or a photon [18, 78]) or by transferring the quantum state from one part to another one within a coupled system. This chapter describes the experiments carried out to show the possibility of transferring quantum information from one ion trapping site to another one [83]. First a short description of the experimental characterisation of the sandwiched two-layer trap Micreon, described in chapter 4.3, is given. This includes the measurement of heating rates within the trap, cooling schemes and also the generation of an entangled pair of ions using a Mølmer - Sørensen interaction [49, 50]. The following sections describe the experimental coupling of ions via their Coulomb-interaction the coherent energy exchange between the two trapping sites and finally the amplification of the coupling strength with additional ions. The main results reported in these two sections have been published in [83].

6.1 The Micreon trap setup and its characteristics

In this section the experiments to characterise the new setup with the Micreon trap are discussed. The first part introduces a cooling method that, by using dark resonances, improved the cooling so that temperatures below the Doppler limit were reached. An important characteristic of an ion trap is its heating rate. The heating rates of the Micreon trap were measured for different settings of the electronics. The obtained results are presented and discussed in the second part of this section.

6.1.1 Fast cooling below the Doppler limit using dark resonances

In section 3.1.3 the Doppler limit is given for a two-level atom that is cooled under the weak binding condition. The derivation of this limit only includes the cooling and heating processes due to the interaction with the monochromatic laser light. In reality, though,

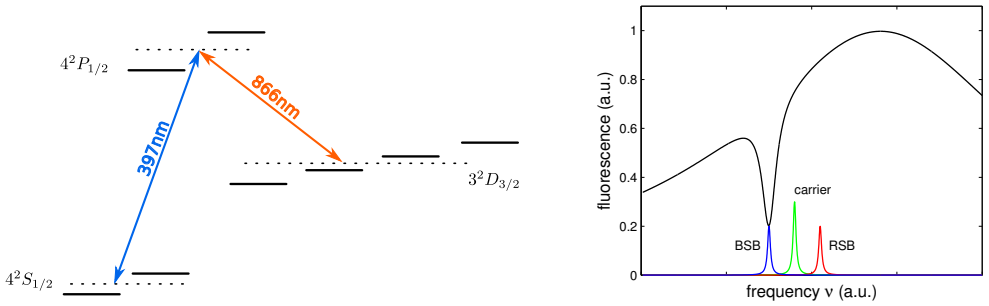

(a) **(b)**

Figure 6.1: *(a) The relevant energy levels for Doppler cooling. To define the quantisation axis a magnetic field is applied, which splits the degenerate Zeeman sublevels. The two lasers for cooling (including* 866 nm *repumping light) can fulfill the Raman condition for direct transfer between an* $|S_{1/2}\rangle$ *and* $|D_{3/2}\rangle$ *sublevel. (b) Model for an atom with one dark resonance, i.e. a three-level system, within the weak binding regime excited by a narrow-band laser. In the ion's rest-frame the red sideband transition of the laser shows up on the higher frequency side of the carrier (the energy of the annihilated motional quantum adds to the the light energy) and the blue sideband is on the lower frequency side. If the detuning of the laser is set such that the blue sideband (BSB) overlaps with the dark resonance, the induced heating process (see figure 3.3d) is suppressed. This can be used to improve the overall cooling rate and to reach a final temperature below the Doppler limit.*

there can also be heating effects due to other perturbations, such as the heating rate of the trap. Therefore, fast cooling techniques that also allow the ions to be cooled below the theoretical Doppler limit are advantageous to reach as low a motional state as possible, as fast as possible. One possibility to improve the Doppler cooling is to use the fact that $^{40}Ca^+$ is not a two-level system but has to be described (in this instance) as an eight-level system. Applying a magnetic field to define a quantisation axis lifts the degeneracy of the Zeeman sublevels. The relevant levels due to this Zeeman-splitting are shown in figure 6.1a.

The fluorescence of a $^{40}Ca^+$ ion at 397 nm under laser illumination (866 nm for repumping) in steady state depends on the occupation probability of the $|P_{1/2}\rangle$ state. For a fixed 397 nm frequency there are, due to the Zeeman sublevels, eight possible frequencies for the 866 nm light for which the Raman condition for a direct transfer between the $|S_{1/2}\rangle$ and the $|D_{3/2}\rangle$ state is fulfilled. The steady state in such a configuration is a dark state as it is a superposition of only the $|S_{1/2}\rangle$ and $|D_{3/2}\rangle$ states, without any contribution of the fluorescing $|P_{1/2}\rangle$ state. These so-called dark states show up as dips in the fluorescence spectrum of the ion (see figure 6.1b)[101]. The dark resonances depend on a variety of parameters: the magnetic field strength and direction and the laser lights' frequencies, intensities, polarisations and directions of propagation. A spectrum of these resonances with the current apparatus is shown in the top plot of figure 6.2. There the frequency of the laser at 397 nm is kept constant while the frequency of the 866 nm laser is scanned slowly across the resonance. A more detailed description on dark states and resonances can be found in [102]. As explained in section 3.1.3 the overall cooling rate and final tem-

perature is dependent on the rates of the cooling and heating processes. If the energy of a blue-sideband transition coincides with a dark resonance (figure 6.1b), one heating process is suppressed (see figure 3.3d). As a result a lower final temperature can be achieved[103].

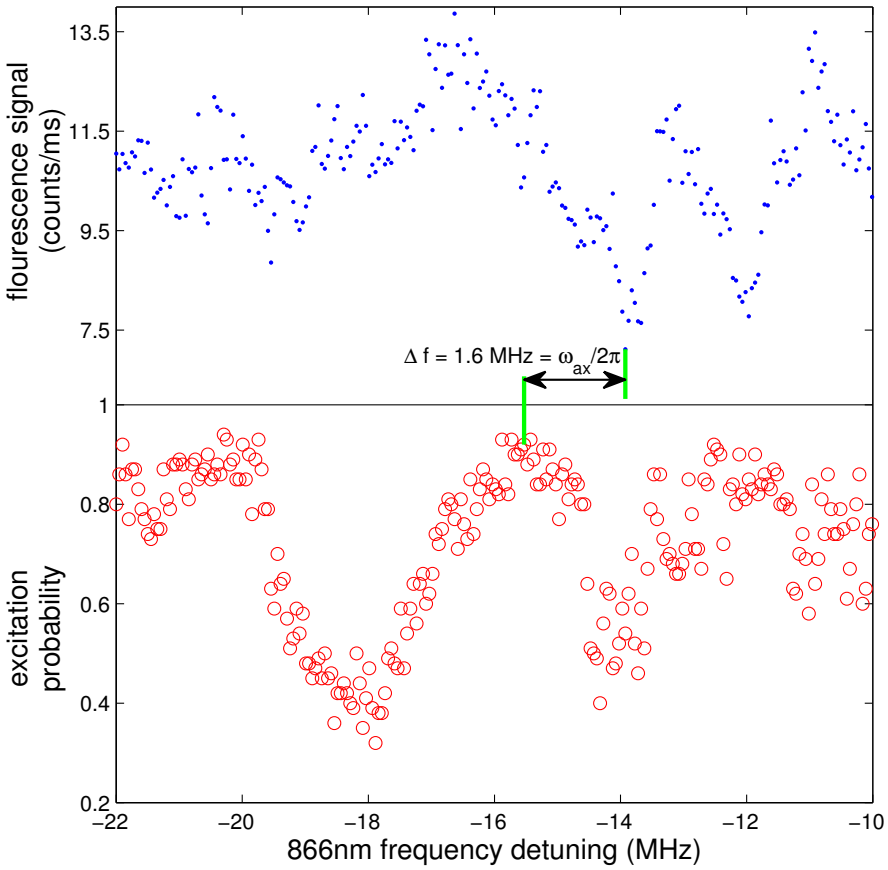

Figure 6.2: *a) A fluorescence signal of a single $^{40}Ca^{+}$ ion versus the detuning of the repumping laser frequency. The resonances showing a decreased signal are due to dark resonances. These can be used to improve Doppler cooling. b) The excitation probability after a $\frac{7\pi}{2}$ pulse as a measure of the contrast and thus the achieved cooling. A high excitation probability indicates a high Rabi oscillation contrast due to the improved cooling with the help of the dark resonances (indicated with a green line).*

As a measure for the final temperature, and therefore the efficacy of the cooling settings, the weak dependence of the Rabi-frequency on the motional state (see equation 3.5) can be used. The lower part of figure 6.2 shows the excitation probability after a $\frac{7\pi}{2}$-pulse and thus a direct measure of the cooling efficiency as the Rabi oscillation contrast increases with decreasing mean population $\bar{n}$ of the motional states. Figure 6.3 shows the full Rabi oscillations on the $S_{1/2} - D_{5/2}$ transition after Doppler cooling, after the improved Doppler cooling and after sideband cooling. The solid lines represent theoretical calculations of the

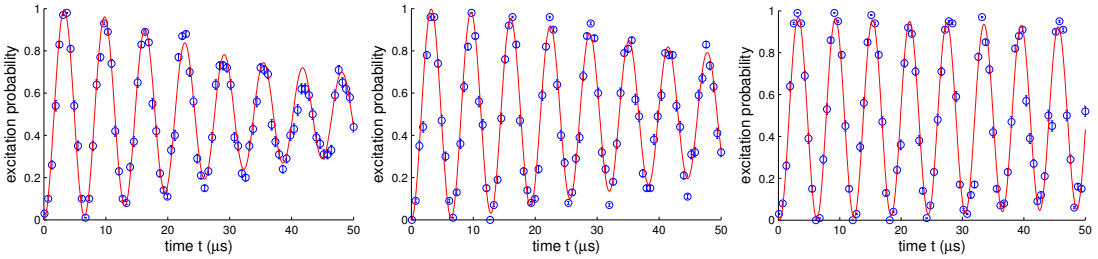

(a) (b) (c)

Figure 6.3: *Rabi oscillations after (a) standard Doppler cooling at* $\Gamma/2$ *detuning, (b) improved Doppler cooling at a dark resonance and (c) sideband cooling. The solid lines represent the calculated oscillations for a thermal state distribution of the axial motional-mode population with a frequency of* $\omega_{\text{axial}} = 2\pi \times 1.63\,\text{MHz}$ *and a Lamb-Dicke parameter* $\eta_{\text{eff}} = 0.086$*. The contributions of the radial spectator modes are neglected. The derived mean phonon numbers are (a)* $\bar{n} = 6.4(3)$*, (b)* $\bar{n} = 3.5(2)$ *and (c)* $\bar{n} = 1.7(2)$*. The standard Doppler-cooling limit for* $^{40}Ca^{+}$ *at this trap frequency is* $\bar{n}_{\text{dopp}} = \Gamma/2\omega = 6.13$*.*

oscillations following equation 3.5 assuming a thermal distribution of the axial motional state. The Rabi-frequency depends on the square of the Lamb-Dicke factor, η, which is smaller for the radial modes as their frequency is about 3 times higher. Further, it depends on the mean population of the motional modes, which, for the radial modes, is smaller than the one for the axial at the same thermal energy. The radial modes can thus be neglected and only the axial mode at a frequency of $\omega_{\text{axial}} = 2\pi \times 1.63\,\text{MHz}$ with an effective Lamb-Dicke parameter $\eta_{\text{eff}} = 0.086$ is taken into account. The measured mean motional phonon number of $\bar{n} = 6.4(3)$ for standard Doppler cooling (figure 6.3a) fits well with the expected Doppler cooling limit of $\bar{n}_{\text{dopp}} = 6.13$. The mean phonon number of $\bar{n} = 3.5(2)$ for the cooling at a dark resonance shows that temperatures below the Doppler limit are possible without the need for the slow sideband cooling. However, to reach even lower motional states, or even the motional ground state, it was necessary to use sideband-cooling techniques.

6.1.2 Heating-rates

The heating rate for the Micreon trap has been measured by comparing Rabi oscillations on the red and blue sidebands, following section 3.1.4 for different axial trapping frequencies. One example set of measurements is shown in figure 6.4, for a trapping frequency of $\omega_{\text{ax}} = 2\pi \times 1.84\,\text{MHz}$. The ion is initially cooled by the improved Doppler cooling, followed by sideband cooling. After four different waiting times, $\tau = 0,\ 1.5,\ 3$, and $4.5\,\text{ms}$, the Rabi oscillations are driven on the red and the blue sideband (figure 6.4, left side). The mean phonon numbers after each time between cooling and measurement are then calculated by equations 3.8 and 3.9, using a thermal state distribution. All oscillations have been measured with the same state initialisation and laser parameters. The effective Rabi oscillation frequency, Ω_{eff}, and a damping constant, that takes into account the loss of

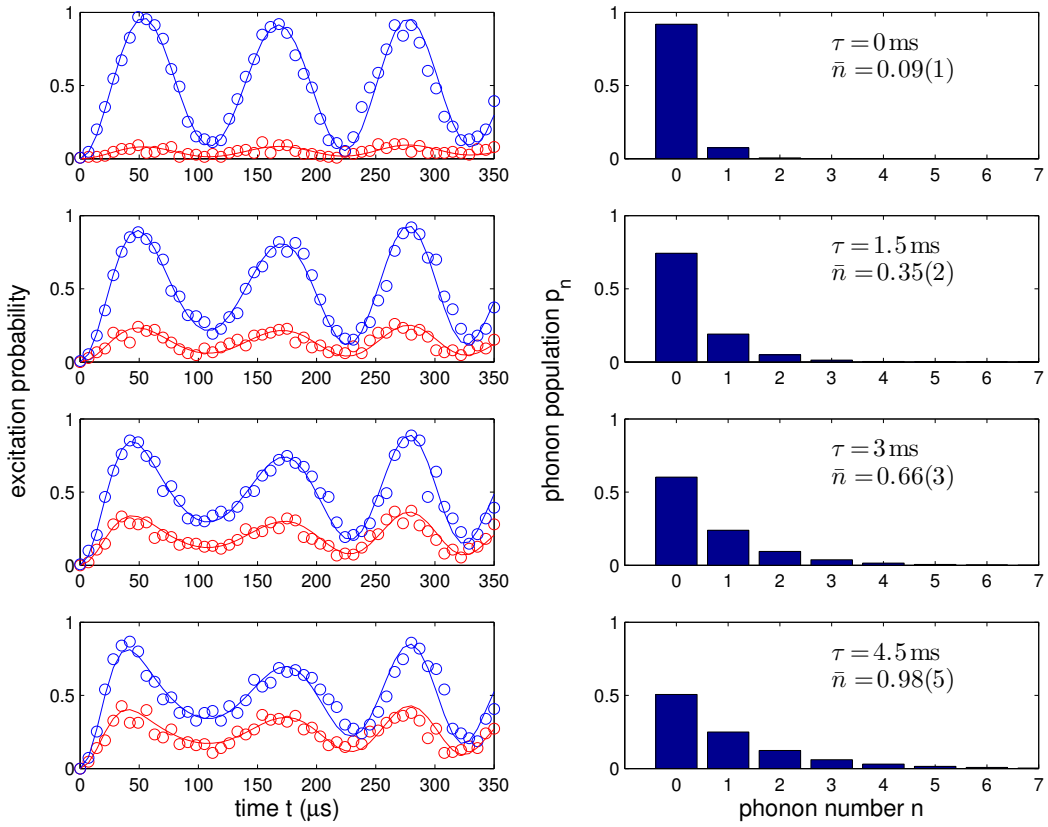

Figure 6.4: *(left) Red and blue Rabi oscillations to determine the mean phonon number for different waiting times, τ, after sideband cooling. The change of the mean phonon numbers underlying thermal distributions of the motional states (right) give a heating rate of* 0.19(1) *phonons per ms. The trap frequency is* $\omega_{\text{axial}} = 2\pi \times 1.84\,\text{MHz}$. *The measurements were performed for each waiting time, τ, with the same laser settings and these parameters were used simultaneously for all four calculations. The only free parameter is the mean phonon number*

contrast due to the radial spectator modes, are thus constant for all waiting times, τ. In this case, the heating of the radial modes has been neglected, as its effect on Ω_{eff} scales with η^2 and furthermore the heating of the radial modes is expected to be slower than the heating of the axial mode due to their higher frequencies. The final heating rate can then be determined, and in this case is $\dot{n} = 0.19(1)$ phonons per millisecond.

The heating rates have been measured for various axial trapping frequencies, ω_{ax}, ranging from $2\pi \times 0.8\,\text{kHz}$ to $2\pi \times 1.84\,\text{MHz}$, for three different configurations of the electrode voltage supply and low-pass filters. The results obtained are shown in figure 6.5. For the first heating rate measurements (red triangles) the trapping voltages were generated by lead batteries, referenced with a 10 V precision reference, and in-vacuum filters with cut-off frequency of 1 MHz (see section 4.3). The heating rates could be reduced by adding an additional 5.1 kΩ resistor to the low-pass filter outside of the vacuum feed throughs and thus reducing the cut-off frequency (blue squares figure 6.5). The larger resistor produces

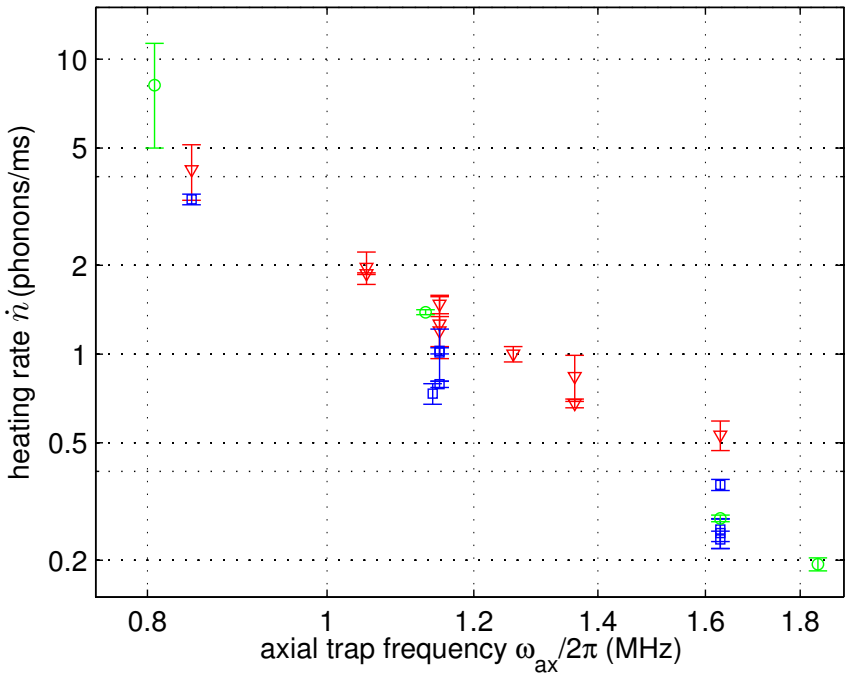

Figure 6.5: *The measured heating rates as a function of the axial trapping frequencies. The red triangles show the heating rates with the in-vacuum low-pass RC filter with* $R = 2.8\,\mathrm{k\Omega}$ *resistor and* $C = 55\,\mathrm{pF}$ *capacitor* ($f_{\mathrm{cut-off}} = 1\,\mathrm{MHz}$)*. By increasing the resistor to* $R = 7.9\,\mathrm{k\Omega}$ ($f_{\mathrm{cut-off}} = 370\,\mathrm{kHz}$) *the heating rates could be reduced (blue data points). The green circles indicate data taken with the improved filter board and with the commercially available ISEG high-voltage supply in place of the batteries. The higher heating rates for lower frequencies indicate a higher noise level of the ISEG supply in this range.*

more Johnson noise itself, but this effect is offset by the improved filtering. The net effect (above cut-off frequency) is to reduce the Johnson noise with the square root of the filter resistance.

$$I_{\text{Johnson noise}} = \sqrt{\frac{4k_BTR}{1+\omega^2(RC)^2}} \propto 1/\sqrt{R}. \tag{6.1}$$

By increasing the filter resistor from $2.8\,\Omega$ to $7.9\,\Omega$ one would expect a reduction of the heating rates with a factor of 1.7. For trap frequencies above 1 MHz the observed reduction in heating rates, and thus noise, is a factor of 1.6(8) assuming that $\dot{n} \propto 1/\omega_{\mathrm{ax}}^3$. Taking the lower frequencies into account leads to a different dependency on the trap frequency as these frequencies are close to or below the cut-off frequencies of the filter. Another reason for the higher heating rates at lower trap frequencies may be given by the unknown noise distribution of the voltage supplies that may have a higher noise at low frequencies. This assumption is supported by the data that shows an increase in heating rates at low frequencies above the technical noise dependency for the different voltage supplies. Furthermore, a further increase of the additional resistor (up to $53.8\,\mathrm{k\Omega}$) did not improve the heating rates, which also points to noise sources within the electronic system. The

third set (green circles) was carried out with the ISEG high-voltage supply ("ISEG box") in place of the batteries and with 370 kHz cut-off frequency of the in-vacuum filter. At high axial trapping frequencies ($\omega_{ax} > 1.2$ MHz) the performance of the ISEG box is similar to the batteries, but in the low frequency regime, e.g. $\omega_{ax} = 0.8$ MHz, the noise characteristics of the box induce even higher heating rates.

6.2 First segmented quantum information experiments in Innsbruck

Scalable quantum information processing was the ultimate goal of segmented trap experiments such as the Micreon trap. In the first part of this section the experiment to measure the coherence time of the $^{40}Ca^{+}$ qubit in the Micreon trap apparatus is presented. In the second part, an entangling Mølmer-Sørensen type gate is used to create a maximally entangled state with two ions.

6.2.1 Coherence time of a single qubit

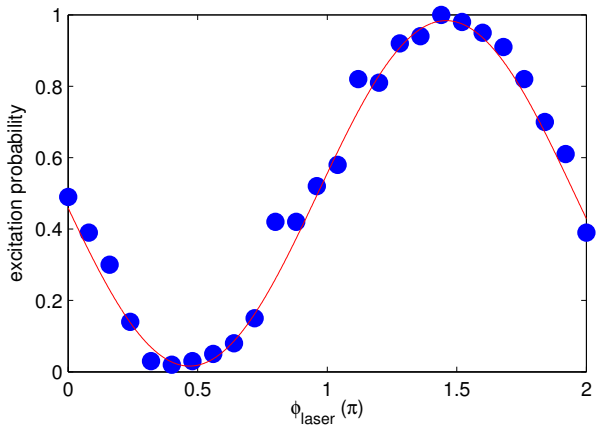

Figure 6.6: *Ramsey experiment with a waiting time of* 70 μs. *The excitation probability of the* $|D_{5/2}\rangle$*-state is shown for varied phase of the second laser pulse. The contrast is 96%.*

The coherence time of a qubit is defined by the time for which the phase and amplitudes of a prepared superposition state, e.g. a superposition of an $|S\rangle$ and $|D\rangle$ state, remains known. One fundamental limit of this time is the lifetime of the states, in which the qubit is stored. In the case of $^{40}Ca^{+}$ this is the lifetime of the metastable $|D_{5/2}\rangle$ state, which was measured to be 1.162 s [104]. However, there are technical sources of phase noise that cause a faster decay of the coherence. These sources include magnetic field fluctuations and fluctuations of the laser's amplitude, frequency and phase. Therefore the actual coherence time of the whole system is of interest.

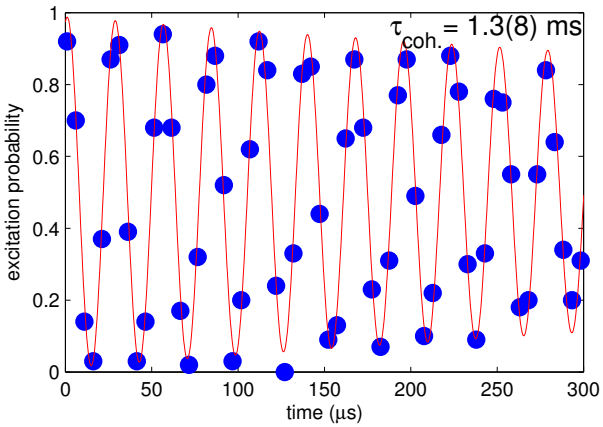

Figure 6.7: *Ramsey experiment with fixed phase and laser detuning of* $\Delta_{\text{laser}} = 35.9(1)\,\text{kHz}$. *An exponential fit gives an estimate of the coherence time of the single qubit,* $\tau_{\text{coh.}} = 1.3(8)\,\text{ms}$.

Ramsey experiments are a widely-used tool to determine the coherence time of a setup [86, 105]. In this method a superposition is created by a resonant $\pi/2$-pulse followed by a fixed waiting time, τ, during which the qubit evolves freely. A second resonant $\pi/2$-pulse will then map the phase, ϕ, of the qubit's superposition onto the populations of the $|S\rangle$ and $|D\rangle$ states. This phase consists of two contributions: the phase, $\delta\phi$, that the ion acquired during the waiting time, τ, and the phase of the second laser pulse with respect to the first laser pulse, ϕ_{laser}:

$$\phi = \delta\phi + \phi_{\text{laser}}. \tag{6.2}$$

Varying the relative phase of the second laser pulse leads to interferences in the excitation probability, shown in figure 6.6. The phase shift that the qubit acquired during the waiting time, is the result of the energy shift between the qubit and the reference, the laser light. Static phase shifts, induced for example by a detuning of the laser from the qubit resonance, where the detuning must be smaller than the Rabi frequency ($\Delta_{\text{laser}} \ll \Omega_{\text{Rabi}}$), lead to a shift of the interference fringes. Any random phase shifts, e.g. magnetic field noise or laser fluctuations, cause a loss of contrast of the interference.

There are different approaches to measure the coherence time with the Ramsey method. One accurate but slow solution is to measure the contrast of the Ramsey fringes after increasing waiting times. The loss of contrast over time thus gives the information of the decay of the coherence in the whole system. This decay is further dependent on the statistical characteristics of the noise and can lead to different timescales for each noise source [56].

Here, a slightly faster and simpler measurement of the coherence time is presented. It is performed by deliberately detuning the laser frequency and measuring the excitation probability after the second $\pi/2$ pulse with fixed phase for varying waiting times. The detuning of the laser frequency leads to an oscillation of the excitation probability at the frequency of the detuning of the laser (see figure 6.7). The obtained coherence time,

assuming for simplicity an exponential decay, is $\tau_{\text{coh.}} = 1.3(8)\,\text{ms}$. This is limited by the magnetic-field stability and laser linewidth. It may be improved by using fibre-noise cancellation [106] to reduce the frequency noise induced on the laser light by long fibre connections and enhancing magnetic shielding [46].

6.2.2 Two qubit entanglement with Mølmer-Sørensen gate

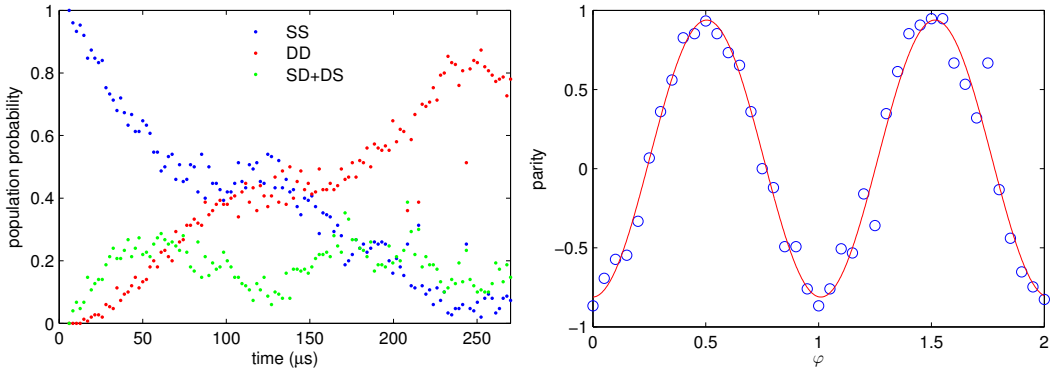

Figure 6.8: *Experimental results of an entangling Mølmer-Sørensen gate in a segmented ion trap. (a) The time evolution of the population probability of the two-qubit states* $|\text{SS}\rangle$ *(blue data points) and* $|\text{DD}\rangle$ *(red data points) and the sum of both states* $|\text{SD}\rangle$ *and* $|\text{DS}\rangle$ *(green data points). After the gate time* $t = 125\,\mu\text{s}$ *the unwanted populations in* $|\text{SD}\rangle$ *and* $|\text{DS}\rangle$ *interfere destructively and the two qubits are in the maximally entangled state* $|\text{SS}\rangle + |\text{DD}\rangle$*. (b) Parity oscillations of the two-qubit state after a* $\pi/2$ *pulse with varying phase.*

A basic requirement for a scalable quantum computer is to be able to create entangled qubit pairs, and further perform many-qubit gate operations. As a first step towards this goal, an entangling Mølmer-Sørensen gate has been performed in this new setup (see section 3.1.4). Two ions are confined at an axial trap frequency of $\omega_{\text{ax}} = 2\pi \times 1.63\,\text{MHz}$. Bichromatic beams were detuned by $\varepsilon = 8\,\text{kHz}$ from the motional red and blue sidebands of the $S_{1/2} - D_{5/2}$ transition. This leads to a gate-time of $125\,\mu\text{s}$ after which the maximally entangled state $|\text{SS}\rangle + |\text{DD}\rangle$ is prepared. The result of the time evolution of the qubit states is shown in figure 6.8a. As a test for the fidelity of the prepared $|\text{SS}\rangle + |\text{DD}\rangle$ state [36], parity oscillations were measured (see figure 6.8b). The obtained gate fidelity is 90(2)%. A higher fidelity could be achieved with some improvements on the setup, e.g. increasing the magnetic field stability by a μ-metal shielding box around the vacuum vessel similar to the one presented in the work of Tomas Monz [46]. Another limitation is the available light power of the 729 nm laser, as the gate time could be reduced further with higher Rabi oscillation frequencies, Ω [50].

6.3 Coulomb-coupling of ions in a double-well potential

The following section discusses the experiments that were performed in the new setup as a basic building block for a scalable ion trap quantum computation architecture [83]. The underlying idea is to directly transport quantum information within an ion trap from one trapping site to another without any particle transport. This direct coupling of two trapping sites is achieved by the dipole-dipole interaction due to the charged ions' motions in their respective trapping potentials, in analogy to two pendulums coupled with a massless spring. Here, the massless spring is represented by the dipole-dipole interaction. The first part of this section discusses the underlying physics of the coupled system. The second part presents the experimental realisation of coherent energy exchange between two adjacent trapping sites. The third part shows how additional ions were used to amplify the coupling strength as near-field antennae.

6.3.1 Dipole-dipole interaction of ions in adjacent traps

The dipole moment, $\vec{d}$, of an ion with charge, q, and mass, m, trapped in a harmonic trap with frequency, ω, is oriented along the trap axis, $\vec{z}$:

$$\vec{d} = q\Delta\vec{z}. \tag{6.3}$$

Δz is the vibrational amplitude of the ion's oscillation along the trap axis and, in the quantum mechanical limit, can be expressed with the creation and annihilation operators, $a^\dagger$ and a:

$$\Delta z = \sqrt{\frac{\hbar}{2m\omega}}\left(a + a^\dagger\right). \tag{6.4}$$

The dipole-dipole interaction strength of two such dipoles, $\vec{d}_1$ and $\vec{d}_2$, depends on their separation, $\vec{r}$, and orientation:

$$U_{dd} = \frac{1}{4\pi\varepsilon_0}\frac{\vec{d}_1\vec{d}_2 - 3(\vec{d}_1\cdot\hat{r})(\vec{d}_2\cdot\hat{r})}{r^3} \tag{6.5}$$

In the experiments of this section the dipole-dipole interaction of ions or ion strings held in two separate wells of a linear segmented ion trap is investigated. As the dipoles are oriented parallel to one another and along one axis the interaction strength with one ion in each well is:

$$\begin{aligned} U_{dd} &= -\frac{q_1 q_2}{2\pi\varepsilon_0}\frac{\Delta z_1 \Delta z_2}{r^3} \\ &= -\hbar\frac{\Omega_c}{2}\left(a_1 + a_1^\dagger\right)\left(a_2 + a_2^\dagger\right) \\ &\approx -\hbar\frac{\Omega_c}{2}\left(a_1 a_2^\dagger + a_1^\dagger a_2\right) \end{aligned} \tag{6.6}$$

with

$$\Omega_c = \frac{q_1 q_2}{2\pi\epsilon_0\sqrt{m_1 m_2\,\omega_1\omega_2}}\frac{1}{r^3} \tag{6.7}$$

where the subscripts 1 and 2 denote the well to which the parameter refers. In this approximation, the fast oscillating terms, $a_1 a_2$ and $a_1^\dagger a_2^\dagger$ have been omitted (rotating wave approximation). At resonance, i.e. $\omega_1 = \omega_2 = \omega_0$, the solution of the differential equations for the time-dependent creation operators in the Heisenberg picture are:

$$\begin{aligned} a_1^\dagger(t) &= e^{i\omega_0 t}\left(a_1^\dagger \cos\left(\frac{\Omega_c t}{2}\right) - i a_2^\dagger \sin\left(\frac{\Omega_c t}{2}\right)\right) \\ a_2^\dagger(t) &= e^{i\omega_0 t}\left(a_2^\dagger \cos\left(\frac{\Omega_c t}{2}\right) - i a_1^\dagger \sin\left(\frac{\Omega_c t}{2}\right)\right). \end{aligned} \tag{6.8}$$

After time $T_{\text{swap}} = \pi/\Omega_c$ the operators have changed roles ($a_1^\dagger$ became $a_2^\dagger$ and vice versa) with an additional phase factor such that the oscillators completely exchanged their motional states. Again, this can be seen as analogous to the behaviour of classical coupled pendulums at resonance. For each ion i the motional states, $|n_i\rangle$, their expectation values, $\langle n_i\rangle = \langle a_i^\dagger a_i\rangle$, and their mean phonon numbers, $\bar{n_i}$, oscillate back and forth between the two trapping sites at frequency $\Omega_c/2\pi$. More explicitly, under the dipole-dipole interaction at resonance, during the exchange of the motional energies between the two wells, entanglement is created between the initial motional state $|n_1, n_2\rangle$ and all other motional states $|n_1', n_2'\rangle$, that fulfill the requirement $n_1 + n_2 = n_1' + n_2'$. This entanglement is maximal after $t = T_{\text{swap}}/2$ and then coherently vanishes again into the unentangled, swapped state $|n_2, n_1\rangle$. The initial state $|0, 1\rangle$, for example, evolves into the entangled Bell state $(|0, 1\rangle + |1, 0\rangle)/\sqrt{2}$ at time $t = T_{\text{swap}}/2$. This motional entanglement can further be used, similar to the Cirac-Zoller type gate [47], to create maximally entangled internal states of the ions by mapping the motional state onto the electronic states. The speed of this gate using the coupled motion of the ions within the two wells depends directly on the coupling strength $\Omega_c \sim 1/r^3$ and hence on the separation r of the two trapping sites. This means small distances are favorable. This, however, requires small trap geometries, which would in return lead to higher heating rates. As an example, $^{40}Ca^+$ ions stored in two wells with resonant trapping frequency $\omega_0 = 1\,\text{MHz}$ separated by $100\,\mu\text{m}$ would experience a coupling strength of $\Omega_c = 2\pi \times 0.18\,\text{kHz}$. The creation of a maximally entangled motional state would then be achieved in $T_{\text{swap}}/2 = \pi/2\Omega_c = 1.4\,\text{ms}$, which would then be too long in comparison to either or both of the electronic coherence time or the underlying heating rate. One can use more ions in each well to increase the coupling strength, as described in the experiments at the end of this section.

6.3.2 Creation of a double-well potential in the Micreon trap

In the following experiments ions are stored in a double-well potential with a well separation of about $50\,\mu\text{m}$. Such a potential can be well described by a fourth-order polynomial, where for the symmetric case, i.e. at resonance, the first and third order contribution can be eliminated by a proper choice of origin.

$$E_{\text{pot}}(z) = q\left(\alpha_2 z^2 + \alpha_4 z^4\right) \tag{6.9}$$

In a linear trap a minimum of five electrode pairs is needed to create a double-well potential. Despite the $250\,\mu\text{m}$ wide electrodes of the Micreon trap, with a pitch of $280\,\mu\text{m}$,

and an ion-electrode distance of 258 μm, such a potential can be created. The voltages $U_1 = U_5 = 110.4\,\mathrm{V}$, $U_2 = U_4 = -16.8\,\mathrm{V}$ and $U_3 = 13.7\,\mathrm{V}$ are applied to the five electrode pairs to create a double-well potential with a separation of $r = 54\,\mu\mathrm{m}$ and trapping frequency of $\omega_0 = 537\,\mathrm{kHz}$. Figure 6.9 shows a schematic of the section of the trap used and a simulation of the potential created. Two electrode pairs were used during the experiments in addition to the minimum five pairs required for the quartic potential. One pair (on the extreme left of figure 6.9) was used to create an additional, nearly homogeneous electric field at the ions' positions. This adds a first order contribution to the axial potential, $\alpha_1 z$, and thereby shifts the individual trap frequencies of the two wells in opposite directions. By applying a voltage, U_{ax}, to this electrode pair, the two traps can be tuned into and out of resonance. The second additional electrode pair (on the extreme right of figure 6.9a) was held at a voltage of $U_{\mathrm{comp}} \approx -33\,\mathrm{V}$. This was necessary to compensate for the asymmetry in the trapping region geometry, namely the presence of the taper region.

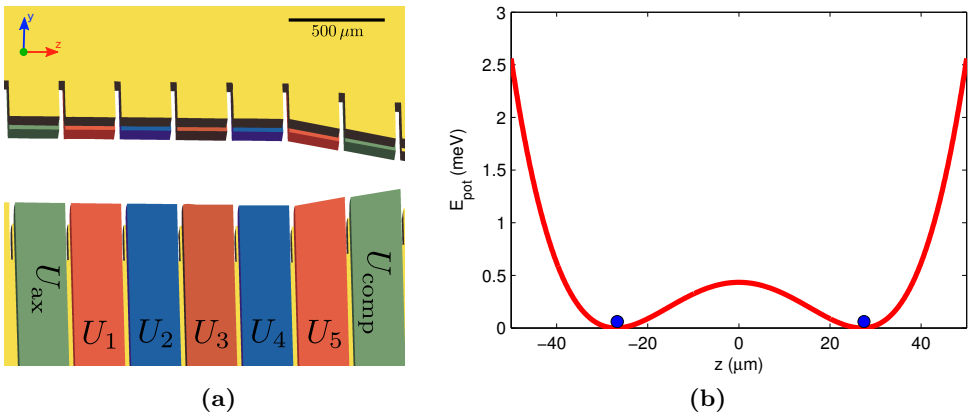

(a) **(b)**

Figure 6.9: *a) Schematic close-up of the zone of interest. The electrode pairs used to generate the double-well potential are colour-coded: red for positive voltages, blue for negative voltages and green for compensation voltages. b) The axial potential calculated with the parameters, r and ω_0, determined from the motional spectra in Fig. 6.12 is illustrated. The potential barrier between the two wells is* 4.3 meV.

6.3.3 Coherent energy exchange between two trapping sites

In order to demonstrate coherent energy exchange between the two traps, one ion was loaded into each well of the double well described in the previous section (6.3.2). By adjusting the control voltage U_{ax} the two traps were brought into resonance. During each experimental sequence the ions were first Doppler cooled for 2.5 ms with one laser beam, that was shaped elliptically to illuminate both trapping zones simultaneously. After Doppler cooling, sideband cooling was applied to both wells with two 729 nm laser beams focused individually on the two trapping sites. During the 4 ms cooling time the trapping sites were illuminated by the beams, alternating at the approximate rate of the coupling frequency between the two wells. This alternating sideband cooling creates an imbalance

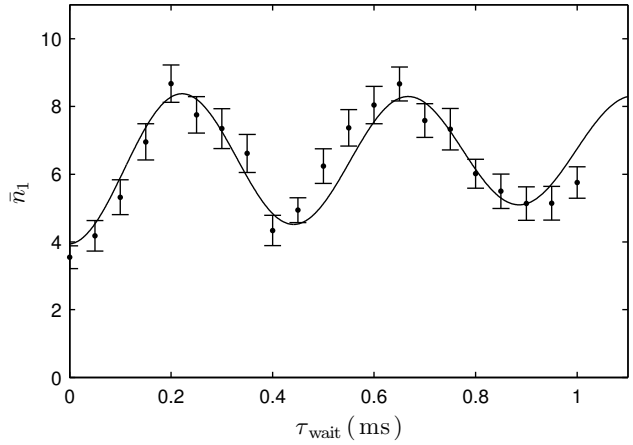

Figure 6.10: *The mean phonon number, $\bar{n}_1$, of the first well after the alternating sideband cooling and a waiting time τ_{wait}. The sideband cooling has been arranged to achieve an imbalance in the initial mean phonon numbers for the two wells, $\bar{n}_1 = 4(1)$ and $\bar{n}_2 = 9(1)$. The state exchange between the two coupled traps is revealed as an oscillation of the phonon numbers with a frequency of $\Omega_c = 2\pi \times 2.25(4)\,\mathrm{kHz}$ and an exchange time of $T_{\mathrm{swap}} = 220(10)\,\mu\mathrm{s}$. A damping constant $\tau_{\mathrm{damp}} = 3(2)\,\mathrm{ms}$ and a background heating of $\dot{\bar{n}} = 1.3(7)$ quanta per millisecond are inferred from the fit to the data. The error bars are determined by a Monte Carlo simulation and represent one standard deviation.*

in the phonon populations of the two traps as the motional states are exchanged between the two wells with the cooling following this exchange. As a result, the initial mean phonon number of the first ion is $\bar{n}_1 = 4(1)$, and for the second is $\bar{n}_2 = 9(1)$. After the cooling process the system evolves over a waiting time τ_{wait}. Then blue and red sideband flops are driven on the first ion for up to $60\,\mu\mathrm{s}$ and finally the state of this ion in the first trap well is detected. For the detection the same laser light is used as for Doppler cooling, but only the fluorescent light of the first ion is sent to the detector while the light from the other ion is blocked. The mean phonon number for the first well is then obtained in a similar manner to the heating rate measurement method in section 6.1.2. In this instance, however, thermal states are not used, but rather free population probabilities for every phonon state.

The resulting mean phonon numbers of the first ion as a function of the waiting time τ_{wait} is shown in figure 6.10. The solid lines represents a theoretical calculation of the evolution of the mean phonon number in one well on resonance:

$$\bar{n}_1(\tau_{\mathrm{wait}}) = \bar{n}_1(0) + \frac{1}{2}\Delta\bar{n}\left(1 - \cos\left(\pi\frac{\tau_{\mathrm{wait}}}{T_{\mathrm{swap}}}\right)\right)e^{-\frac{\tau_{\mathrm{wait}}}{\tau_{\mathrm{damp}}}} + \dot{\bar{n}}\tau_{\mathrm{wait}}. \tag{6.10}$$

$\Delta\bar{n}$ denotes the the difference between the initial mean phonon numbers of the two wells. Damping effects due to decoherence or any slow fluctuations of the experimental parameters, e.g. slight changes of the resonance condition due to voltages varying on the scale of millivolts, are taken into account with τ_{damp}. $\langle\dot{n}\rangle$ denotes the mean background heating rate for uncorrelated noise.

6.4 Ion-antennae to amplify the coupling strength

As presented in the previous section, it is possible to use the dipole-dipole interaction between two adjacent ion traps as a quantum-mechanical bus, to either transfer information from one site to the other, or to generate entanglement between the two sites. To do this the coupling strength would be ideally significantly larger than the underlying heating rate. This section describes how additional ions in each trapping well increase the coupling strength. In the first part, a different way to measure the coupling strength via spectroscopy is shown, followed by a description of the experiments where strings of up to three ions per trap are used to increase the coupling strength by a factor of up to seven.

6.4.1 Motional spectrum of coupled ions - avoided crossing

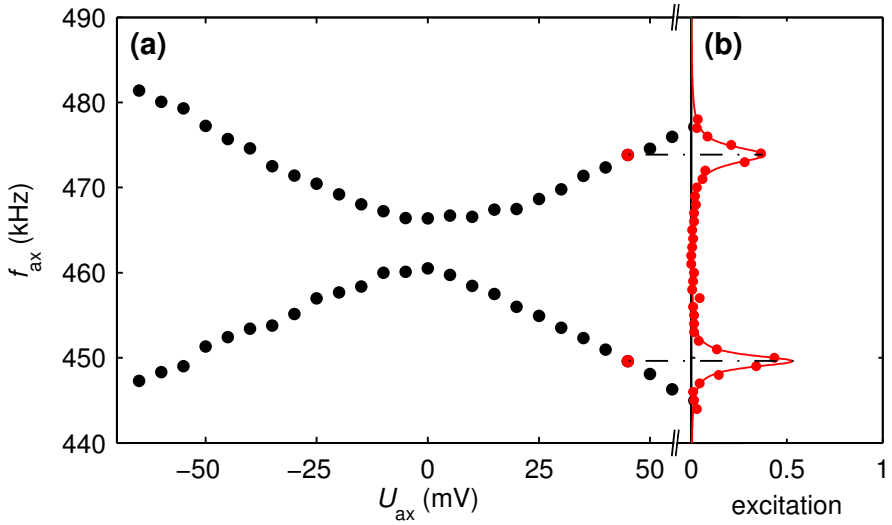

Figure 6.11: ***(a)*** *Oscillation frequencies of four trapped ions (two in each well) as a function of the axial control voltage U_{ax}, yielding a mode splitting of* 5.5(3) *kHz. The data points correspond to peaks in individual sideband spectra taken on the $S_{1/2}$-$D_{5/2}$ transition. The error bars are smaller than the dot size.* ***(b)*** *Example of an individual sideband spectrum. The resonant frequencies are marked with a dot-dashed line, and the corresponding data points in (a) are marked red.*

While it is possible to directly measure the coupling strength by observing the oscillation in phonon numbers as a function of time, there exists another, faster, method. To measure the coupling strength it is also possible to map out the ions' sideband excitation spectra on the $S_{1/2} - D_{5/2}$ transition as the trapping frequencies are scanned through the resonance condition. As explained in section 6.3.2, the applied control voltage U_{ax} at an outer electrode pair shifts the trap frequencies in opposite directions. Far below resonance ($\omega_1 \ll \omega_2$, $U_{ax} \sim -50\,\mathrm{mV}$) the wells do not interact, and the oscillations of the ions in each well are independent. Similarly, far above resonance ($\omega_1 \gg \omega_2$, $U_{ax} \sim +50\,\mathrm{mV}$) there is no interaction. However, near resonance the wells do couple and it is no longer possible

to describe the oscillations as independent motions in each well. Rather, the relevant eigenstates of the motion are "in phase" (COM-mode) and "out-of phase" (breathing mode). The frequencies of these new eigenstates, ω_{COM} and ω_{br}, are separated by the coupling strength Ω_c. The coupling of the two trap wells thus manifests as an avoided crossing, when tuning into and out of resonance. Figure 6.11 a shows an example of this avoided crossing for an experiment, where 2 ions are stored in each well. Each pair of (upper and lower) data points represents the resonance frequencies of the two trap wells for a given value of U_{ax}. These frequencies are determined with a sideband spectrum for both ion strings as shown in figure 6.11 b. The minimum distance of between the two frequencies is then the coupling strength at resonance. In this case $\Omega_c = 2\pi \times 5.5(3)\,\mathrm{kHz}$.

6.4.2 Experimental coupling strengths for up to three ions per trap

Equation 6.7 suggests, that the coupling strength scales linearly with N, the number of ions: $\Omega_c \sim q_1 q_2/\sqrt{m_1 m_2} \sim N$. However, this derivation of the coupling strength assumes a point charge in each trapping well. It neglects the fact that additional ions arrange as an extended string within the traps. The coupling strength dependency on the number of ions for a fixed axial potential can be calculated numerically. With the known potential $E_{\mathrm{pot}}(z)$ the total energy with N ions is

$$E^N_{\mathrm{tot}}(\vec{z}^N) = \sum_{i=1}^{N} E_{\mathrm{pot}}(z_i) + \sum_{i=1}^{N-1}\sum_{j=i+1}^{N} \frac{q^2}{4\pi\epsilon_0}\cdot\frac{1}{|z_i - z_j|} \tag{6.11}$$

$\vec{z}^N = (z_1, ..., z_N)$ denotes the position vector for all ions. The equilibrium positions $\vec{z}^N_0$ can be determined by minimising the total energy. The vibrational frequencies of all modes are then the eigenvalues of the Hessian matrix of $\frac{\partial^2}{\partial_i \partial_j} E^N_{\mathrm{tot}}$ at the equilibrium positions $\vec{z}^N_0$. The difference of the energies of the two center of mass modes in each trapping well, i.e. the two lowest eigenvalues, is then the coupling strength between the two traps.

Figure 6.12 displays avoided crossings of the motional spectra for six different configurations, where the number of ions was increased up to six ions (three per trap) while the created trapping potential remained unchanged. The curves represent the theoretical calculations of the spectra with three common parameters, α_1 α_2 and α_4, which determine the axial potential (see section 6.3.2) and the effect of the control voltage U_{ax}. This potential is the same as the one used in section 6.3.3 and the coupling strength of $\Omega_c = 2\pi \times 1.9(3)\,\mathrm{kHz}$ agrees within one standard deviation with the one measured with coherent energy exchange rate between the two wells. The data in Figure 6.12 (a) shows two measurements, where just one ion is stored in either the right or left trapping well. As there can be no coupling, the avoided crossing does not appear. The spectra in the second part of the figure are for configurations with one ion in each well, two ions in the left and one in the right, two ions in each and three ions in each well, as shown in the picture insets. The corresponding coupling strengths are then $\Omega_c(1+1) = 1.9(3)\,\mathrm{kHz}$, $\Omega_c(2+1) = 2.4(9)\,\mathrm{kHz}$, $\Omega_c(2+2) = 6.0(3)\,\mathrm{kHz}$, $\Omega_c(3+3) = 14(1)\,\mathrm{kHz}$. The seven-fold increase of the coupling is beyond the factor of three that is expected from a simple point-charge model and is due to the anharmonicity of the individual potential wells: as the

outer potential walls are steeper than the inner ones, the ion-strings' centers of mass get closer as more ions are added. At the same time, the average oscillation frequency is reduced. Both of these effects lead to an increase in the coupling strength (see equation 6.7). The extent of the ion strings provides a comparable increase as it is non-negligible with respect to the inter-well distance.

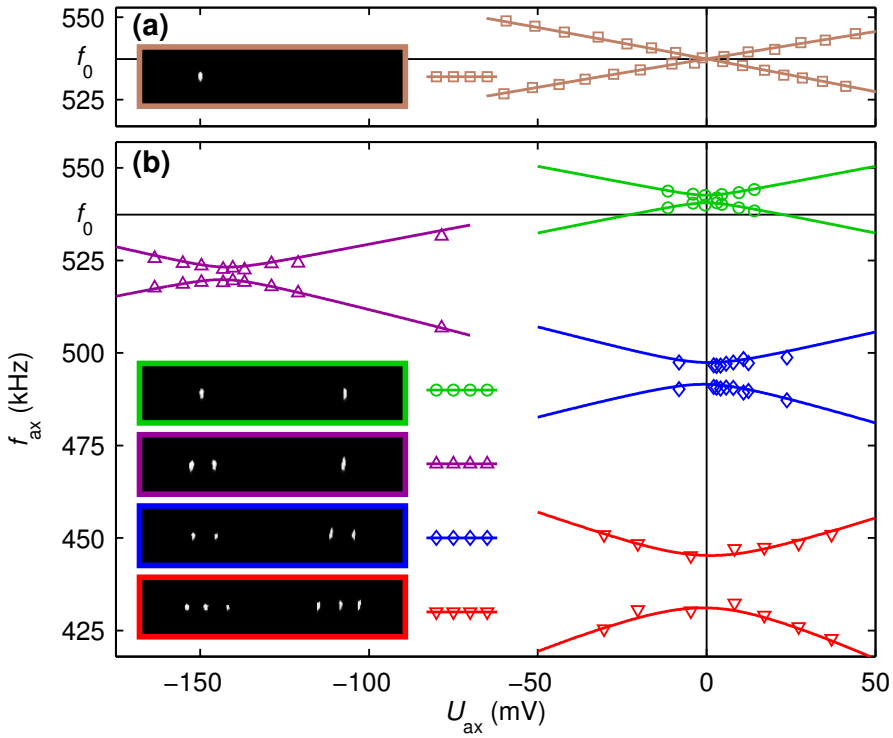

Figure 6.12: *Experimentally observed dipole-dipole coupling for various ion configurations in a double-well potential. The graphs display the oscillation frequencies of the two lowest vibrational modes as a function of control voltage U_{ax} and reveal the mode splitting at resonance; the horizontal line in each graph shows f_0. (a) Unmodified trap frequencies, as measured with a single ion in the left well (negative slope) or in the right well (positive slope). (b) Spectra with up to three ions in each well, as depicted in the insets (inset border colour matches data symbol and line colour). The lines represent predictions from numerical calculations and fit all data simultaneously. A small drift in the control voltage of* 7 mV *over one hour has been taken into account, aligning the spectra on top of one another. The mode splittings (in kHz) for the four different configurations are 1.9(3), 2.4(9), 6.0(3) and 14(1). The shift to lower voltages for three ions (2+1) is due to the asymmetry in their configuration. The vertical elongation of the ion pictures is due to aberrations, arising from an off-axis position of the ions relative to the imaging axis.*

6.5 Considerations for a Mølmer-Sørensen gate in a coupled double-well potential

The demonstrated coupling can be used in diverse schemes to create entanglement or to perform gate operations between coupled traps. Similar to the creation of Bell states, a Cirac-Zoller gate could be performed. However, this gate requires ground-state cooling. Another possibility is the thermally robust Mølmer-Sørensen gate [52], presented in section 3.1.4. For many ions (at least two) confined in a single linear trap, the additional motional modes are at least a factor of $\sqrt{3}$ higher than the frequency of the center of mass mode [35]. Therefore, the higher modes can be neglected, if the detuning $\varepsilon \sim 10\,\mathrm{kHz}$ of the bichromatic laser light is small compared to the mode splitting between the COM mode ($\omega_{\mathrm{COM}} \sim 1.6\,\mathrm{MHz}$) and the breathing mode ($\omega_{\mathrm{br}} \sim \sqrt{3}\omega_{\mathrm{COM}}$). The coupling strength, Ω_c, and thus the mode splitting between the COM and breathing mode for two adjacent ion traps, however, is significantly smaller (on the order of few kHz). As described

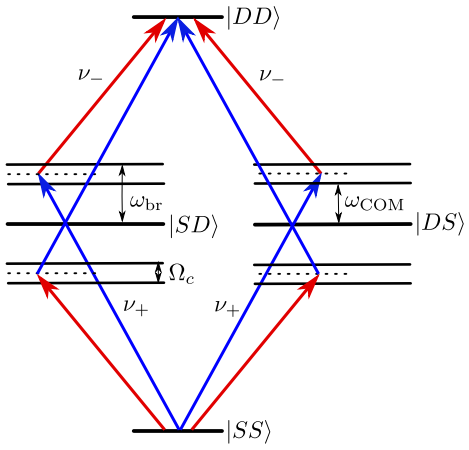

Figure 6.13: *Schematic of a Mølmer-Sørensen interaction with two ions in a coupled system of two adjacent traps. In this case both motional modes, the centre of mass mode, ω_{COM}, and the breathing mode, ω_{br}, have to be taken into account. A bichromatic light field detuned by $\varepsilon = \Omega_c/2$ can introduce an entangling gate between two ions in separate traps.*

in section 3.1.4 the detuned, bichromatic light field induces interference, that causes the unwanted populations in $|\mathrm{SD}\rangle$ and $|\mathrm{DS}\rangle$ to interfere destructively. A far detuning of the laser from the motional sidebands, i.e. $\varepsilon \gg \Omega_c$, creates such interference terms for both motional modes. However, as the Lamb-Dicke factors for these two modes have opposite signs (due to the direction of oscillation), the interference terms cancel and the gate does not work. One way to circumvent this, is to set the detuning of the laser light such that they are set in between the two modes as depicted in figure 6.13. The detuning ε is thus $\Omega_c/2$. The gate time for the MS gate directly depends on the detuning ε, and in this case again on the coupling strength Ω_c. Additional ions, as demonstrated in the previous

section, can be used as near-field antennae to increase the speed at which gates can be performed in these coupled systems.

6.6 Summary and outlook

This chapter presented an experimental characterisation of the Micreon apparatus. A fast cooling method was described that allows cooling below the Doppler limit using dark resonances. Furthermore, the heating rates of the trap are shown and were improved by appropriate choice of electronics.

The second part reports on the quantum information experiments in the apparatus. The electronic coherence time was measured to be 1.3(8) ms. The maximally entangled state $|\mathrm{SS}\rangle + |\mathrm{DD}\rangle$ has been generated using a Mølmer-Sørensen interaction with a fidelity of 90(2)%. Possible sources to improve the coherence of the system are laser-intensity stabilisation and magnetic-field shielding.

The third part of this chapter presented the experiments for a scalable architecture of a trapped-ion quantum computer using the dipole-dipole interaction. A coherent exchange of the motional state between two trapping wells was realised. The interaction strength was improved by a factor of about seven using three ions in each well, where they act as near-field antennae. This way of transporting quantum information within an ion trap can serve as a route to scale up ion-trap quantum computation. Bringing rows of traps pair-wise into resonance allows the creation of linear cluster states within two steps. A two-dimensional cluster state would only require two further steps by pair-wise coupling of columns.

Moreover, the dipole-dipole interaction is not limited to ions; the presented technique may be directly transferred to the coupling of trapped Rydberg atoms. Nor is the interaction limited to systems of equal mass, as demonstrated by the mode-splitting for the asymmetric configuration. Atomic and ionic systems may thus be combined. Neutral atoms have already been brought close to ions. When the ions' oscillation frequency is tuned into resonance with adjacent levels of a Rydberg atom, coupling between ions and Rydberg atoms may become achievable.

Chapter 7

Summary and outlook

Segmented ion traps are one possible route to render trapped-ion quantum information processing scalable. In this work, two experimental setups have been built incorporating two different traps: the surface trap "Bastille" and the sandwiched two-layer trap "Micreon".

With the surface trap, ions were used as probes for electric fields. These very sensitive probes allow direct measurement of effects which are difficult or impossible to observe by other means. The results allow experimental light to be shone on topics which were otherwise based on intuition.

In the first experiments (in section 5.2), the inter-ion distances within long chains of ions were used to calculate the axial trapping potential. This method was used to observe the potential changes during a shuttling routine, and to measure the axial effect of a single electrode upon the axial potential. The method can find applications for characterising and optimising ion trap geometries. Furthermore, this method could be extended to higher dimensions with the use of two- or three dimensional ion crystals [96, 97].

In the second experiments (section 5.3) a few ions were used to demonstrate light-induced charging effects on surfaces. It was demonstrated that the copper surface of the trap electrodes charges under illumination of laser light for various wavelengths ranging from 375 nm to 729 nm. Further, an anti-reflective coated glass plate could be charged with UV laser light (375 nm and 397 nm). By observing a string of three ions for one second the presence of as few as 40 elementary charges could be measured. Here, the ions can be used as tools for diagnostics of surfaces and trap structures. Moreover, the two methods could be combined. The field of a charging effect on a surface close to the ions could thus be spatially resolved.

While the experiments with the surface trap Bastille were of a more technical nature, those with the two-layer trap aimed to demonstrate future architectures of possibly scalable quantum computers. This goal was achieved by the successful demonstrations of the coupling of two quantum mechanical oscillators, here trapped ions. The coupling strength Ω_c between the two traps could be further increased by the use of additional ions. These act as near-field antennae and thus enhance the coupling.

This coupling can be used in diverse schemes to create entanglement or to perform

gate operations for quantum information processing. Creation of Bell states similar to the Cirac-Zoller gate would be possible, though this would require ground-state cooling of the ions. Another route to perform a thermally-robust quantum gate could be with a state-dependent pushing force induced by an appropriate laser. It should be noted that a fast variant of the thermally robust Mølmer-Sørensen gate may also be implemented in the system under consideration: if the required bichromatic laser beams are tuned to the centre of the mode splitting, a gate can be performed within $T_{\text{gate}} = 4\pi/\Omega_c$ (section 6.5).

The coupling scheme also has implications for possibly larger architectures for quantum computation. It is straightforward to imagine a linear array of ion traps, each holding a string of ions, able to interact axially. One could further imagine a two-dimensional array of traps in which parallel dipoles can also be coupled. This could then allow, for example, the production of large scale cluster states.

The experiments in this work introduced new methods for characterising and operating a future large-scale quantum computer. The first experiments (ions as field probes) allow a deeper understanding of practical considerations for scalable ion-traps. The second experiments (ions as near-field antennae) provide a foundation for quantum information transport within such an architecture.

Appendix A

Publications

- *Trapped-ion antennae for the transmission of quantum information*, M. Harlander, R. Lechner, M. Brownnutt, R. Blatt, W. Hänsel, Nature **471**, 200 (2011).
- *Trapped-ion probing of light-induced charging effects on dielectrics*, M. Harlander, M. Brownnutt, W. Hänsel, R. Blatt, New J. Phys. **12**, 093035 (2010).
- *Spatially-resolved potential measurement with ion crystals*, M. Brownnutt, M. Harlander, W. Hänsel, R. Blatt, arXiv:1105.0604v1 (2011).
- *14-qubit entanglement: creation and coherence*, T. Monz, P. Schindler, J. T. Barreiro, M. Chwalla, D. Nigg, W. A. Coish, M. Harlander, W. Hänsel, M. Hennrich, R. Blatt, Phys. Rev. Lett. **106**, 130506 (2011).
- *Deterministic reordering of 40Ca+ ions in a linear segmented Paul trap*, F. Splatt, M. Harlander, M. Brownnutt, F. Zhringer, R. Blatt, W. Hänsel, New J. Phys. **11**, 103008 (2009).

Bibliography

[1] H. Hertz, *Über die Grundgleichungen der Electrodynamik für bewegte Körper*, Ann. d. Phys. u. Chem. **40**, 27 (1890).

[2] P. Benioff, *Quantum mechanical models of turing machines that dissipate no energy*, Phys. Rev. Lett. **48**, 1581 (1982).

[3] R. Feynman, *Simulating physics with computers*, Int. J. Theoret. Phys. **21**, 467 (1982).

[4] QUIE^{2}T, *Strategic report on current status, visions and goals for research in Europe*, http://qurope.eu/content/Roadmap, 2010.

[5] A. Steane, *Quantum computing*, Reports on Progress in Physics **61**, 117 (1998).

[6] P. W. Shor, *Polynomial-time algorithms for prime factorization and discrete logarithms on a quantum computer*, SIAM J.SCI.STATIST.COMPUT. **26**, 1484 (1997).

[7] D. P. DiVincenzo, *The Physical Implementation of Quantum Computation*, Fortschr. Phys. **48**, 771 (2000).

[8] J. I. Cirac and P. Zoller, *A scalable quantum computer with ions in an array of microtraps*, Nature **404**, 579 (2000).

[9] W. Paul and H. Steinwedel, *Ein neues Massenspektrometer ohne Magnetfeld*, Zeitschrift Naturforschung Teil A **8**, 448 (1953).

[10] F. Major, V. Gheorghe, and G. Werth, *Charged Particle Traps*, Springer, 2004.

[11] R. F. Wuerker, H. Shelton, and R. V. Langmuir, *Electrodynamic Containment of Charged Particles*, Journal of Applied Physics **30**, 342 (1959).

[12] P. K. Gosh, *Ion traps*, Glarendon Press, 1995.

[13] J. P. Schiffer, *Phase transitions in anisotropically confined ionic crystals*, Phys. Rev. Lett. **70**, 818 (1993).

[14] C. Roos, *Controlling the quantum state of trapped ions*, PhD thesis, University of Innsbruck, Austria, (2000).

[15] S. Gulde, *Experimental realization of quantum gates and the Deutsch-Josza algorithm with trapped $^{40}Ca^{+}$-ions*, PhD thesis, University of Innsbruck, Austria, 2003.

[16] D. F. V. James and D. F. V. James, *Quantum dynamics of cold trapped ions with application to quantum computation*, Applied Physics B: Lasers and Optics **66**, 181 (1998).

[17] G.-D. Lin, S.-L. Zhu, R. Islam, K. Kim, M.-S. Chang, S. Korenblit, C. Monroe, and L.-M. Duan, *Large-scale quantum computation in an anharmonic linear ion trap*, Europhys. Lett. **86**, 60004 (2009).

[18] D. Kielpinski, C. Monroe, and D. J. Wineland, *Architecture for a large-scale ion-trap quantum computer.*, Nature **417**, 709 (2002).

[19] M. Kumph, M. Brownnutt, and R. Blatt, *Two-dimensional arrays of radio-frequency ion traps with addressable interactions*, New J. Phys. **13**, 073043 (2011).

[20] D. Stick, W. K. Hensinger, S. Olmschenk, M. J. Madsen, K. Schwab, and C. Monroe, *Ion trap in a semiconductor chip*, Nature Physics **2**, 36 (2006).

[21] M. Brownnutt, G. Wilpers, P. Gill, R. C. Thompson, and A. G. Sinclair, *Monolithic microfabricated ion trap chip design for scaleable quantum processors*, New J. Phys. **8**, 232 (2006).

[22] J. Britton, D. Leibfried, J. A. Beall, R. B. Blakestad, J. H. Wesenberg, and D. J. Wineland, *Scalable arrays of rf Paul traps in degenerate Si*, Applied Physics Letters **95**, 173102 (2009).

[23] S. A. Schulz, U. G. Poschinger, F. Ziesel, and F. Schmidt-Kaler, *Sideband cooling and coherent dynamics in a microchip multi-segmented ion trap*, New J. Phys. **10**, 045007 (2008).

[24] W. K. Hensinger, S. Olmschenk, D. Stick, D. Hucul, M. Yeo, M. Acton, L. Deslauriers, and C. Monroe, *T-junction ion trap array for two-dimensional ion shuttling storage, and manipulation*, Appl. Phys. Lett. **88**, 034101 (2006).

[25] R. B. Blakestad, C. Ospelkaus, A. P. VanDevender, J. M. Amini, J. Britton, D. Leibfried, and D. J. Wineland, *High fidelity transport of trapped-ion qubits through an x-junction trap array*, Phys. Rev. Lett. **102**, 153002 (2009).

[26] J. M. Amini, H. Uys, J. H. Wesenberg, S. Seidelin, J. Britton, J. J. Bollinger, D. Leibfried, C. Ospelkaus, A. P. VanDevender, and D. J. Wineland, *Toward scalable ion traps for quantum information processing*, New J. Phys. **12**, 033031 (2010).

[27] D. L. Moehring, C. Highstrete, D. Stick, K. M. Fortier, R. Haltli, C. Tigges, and M. G. Blain, *Design, fabrication and experimental demonstration of junction surface ion traps*, New J. Phys. **13**, 075018 (2011).

[28] M. Harlander, M. Brownnutt, W. Hänsel, and R. Blatt, *Trapped-ion probing of light-induced charging effects on dielectrics*, New J. Phys. **12**, 093035 (2010).

[29] Q. A. Turchette, Kielpinski, B. E. King, D. Leibfried, D. M. Meekhof, C. J. Myatt, M. A. Rowe, C. A. Sackett, C. S. Wood, W. M. Itano, C. Monroe, and D. J. Wineland, *Heating of trapped ions from the quantum ground state*, Phys. Rev. A **61**, 063418 (2000).

[30] L. Deslauriers, S. Olmschenk, D. Stick, W. K. Hensinger, J. Sterk, and C. Monroe, *Scaling and suppression of anomalous heating in ion traps.*, Phys. Rev. Lett. **97**, 103007 (2006).

[31] R. Reichle, D. Leibfried, R. B. Blakestad, J. B. J. D. Jost, E. Knill, C. Langer, R. Ozeri, S. Seidelin, and D. J. Wineland, *Transport dynamics of single ions in segmented microstructured paul trap arrays*, Progress of Physics **54**, 666 (2006).

[32] J. Jones, *Efficient Refocusing of One-Spin and Two-Spin Interactions for NMR Quantum Computation*, Journal of Magnetic Resonance **141**, 322 (1999).

[33] F. Shaikh, A. Ozakin, J. M. Amini, H. Hayden, C. S. Pai, C. Volin, D. R. Denison, D. Faircloth, A. W. Harter, and R. E. Slusher, *Monolithic Microfabricated Symmetric Ion Trap for Quantum Information Processing*, arXiv:1105.4909[quant-ph] (2011).

[34] R. J. Hendricks, D. M. Grant, P. F. Herskind, A. Dantan, and M. Drewsen, *An all-optical ion-loading technique for scalable microtrap architectures*, Appl. Phys. B **88**, 507 (2007).

[35] M. Riebe, *Preparation of entangled states and quantum teleportation with atomic qubits*, PhD thesis, University of Innsbruck, Austria, 2005.

[36] J. Benhelm, *Experimental quantum-information processing with $^{40}Ca^{+}$-ions*, PhD thesis, University of Innsbruck, Austria, 2008.

[37] S.-S. Liaw, *Ab initio calculation of the lifetimes of 4p and 3d levels of Ca^{+}*, Phys. Rev. A **51**, R1723 (1995).

[38] R. Loudon, *The quantum theory of light*, Oxford University Press, 1983.

[39] F. Schmidt-Kaler, H. Häffner, S. Gulde, M. Riebe, G. P. T. Lancaster, T. Deuschle, C. Becher, W. Hänsel, J. Eschner, C. F. Roos, and R. Blatt, *How to realize a universal quantum gate with trapped ions*, Appl. Phys. B **77**, 789 (2003).

[40] C. Monroe, D. M. Meekhof, B. E. King, S. R. Jefferts, W. M. Itano, D. J. Wineland, and P. Gould, *Resolved-sideband raman cooling of a bound atom to the 3d zero-point energy*, Phys. Rev. Lett. **75**, 4011 (1995).

[41] F. Schmidt-Kaler, C. Roos, H. C. Nägerl, H. Rohde, S. Gulde, A. Mundt, M. Lederbauer, G. Thalhammer, T. Zeiger, P. Barton, L. Hornekaer, G. Reymond, D. Leibfried, J. Eschner, and R. Blatt, *Ground state cooling, quantum state engineering and study of decoherence of ions in Paul traps*, Journal of Modern Optics , 2573 (2000).

[42] C. N. Cohen-Tannoudji, *Atomic motion in laser light*, In *fundamental systems in quantum optics*, Les Houches, Session LIII. Elsevier Science Publishers, (1990).

[43] S. Stenholm, *Semiclassical theory of laser cooling*, Rev. Mod. Phys. **58**, 699 (1986).

[44] D. J. Wineland and W. M. Itano, *Laser cooling of atoms*, Phys. Rev. A **21**, 1521 (1979).

[45] J. I. Cirac, R. Blatt, P. Zoller, and W. D. Phillips, *Laser cooling of trapped ions in a standing wave.*, Phys. Rev. A **46**, 2668 (1992).

[46] T. Monz, *Experimental*, PhD thesis, University of Innsbruck, Austria, 2011.

[47] J. I. Cirac and P. Zoller, *Quantum computations with cold trapped ions*, Phys. Rev. Lett. **74**, 4091 (1995).

[48] F. Schmidt-Kaler, H. Häffner, M. Riebe, S. Gulde, G. P. T. Lancaster, T. Deuschle, C. Becher, C. F. Roos, J. Eschner, and R. Blatt, *Realization of the Cirac-Zoller controlled-NOT quantum gate.*, Nature **422**, 408 (2003).

[49] A. Sørensen and K. Mølmer, *Quantum Computation with Ions in Thermal Motion*, Phys. Rev. Lett. **82**, 1971 (1999).

[50] J. Benhelm, G. Kirchmair, C. F. Roos, and R. Blatt, *Towards fault-tolerant quantum computing with trapped ions*, Nature Physics **4**, 463 (2008).

[51] D. Leibfried, B. DeMarco, V. Meyer, D. Lucas, M. Barrett, J. Britton, W. M. Itano, B. Jelenković, C. Langer, T. Rosenband, and D. J. Wineland, *Experimental demonstration of a robust, high-fidelity geometric two ion-qubit phase gate*, Nature **422**, 412 (2003).

[52] G. Kirchmair, J. Benhelm, F. Zähringer, R. Gerritsma, C. F. Roos, and R. Blatt, *Deterministic entanglement of ions in thermal states of motion*, New J. Phys. **11**, 023002 (2009).

[53] M. Riebe, H. Häffner, C. F. Roos, W. Hänsel, J. Benhelm, G. P. T. Lancaster, T. W. Körber, C. Becher, F. Schmidt-Kaler, D. F. V. James, and R. Blatt, *Deterministic quantum teleportation with atoms*, Nature **429**, 734 (2004).

[54] M. D. Barrett, J. Chiaverini, T. Schaetz, J. Britton, W. M. Itano, J. D. Jost, E. Knill, C. Langer, D. Leibfried, R. Ozeri, and D. J. Wineland, *Deterministic quantum teleportation of atomic qubits.*, Nature **429**, 737 (2004).

[55] M. Riebe, T. Monz, A. S. Villar, P. Schindler, M. Chwalla, M. Hennrich, and R. Blatt, *Deterministic entanglement swapping with an ion trap quantum computer*, Nat. Phys. **4**, 839 (2008).

[56] T. Monz, P. Schindler, J. T. Barreiro, M. Chwalla, D. Nigg, W. A. Coish, M. Harlander, W. Hänsel, M. Hennrich, and R. Blatt, *14-qubit entanglement: Creation and coherence*, Phys. Rev. Lett. **106**, 130506 (2011).

[57] P. Schindler, J. T. Barreiro, T. Monz, V. Nebendahl, D. Nigg, M. Chwalla, M. Hennrich, and R. Blatt, *Experimental Repetitive Quantum Error Correction*, Science **332**, 1059 (2011).

[58] R. Gerritsma, G. Kirchmair, F. Zähringer, E. Solano, R. Blatt, and C. F. Roos, *Quantum simulation of the Dirac equation*, Nature **463**, 68 (2010).

[59] F. Zähringer, G. Kirchmair, R. Gerritsma, E. Solano, R. Blatt, and C. F. Roos, *Realization of a quantum walk with one and two trapped ions*, Phys. Rev. Lett. **104**, 100503 (2010).

[60] J. T. Barreiro, M. Muller, P. Schindler, D. Nigg, T. Monz, M. Chwalla, M. Hennrich, C. F. Roos, P. Zoller, and R. Blatt, *An open-system quantum simulator with trapped ions*, Nature **470**, 486 (2011).

[61] D. Porras and J. I. Cirac, *Effective quantum spin systems with trapped ions*, Phys. Rev. Lett. **92**, 207901 (2004).

[62] M. Johanning, A. F. Varón, and C. Wunderlich, *Quantum simulations with cold trapped ions*, J. Phys. B **42**, 154009 (2009).

[63] D. Beckman, A. N. Chari, S. Devabhaktuni, and J. Preskill, *Efficient networks for quantum factoring*, Phys. Rev. A **54**, 1034 (1996).

[64] S. Lloyd, *Universal quantum simulators*, Science **273**, 1073 (1996).

[65] M. Richter, *How many qubits in a supercomputer*, Priv. comm.; The Cray XT5-HE (Jaguar) can store a 43-qubit quantum state., 2010.

[66] L.-M. Duan, *Scaling ion trap quantum computation through fast quantum gates*, Phys. Rev. Lett. **93**, 100502 (2004).

[67] K. Kim, M. S. Chang, S. Korenblit, R. Islam, E. E. Edwards, J. K. Freericks, G. D. Lin, L. M. Duan, and C. Monroe, *Quantum simulation of frustrated Ising spins with trapped ions*, Nature **465**, 590 (2010).

[68] M. Brownnutt, M. Harlander, W. Hänsel, and R. Blatt, *Spatially-resolved potential measurement with ion crystals*, arXiv:1105.0604[quant-ph] (2011).

[69] J. J. García-Ripoll, P. Zoller, and J. I. Cirac, *Speed optimized two-qubit gates with laser coherent control techniques for ion trap quantum computing*, Phys. Rev. Lett. **91**, 157901 (2003).

[70] S.-L. Zhu, C. Monroe, and L.-M. Duan, *Trapped ion quantum computation with transverse phonon modes*, Phys. Rev. Lett. **97**, 050505 (2006).

[71] F. Mintert and C. Wunderlich, *Ion-trap quantum logic using long-wavelength radiation*, Phys. Rev. Lett. **87**, 257904 (2001).

[72] M. Johanning, A. Braun, N. Timoney, V. Elman, W. Neuhauser, and C. Wunderlich, *Individual addressing of trapped ions and coupling of motional and spin states using rf radiation*, Phys. Rev. Lett. **102**, 073004 (2009).

[73] I. Cirac, P. Zoller, J. Kimble, and H. Mabuchi, *Quantum state transfer and entanglement distribution among distant nodes in a quantum network*, Phys. Rev. Lett. **78**, 3221 (1997).

[74] T. Wilk, S. C. Webster, A. Kuhn, and G. Rempe, *Single-Atom Single-Photon Quantum Interface*, Science **317**, 488 (2007).

[75] M. Keller, B. Lange, K. Hayasaka, W. Lange, and H. Walther, *Continuous generation of single photons with a controlled waveform in an ion-trap cavity system*, Nature **431**, 1075 (2004).

[76] H. G. Barros, A. Stute, T. E. Northup, C. Russo, P. O. Schmidt, and R. Blatt, *A deterministic single photon source from a trapped ion*, New J. Phys. **11**, 103004 (2009).

[77] L.-M. Duan, B. B. Blinov, D. L. Moehring, and C. Monroe, *Scalable trapped ion quantum computation with a probabilistic ion-photon mapping*, Quant. Inf. Comp. **4**, 165 (2004).

[78] D. L. Moehring, P. Maunz, S. Olmschenk, K. C. Younge, D. N. Matsukevich, L. M. Duan, and C. Monroe, *Entanglement of single-atom quantum bits at a distance*, Nature **449**, 68 (2007).

[79] B. H. J. Raussendorf R., *A one-way quantum computer*, Phys. Rev. Lett. **86**, 5188 (2001).

[80] A. Stute, *Rate of creating an entangled atom-photon pair with a cavity*, Priv. comm.; The rate at which the state of an ion can be entangled with an emitted photon is 40 Hz, 2012.

[81] M. A. Rowe, A. Ben-Kish, B. DeMarco, D. Leibfried, V. Meyer, J. Beall, J. Britton, J. Hughes, W. M. Itano, B. Jelenković, C. Langer, T. Rosenband, and D. J. Wineland, *Transport of quantum states and separation of ions in a dual RF ion trap*, Quant. Inf. Comp. **2**, 257 (2002).

[82] F. Splatt, M. Harlander, M. Brownnutt, F. Zähringer, R. Blatt, and W. Hänsel, *Deterministic reordering of $^{40}ca^{+}$ ions in a linear segmented paul trap*, New Journal of Physics **11**, 103008 (2009).

[83] M. Harlander, R. Lechner, M. Brownnutt, R. Blatt, and W. Hansel, *Trapped-ion antennae for the transmission of quantum information*, Nature **471**, 200 (2011).

[84] K. R. Brown, C. Ospelkaus, Y. Colombe, A. C. Wilson, D. Leibfried, and D. J. Wineland, *Coupled quantized mechanical oscillators*, Nature **471**, 196 (2011).

[85] R. W. P. Drever, J. L. Hall, F. V. Kowalski, J. Hough, G. M. Ford, A. J. Munley, and H. Ward, *Laser phase and frequency stabilization using an optical resonator*, Applied Physics B: Lasers and Optics **31**, 97 (1983).

[86] M. Chwalla, *Precision spectroscopy with $^{40}Ca^{+}$ ions in a Paul trap*, PhD thesis, University of Innsbruck, Austria, 2009.

[87] P. Schindler, *Frequency synthesis and pulse shaping for quantum information processing with trapped ions*, Diploma thesis, University of Innsbruck, Austria, (2008).

[88] F. Splatt, *Development and operation of miniaturised segmented ion traps for scalable quantum computation*, PhD thesis, University of Innsbruck, Austria, (2009).

[89] W. W. Macalpine and R. O. Schildknecht, *Coaxial resonators with helical inner conductor*, Proceedings of the IRE **49**, 2099 (1959).

[90] S. Schulz, *Scalable Microchip Ion Traps for Quantum Computation*, PhD thesis, University of Ulm, Germany, 2009.

[91] J. F. Eble, S. Ulm, P. Zahariev, F. Schmidt-Kaler, and K. Singer, *Feedback-optimized operations with linear ion crystals*, J. Opt. Soc. Am. B **27**, A99 (2010).

[92] W. J. Kim, A. O. Sushkov, D. A. R. Dalvit, and S. K. Lamoreaux, *Surface contact potential patches and casimir force measurements*, Phys. Rev. A **81**, 022505 (2010).

[93] G. Binnig, C. F. Quate, and C. Gerber, *Atomic force microscope*, Physical Review Letters **56**, 930 (1986).

[94] R. Maiwald, D. Leibfried, J. Britton, J. C. Bergquist, G. Leuchs, and D. J. Wineland, *Stylus ion trap for enhanced access and sensing*, Nature Physics **5**, 551 (2009).

[95] M. Block, A. Drakoudis, H. Leuthner, P. Seibert, G. Werth, M. Block, A. Drakoudis, H. Leuthner, and P. Seibert, *Crystalline ion structures in a Paul trap*, J. Phys. B: At. Mol. Opt. Phys. **33**, L375 (2000).

[96] I. M. Buluta and S. Hasegawa, *The structure of planar Coulomb crystals in RF traps*, J. Phys. B: At. Mol. Opt. Phys. **42**, 154004 (2009).

[97] L. Hornekær and M. Drewsen, *Formation process of large ion coulomb crystals in linear paul traps*, Phys. Rev. A **66**, 013412 (2002).

[98] P. A. Anderson, *The work function of copper*, Phys. Rev. **76**, 388 (1949).

[99] D. T. C. Allcock, T. P. Harty, H. A. Janacek, N. M. Linke, C. J. Ballance, A. M. Steane, D. M. Lucas, R. L. Jarecki, S. D. Habermehl, M. G. Blain, D. Stick, and D. L. Moehring, *Heating rate and electrode charging measurements in a scalable, microfabricated, surface-electrode ion trap*, Appl. Phys. B , 1 (2011).

[100] P. Herskind, *Integrated optics in ion-trap experiments*, Presentation at the institute of quantum optics and quantum technology (IQOQI), Innsbruck, 2011.

[101] M. O. Scully and M. S. Zubairy, *Quantum Optics*, Cambridge University Press, 1997.

[102] D. Rotter, *Quantum feedback and quantum correlation measurements with a single Barium ion*, PhD thesis, University of Innsbruck, Austria, 2008.

[103] S. Dirk Reiß, A. Lindner, and R. Blatt, *Cooling of trapped multilevel ions: A numerical analysis*, Physical Review A **54**, 5133 (1996).

[104] A. Kreuter, C. Becher, G. P. T. Lancaster, A. B. Mundt, C. Russo, H. Häffner, C. Roos, J. Eschner, F. Schmidt-Kaler, and R. Blatt, *Spontaneous emission lifetime of a single trapped Ca^+ ion in a high finesse cavity.*, Phys. Rev. Lett. **92**, 203002 (2004).

[105] N. F. Ramsey, *Molecular beams*, Clarendon Press, 1986.

[106] L.-S. Ma, P. Jungner, J. Ye, and J. L. Hall, *Delivering the same optical frequency at two places: accurate cancellation of phase noise introduced by an optical fiber or other time-varying path*, Opt. Lett. **19**, 1777 (1994).

Danksagung

Diese Arbeit wäre ohne die Unterstützung und Hilfe vieler Personen nicht möglich gewesen. Daher möchte ich mich an dieser Stelle bei ihnen herzlichst bedanken.

An erster Stelle gilt mein Dank Rainer Blatt. Er gab mir die Möglichkeit, diese Doktorarbeit in seiner Forschungsgruppe durchzuführen. Das angenehme Klima in seiner Gruppe und sein stetiger Einsatz für ein wissenschaftlich fruchtbares Umfeld bildeten ideale Arbeits- und Forschungsbedingungen.

Die zweite Person, der ich zu großem Dank verpflichtet bin, ist der Betreuer der Arbeit, Wolfgang Hänsel. Durch seinen unermüdlichen Einsatz konnten wir das Experiment vorantreiben und auch einzelne Rückschläge erfolgreich überwinden. Des Weiteren möchte ich mich auf diesem Wege bei Michael Brownnutt für das Korrekturlesen meiner Arbeit bedanken. Auch waren Michael, Wolfgang und Regina Lechner eine tatkräftige Unterstützung bei den Messungen, die häufiger bis spät in die Nacht andauerten.

Darüber hinaus möchte ich mich bei allen Mitgliedern der Arbeitsgruppe für die angenehme Atmosphäre und ihre bereitwillige Hilfestellung zu den verschiedensten Problemen bedanken. Namentlich möchte ich unter den vielen anderen Philipp Schindler als Berater in Elektronikfragen, Michael Chwalla, der Mann für *den* Laser, und Thomas Monz als Ansprechpartner zu Fragen in- und ausserhalb der Physik erwähnen. Auch den nichtwissenschaftlichen Mitarbeitern in den mechanischen und elektrischen Werkstätten und in den Sekretariaten gilt mein Dank, ohne deren eifrigen Einsatz diese Arbeit nicht möglich gewesen wäre.

Abschließend möchte ich meiner Familie herzlichst danken. Sie stand stets hinter mir und gab mir zu jeder Zeit ihre volle Unterstützung. Und ganz besonders möchte ich mich bei meiner Freundin Jasmin bedanken, für ihre Geduld, ihren Zuspruch und ihr Verständnis in den letzten Jahren.

Vielen, vielen Dank!